Annual Report 2006

Address:	Prof. Dr. Burkard Hillebrands Fachbereich Physik Technische Universität Kaiserslautern Erwin-Schrödinger-Straße 56 67663 Kaiserslautern, Germany Tel.: +49-(0)631-205-4228 Fax.:+49-(0)631-205-4095
Postal address:	Postfach 3049 67653 Kaiserslautern, Germany
Internet:	http://www.physik.uni-kl.de/hillebrands/
E-Mail:	hilleb@physik.uni-kl.de

Our Group

From left to right:

Prof. Dr. Burkard Hillebrands, Dr. Patrizio Candeloro,
Steven Crane(guest), Steffen Blomeier, Thomas Schneider,
Timo Neumann, Dr. Britta Leven, Bastian Leven, Dieter Weller,
Sibylle Müller, Bernd Pfaff, Sebastian Hermsdörfer, Sebastian Schäfer,
Björn Obry, Dr. Alexander Serga, Oksana Gaier, Christian Sandweg,
Dr. Jaroslav Hamrle, Andreas Beck

This report contains unpublished results and should
not be quoted without permission from the authors.

Contents

Chapter 1: Introduction

Dear Colleagues and Friends,

this year we celebrate our 10th anniversary of presenting an Annual Report, this time covering the period of November 2005 to October 2006. The last 10 years were filled with research and training on the dynamics of small magnetic structures, on linear and nonlinear spin wave properties, on ion irradiation induced modification and tailoring of magnetic materials as well as - in a separate enterprise - on functionalized surfaces, lately for biomedical applications. In total, in these 10 years 29 diploma students and 15 Ph.D. students completed their theses in our group, we have published 178 papers, we have given 379 presentations at conferences and workshops, and 29 guest scientists have visited our group, many of them several times.

Here we now report on our results obtained in the last 12 months. Highlights of this period are our new results on the Bose-Einstein condensation and related effects in magnon gases (a joint paper with Sergej O. Demokritov and coworkers in Münster, Genadij A. Melkov in Kiev and Andrei N. Slavin in Oakland University, Rochester, published in Nature), the spin quantization and coherency effects in small magnetic rings, the measurement of phase fronts of linear and nonlinear spin waves, microwave assisted magnetic switching, domain wall properties and coupling effects in embedded ferromagnetic elements, orthogonal exchange bias field directions in specific microstructures, and the magnetic properties of Heusler compounds. Concerning the latter we found a surprisingly large quadratic magneto-optic Kerr effect, the largest reported to our knowledge, which, also surprisingly, can be suppressed by low dose ion irradiation.

A highlight this year was the award of the doctor honoris causa to Albert Fert for his achievements in natural sciences, in particular for his discovery of the giant magnetoresistance effect. On the same day we have held our kick-off meeting of our new European Research Training Network "Spin Current Induced Ultrafast Switching (SPINSWITCH)" for which I serve as the coordinator. Partners, among them two industrial partners, are from Erlangen and Konstanz (Germany), from Paris and Grenoble (France), from Glasgow and from London (Great Britain), Leuven (Belgium), Salamanca (Spain), Lisboa (Portugal), from Krakow and Posnan (Poland), and from Iasi (Romania), see http://www.spinswitch.de for details. Albert Fert is also a member of this network.

I accepted the position of the Vice President for Research and Technology of my University starting in September. I accepted on the condition that I can continue research and can maintain the group on the same scientific level as before. As an outcome of the negotiations Alexander Serga received tenure, and he is now responsible for the research program on nonlinear spin wave properties.

A significant part of our work is embedded in the German priority program ("Schwerpunktprogramm") entitled "Ultrafast magnetization processes", and in the Research Unit ("Forschergruppe") entitled "New materials with high spin polarization", both funded by the Deutsche Forschungsgemeinschaft.

Locally we acknowledge support by the state funded priority center "Materials for Micro and Nanosystems" and by the "Center for Nanostructure Technology and Molecular Biological Technology", which is operated by our university providing the technology for patterning down to the deep submicron scale.

Our work would not have been possible without valuable collaborations with people all over the world. They are too many to list them here all. In particular we would like to thank, in alpha-

betical order, Yasuo Ando, Christian Back, Harry Bernas, John Chapman, Claude Chappert, Darrell Comins, Russell Cowburn, Vladislav Demidov, Sergej Demokritov, Bernard Dieny, Günter Dumpich, Hajo Elmers, Jürgen Fassbender, Gerhard Fecher, Claudia Felser, Claude Fermon, Jacques Ferré, Albert Fert, Paulo Freitas, Hubert Grimm, Andreas Hütten, Kouichiro Inomata, Gerhard Jakob, Martin Jourdan, Boris Kalinikos, Matthias Kläui, Mikhail Kostylev, Natalia Kreines, Liesbet Lagae, Jürgen Langer, Norbert Laube, Wolfram Maaß, Jan Marien, Roland Mattheis, Andrezj Maziewski, Jacques Miltat, Alexandra Mougin, Fabrizio Nizzoli, Carl Patton, Dorothée Petit, Kamel Postava, Günter Reiss, Karsten Rott, Ulrich Rüdiger, John R. Sandercock, Rudi Schäfer, Gerd Schönhense, Andrei Slavin, Bob Stamps, André Thiaville and Stefan Visnovsky for their interactions with us and their strong input to our work.

Collaborations within the Fachbereich Physik at the University of Kaiserslautern (in particular Martin Aeschlimann, James Anglin, Sebastian Eggert, Michael Fleischhauer, Volker Schünemann, Herbert Urbassek, Christiane Ziegler and their groups), the Institut für Oberflächen- und Schichtanalytik, as well as the Nano+Bio Center have been very stimulating. I am especially grateful to Heinz Busch and Udo Grabowy and their start up company NTTF GmbH for the close contact. I am much obliged to Peter Pesch and his team from the TZO GmbH for providing convenient general conditions for our work in Rheinbreitbach.

I would also like to thank all our sponsors, which are the Deutsche Forschungsgemeinschaft, the Bundesministerium für Bildung und Forschung, the Humboldt Foundation, the Deutscher Akademischer Austauschdienst, the European Community, INTAS, NEDO, the State of Rheinland-Pfalz and the University of Kaiserslautern. My special thanks go to Andreas Beck and Sibylle Müller for their help in preparing this report and to Hubert Gerber from Photo-Repro-Druck, TU Kaiserslautern.

It is my special pleasure to greet all former group members. May this report help to stay in touch with each other.

If you are interested in our work I would be happy to hear from you. If you have any questions, comments, suggestions, or any kind of criticism, please contact us.

With all my best wishes for Christmas, and a Happy New Year,

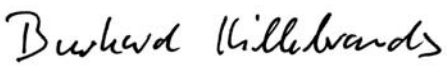

Kaiserslautern, November 2006

Chapter 2: Personnel

2.1 Members of the group

Group leader:

Prof. Dr. Burkard Hillebrands

Senior scientists:

Dr. Britta Leven
Dr. Alexander Serga

Postdocs and long-term guest scientists:

Prof. Dr. Yasuo Ando	until 12/05
Dr. Patrizio Candeloro	
Dr. Jaroslav Hamrle	
Dr. Seong-Gi Min	since 09/06
Dr. Hans Nembach	03/06 - 05/06
Dr. Natalia Sergeeva	since 10/06

PhD students:

Dipl.-Phys. Christian Bayer	until 12/05
Dipl.-Phys. Andreas Beck	
Dipl.-Phys. Sebastian Becker	since 08/06
Dipl.-Phys. Steffen Blomeier	
Dipl.-Phys. Ulla Böde (Rheinbreitbach)	since 01/06
Dipl.-Phys. Oksana Gaier	since 05/06
Dipl.-Phys. Sebastian Hermsdörfer	since 04/06
Dipl.-Phys. Dirk Hoffmann	until 12/05
Dipl.-Phys. Lisa Kleinen (Rheinbreitbach)	
Dipl.-Phys. Patricia Martin Pimentel	
Dipl.-Phys. Hans Nembach	until 02/06
Dipl.-Math. Timo Neumann	since 06/06
Dipl.-Phys. Maciej Oskar Liedke	
Dipl.-Phys. Thomas Schneider	since 11/05
Dipl.-Phys. Helmut Schultheiß	since 02/06
Dipl.-Phys. Markus Weber	until 12/05

Diploma Students:

Sebastian Hermsdörfer	until 03/06
Christian Sandweg	since 10/06
Sebastian Schäfer	since 06/06
Thomas Schneider	until 10/05
Helmut Schultheiß	until 09/05
Georg Wolf	since 10/06

Engineers and Technicians

Jörg Elmer (Rheinbreitbach)
Bernd Pfaff
Dipl.-Ing. (FH) Dieter Weller

Secretaries:

Sibylle Müller
Heike Schuster (Forschungsschwerpunkt MINAS) until 09/06

2.2 Visiting scientists, postdoctoral fellows and exchange students

Prof. Andrei Slavin, University of Rochester, Michigan, U.S.A. 25.07.06 - 28.07.06

Andrei spent the major part of his sabbatical leave with our group. His stay was supported by our Graduate School ("Graduiertenkolleg"). He was delivering a course of lectures on the nonlinear dynamics of spin waves in magnetic films and on generation of microwave spin waves by spin-polarized current. During the second part of his visit he was working on the theory of Bose condensation of spin waves in ferrite films.

Steven Crane, Ph.D. student, University of Calofornia, Berkeley, USA 22.05.06 - 19.08.06

Steven founded for summer research as a NSF Fellow, joint us for a short period to work on Brillouin light scattering spectroscopy of complex oxide multiferroic films.

Dr. Boriss Marhov, Westfälische Wilhelms-Universität Münster 07.08.06 - 09.08.06

Boriss's visit was part of a close collaboration with the group of Sergej Demokritov concerning the growth of smooth metallic layers for the EU Marie Curie Research Training Network ULTRASMOOTH.

2.3 Guest seminars

Prof. Gisela Schütz 28.11.2005	MPI für Metallforschung, Stuttgart *Magnetismus im Röntgenlicht* Physikalisches Kolloquium
Dr. Martin Jourdan 28.11.2005	Johannes Gutenberg Universität, Mainz *Herstellung epitaktischer CCFA-Schichten* Sonderseminar
Dr. Markus Bolte 30.11.2005	Universität Hamburg *Micromagnetic simulation of spin wave eigenmodes in Landau-domain structures* Sonderkolloquium
Prof. Christian Back 12.-13.12.05	Universität Regensburg *Magnetisierungsdynamik: Als die magnetischen Bilder laufen lernten* Physikalisches Kolloquium
Amilcar B. Pinto 19.12.05	Kungl Tekniska Högskolan, Stockholm, Sweden *Magnetic properties of Cu doped ZnO films* Sonderseminar
Prof. Michael Fleischhauer 23.01.2006	TU Kaiserslautern *Quantum optics* Sonderseminar
Dr. Hubert Grimm 30.01.2006	Sensitec Naomi, Mainz *Magnetic sensors* Sonderseminar
Prof. Holger Schmid 29.05.2006	University of California, Santa Cruz, USA *Ultrafast magnetization dynamics in individual nanomagnet* Sonderseminar
Steven Crane 19.06.2006	UC Berkeley, USA *Multiferroic nanostructured films* Sonderseminar

2.4 Visits of group members at other laboratories

Patricia Martín Pimentel	Sensitec-Naomi Mainz 14.02-24.02.06 Host: Dr. H. Grimm
Patricia Martín Pimentel	IMEC, Leuven, Belgium 17.07-25.07.06 Host: Dr. L. Lagae
Alexander A. Serga	Taras Shevchenko National University of Kiev, Uraine 19.06.-28.06.2006 Host: Prof. Dr. G. Melkov
Alexander A. Serga	Taras Shevchenko National University of Kiev, Uraine 18.09.-25.09.2006 Host: Prof. Dr. G. Melkov
Alexander A. Serga	Taras Shevchenko National University of Kiev, Uraine 28.10.-04.11.2006 Host: Prof. Dr. G. Melkov

2.5 Group member photo gallery

Prof.Dr. Yasuo Ando
Guest scientist

Christian Bayer
Ph.D. student

Andreas Beck
Ph.D. student

Sebastian Becker
Ph.D. student

Steffen Blomeier
Ph.D. student

Ulla Böde
Ph.D. student

Dr. Patrizio Candeloro
Postdoc

Jörg Elmer
Technician

Oksana Gaier
Ph.D. student

Dr. Jaroslav Hamrle
Postdoc

Sebastian Hermsdörfer
Ph.D. student

Prof. Dr. Burkard Hillebrands
Group leader

Dirk Hoffmann
Ph.D. student

Lisa Kleinen
Ph.D. student

Dr. Britta Leven
Senior scientist

Maciej Oskar Liedke
Ph.D. student

Patricia Martín Pimentel
Ph.D. student

Dr. Seong-Gi Min
Postdoc

Sibylle Müller
Secretary

Hans Nembach
Ph.D. student

Timo Neumann
Ph.D. student

Bernd Pfaff
Technician

Christian Sandweg
Diploma student

Sebastian Schäfer
Diploma student

Thomas Schneider
Ph.D. student

Helmut Schultheiß
Ph.D. student

Heike Schuster
Secretary

Dr. Alexander Serga
Senior scientist

Dr. Natalia Sergeeva
Postdoc

Markus Weber
Ph.D. student

Dieter Weller
Mechanical engineer

Georg Wolf
Diploma student

Chapter 3: Research Topics

The field of magnetism in films and multilayers is still a strongly developing area in modern solid state physics. This is caused both by the challenging developments in the discovery and understanding of the basic physical phenomena, and by the strong impact into industrial applications in the areas of sensors and information storage technology. New mechanisms like interlayer exchange coupling, the giant magnetoresistance effect, the room-temperature tunneling magnetoresistance effect, and, since very recently, spin current phenomena were discovered all within the last one and a half decade. Applications based on these effects were developed, like the magnetic read head based on the giant magnetoresistance effect found in nearly every hard disk drive sold nowadays. The combination with microelectronics, the so-called field of magneto-electronics is strongly expanding and bridging the gap between conventional magnetism and semiconductor physics in view of potential applications in sensor devices and magnetic random access memories, as well as new fields such as magnetic logic.

Most of our research projects are in this field. A main focus is on spin dynamics. We study the eigen-frequency spectrum of excitations of the magnetization on the frequency scale using the Brillouin light scattering technique, and the temporal evolution by time resolved magneto-optic methods. We investigate high frequency properties like spin waves, time dependent magnetization effects, and fast magnetic switching. Recently, our focus shifted strongly towards transport phenomena using linear and nonlinear spin waves.

A key issue is the fabrication of high-quality epitaxial film and multilayer systems and devices using molecular beam epitaxy as prototype systems to study fundamental problems.

In the field of applications we address problems of fast magnetic switching and the exchange bias effect. We transfer our results into actual devices by working closely together with industrial partners.

Magnetic films are very attractive and versatile nonlinear media. Considering spin waves in films as one example of nonlinear waves we study nonlinear effects which are of a great importance for nonlinear science in general.

As a second working area we develop and investigate carbon films for medical applications in the framework of the Institute for Thin Film Technology in Rheinbreitbach.

Overview on projects

1) Epitaxial magnetic films and multilayers: growth, structure and magnetic properties

The preparation of samples with highest possible structural quality and characterization is very important to be able to study magnetic phenomena with the required precision. We achieve this by using molecular beam epitaxy employing the standard *in-situ* methods for chemical and structural analysis. They comprise Auger spectroscopy for chemical analysis, low and high energy electron diffraction, and *in-situ* scanning tunneling and atomic force microscopy. To characterize the magnetic properties we perform *in-situ* Brillouin light scattering spectroscopy and magneto-optic Kerr effect magnetometry. *Ex-situ*, the samples are investigated using Brillouin light scattering spectroscopy, vector Kerr magnetometry, vibrating sample magnetometry, and more. Scientific subjects are magnetic anisotropies induced at interfaces and by controlled

defects, and interlayer coupling effects between magnetic films in multilayers. Special attention is paid to the interplay between the morphology at the interfaces (atomic defects, steps, roughness and interdiffusion) and the magnetic properties.

2) Surface smoothing

It is very important to fabricate films and multilayers with maximum degree of smoothness. Undesirable roughness, for example, results in a reduced figure of merit in magnetoelectronic devices. We develop a technology to smooth surfaces of films after their preparation. For this purpose we use low-energy beams of argon ions. Mono-energetic, low-energy ions allow for a very controllable smoothing process of the surface without creation of an essential number of defects.

3) Dynamic magnetic properties of laterally patterned nanostructures

We investigate the basic magnetic properties of systems patterned on the micrometer to nanometer scale. In particular we focus on the domain structure and the change in the spin wave mode spectrum due to lateral confinement effects. We have developed a Brillouin light scattering setup, operating in a Fourier microscope like mode, to obtain sub-micrometer scale spatial information about the distribution of dynamic excitations in small magnetic objects. We also developed a micro-focus Brillouin light scattering system to investigate single magnetic elements. Using these methods we have observed lateral quantization of spin waves in magnetic stripes and rectangular elements. Main results are the observation of quantized modes and of edge modes existing in areas with a large internal field gradient, and static and dynamic coupling effects between magnetic objects. The experiments are accompanied by numerical simulations. A new area is the spin-wave tunneling effect and applications to spin wave logic.

4) Nonlinear properties of high-amplitude spin waves

Spin waves with high precession angles are an interesting object for the investigation of general effects of nonlinear wave propagation in dispersive, anisotropic, and dissipative media. Contrary to nonlinear optical pulses, the spectrum of spin waves can be easily manipulated, by, e.g., changing the orientation and the value of the applied magnetic field. In addition spin waves are much slower than light pulses making their observation easier.

Using the time-resolved Brillouin light scattering technique developed in our lab, we measure the intensity distribution of spin waves propagating in a magnetic film with spatial and temporal resolution. Central problems are: the amplification of spin waves in the linear and nonlinear intensity regimes, the formation of instabilities (e.g. self-focusing), the propagation of nonlinear excitations (solitons, magnetic “bullets”) and excitations in nonlinear media with a nontrivial topology such as rings. An important development of these studies is the investigation of self-generation of solitons and bullets in loops with an electronic feedback, the development of a spin wave soliton “laser”, and the discovery of symmetry-breaking spin wave modes like the “Möbius” solitons.

5) Fast magnetic switching

For memory devices it is of special importance how fast and secure magnetic domains can be written and the magnetization of a single magnetic object can be reversed. The corresponding time scale is in the picosecond to nanosecond regime. In order to investigate these phenomena a time-resolved scanning magneto-optic Kerr microscope has been constructed. The time

evolution of the magnetization is sensed stroboscopically. The magnetization dynamics, spin wave propagation effects and in particular the switching behavior of thin magnetic films and nanostructures are investigated.

6) Magnetic nanopatterning

Ion irradiation is an excellent tool to locally modify magnetic properties on the sub-micrometer scale, without substantially affecting the surface topography. This effect is used to magnetically pattern ultrathin films and multilayers using resist masks patterned by electron beam lithography. The major difference between this technique and conventional lithographic techniques is that the environment of the nanostructures can also be magnetic (paramagnetic, antiferromagnetic). A focus is on coupled magnetic systems, such as exchange bias bilayers and exchange coupled trilayers.

7) Exchange bias systems

The investigation of exchange bias systems is of fundamental as well as technological importance. The effect is a shift of the hysteresis loop along the field axis, and it appears in multilayers of coupled ferromagnetic and antiferromagnetic films. In particular we study structurally well characterized epitaxial bilayers. The role of defects and interfacial mixing is investigated using ion irradiation in order to artificially create disorder. Ion irradiation techniques are also applied to modify the magnitude and direction of the exchange bias field. TEM studies are carried out to investigate the structural and magnetic properties as well as their dependency on the irradiation with He^+ and Ga^+ ions. A picosecond all-optical pump-probe setup was developed to study thermal activated unpinning of the exchange coupling at the FM/AF interface. This is of high technological interest, especially for magnetic sensor and storage applications.

8) Biofunctionalized surfaces for medical applications

Amorphous thin carbon films are known to be very biocompatible, and they can be prepared by various deposition techniques to qualify for miscellaneous applications in the biological and medical field. At the Institute for Thin Film Technology we develop in close collaboration with our spin off company NTTF GmbH biocompatible and biofunctionalized surfaces for medical implants, surgical instruments and cellbiological equipment. Currently we are working on carbon coatings for endwelling catheters and cell culture dishes (both made of temperature sensitive polymers) as well as on the development of diffusion barrier coatings on polymers.

Chapter 4: Equipment

A) Preparation and characterization of thin films and multilayers

1. multi–chamber molecular beam epitaxy system (Pink GmbH) comprising
   a. deposition chamber
      (electron beam and Knudsen sources, RHEED, LEED, Auger)
   b. scanning tunneling and needle sensor microscopy chamber
      (*in-situ* STM/needle AFM, Omicron)
   c. Brillouin light scattering and Kerr magnetometry chamber
      (magnetic field 1.2 T, temperature range 80 – 400 K)
   d. load lock chamber
   e. preparation chamber
      (optical coating, heating station 2300°C)
   f. transfer chamber
   g. atom beam reactor chamber with *in-situ* four point probe resistance measurement stage
2. two-chamber UHV multideposition system
   a. deposition chamber
      (electron beam and Knudsen sources, LEED, Auger)
   b. ion beam chamber with fine focus noble gas keV ion source (Omicron), ion beam oxidation module and mask system
3. two-magnetron sputtering system for hard coatings
4. atomic force microscope (Solver, NT-MDT)
5. clean room facility with flow box, spin coater, etc.

B) Magnetic characterization

1. vector Kerr magnetometer
   (longitudinal and transverse Kerr effect, magnetic field 1.2 T, temperature range 2 – 350 K, automated sample positioning)
2. time-resolved vector Kerr magnetometer (10 ps time resolution and microwave setup for generation of short field pulses)
3. scanning Kerr microscope with time resolution
4. picosecond all-optical pump-probe setup (adjustable delay up to 6 ns; ps-laser Lumera Lasers GmbH)
5. magnetic force microscope with magnet (NT-MDT)
6. two Brillouin light scattering spectrometers, computer controlled and fully automated (magnetic field 2.2 T) with stages for
   a. low temperature measurements (2 – 350 K)
   b. space-time resolved measurements for spin wave intensity mapping (resolution 50 µm, 0.83 ns)

c. micro-focus measurements (focus diameter 0.3 µm)
d. *in-situ* measurements
e. elastic measurements

7. microwave setup (up to 32 GHz) comprising a network analyzer, microwave amplifiers, modulators, pulse generators, etc.
8. magnetotransport setups (magnetic field 1.5 T, temperature range 20 – 400 K)

C) Equipment at the Institute for Thin Film Technologies (IDST), Rheinbreitach

1. Preparation of thin films:
   a. chemical vapor deposition (CVD) facility
   b. physical vapor deposition (PVD) facility
   c. plasma enhanced CVD (PECVD) facilities with an inductively coupled rf-plasma beam source and several magnetrons of different sizes
2. Surface and thin film analysis:
   a. profilometer: measurement of coating thickness and roughness determination of intrinsic stress and Young modulus
   b. Ball on Disk: measurement of friction coefficient analysis of surface friction
   c. Revetest: determination of adhesive strength analysis of microcracks
   d. microindention: determination of plastic and elastic microhardness (Vickers)
   e. optical contact angle measurement: determination of solid surface free energy and surface tension evaluation of hydrophobicity and hydrophilicity
   f. reflection- and transmission-spectroscopy (UV-VIS): optical measurements with wavelength range from 185 nm to 915 nm (resolution 1 nm), determination of absorption coefficient and optical gap (Tauc)
   g. (environmental) scanning electron microscopy (ESEM)[1]: comprehensive structural microanalysis of conducting, isolating, anorganic, organic and wet samples
   h. energy dispersive X-ray microanalysis (EDX)[1]: non-destructive fast analysis of elements
   i. neutron activation analysis (NAA)[2]: qualitative und quantitative analysis of main and trace components
   j. elastic recoil detection analysis (ERDA)[2]: analysis of trace elements with depth resolution analysis of hydrogen content
   k. Rutherford Backscattering (RBS)[2]: analysis of trace elements with depth resolution
   l. synchrotron-X-ray-fluorescence (SYXRF)[2]: non-destructive analysis of elements

[1] in cooperation with NTTF GmbH, Rheinbreitbach

[2] (accelarator enhanced analysis in cooperation with the accelarator laboratories of the Universities of Munich, Bonn and Cologne

Chapter 5: Transfer of Technology

1. Magnetism

With our facilities within the Department of Physics at the University of Kaiserslautern we offer consultance and transfer of technology in the areas of thin film magnetism, magnetic film structures and devices, magnetic sensors, and in corresponding problems of metrology.

We are equipped to perform magnetic, transport, elastic and structural measurements of films and multilayer systems.

This is in detail:

- magnetometry using vibrating sample magnetometry, Kerr magnetometry, Brillouin light scattering spectroscopy
- magnetic anisotropies, optionally with high spatial resolution
- magneto-transport properties
- test of homogeneity of magnetic parameters
- exchange stiffness constants in magnetic films
- elastic constants
- surface topography

2. Institut für Dünnschichttechnologie (IDST) - Transferstelle der Technischen Universität Kaiserslautern, Rheinbreitbach

(Institute for Thin Film Technology - Center for Technology Transfer of the University of Kaiserslautern, Rheinbreitbach)

As part of technology transfer the Institute of Thin Film Technology (IDST) offers among other activities

- consultance in tribological problems
- development of product specific coatings
- optimization of coatings especially for medical applications
- coating of polymers and temperature sensitive materials
- coating of samples and small scale production series
- management for R&D-projects

The institute is located in Rheinbreitbach about 20 km south of Bonn in the Center for Surface Technologies (TZO) to support the economy in the northern part of the Rheinland-Pfalz State.

Address:

Institut für Dünnschichttechnologie
Maarweg 30-32
53619 Rheinbreitbach, Germany

Scientific director:

Prof. Dr. B. Hillebrands phone: +49 631 205 4228
e-mail: hilleb@physik.uni-kl.de

Contact:

Lisa Kleinen phone: +49 2224 900 693
fax: +49 2224 900 694
e-mail: kleinen@physik.uni-kl.de

Please contact us for more information.

Chapter 6: Experimental Results

A. Dynamic Magnetic Phenomena

6.1 Spin-wave quantization in nanoscaled magnetic rings

H. Schultheiß, P. Candeloro, S. Schäfer, P.A. Beck, B. Leven, and B. Hillebrands[1]

The spin-wave eigenmode spectra of small magnetic elements such as stripes [1], rectangular elements [2], disks and rings [3–8] were discussed in detail in the past. Nevertheless the topic of spin wave coherence - also in the case of thermally activated spin waves - was never discussed, even though this is an essential requirement for the existence of an eigenmode system. When the spin waves are confined in magnetic elements with lateral dimensions smaller than the coherence length, the reflections at the limiting boundaries can lead to constructive interference, and to the creation of standing spin waves. In contrast no eigenmode system can be created when the lateral sizes of the microstructures are larger than the coherence length, because the spin waves cannot propagate coherently from one turning point to the other. In this case the spin wave properties will be mostly determined by the local internal field and the frequency of the spin waves will change continuously with the position inside the magnetic element, according to the variations of the internal field.

In the last decade magnetic eigenmodes, due to coherent spin waves, have been widely investigated in microstructures with different geometries using a variety of experimental techniques [1, 3, 4, 7]. Among the observations reported so far, it is worthy to mention that not only the lateral confinement of the structures, but also inhomogeneous internal fields can create the suitable conditions for the occurrence of lateral standing spin waves [9, 10]. However, all the past works are either concerned with confined or unconfined spin waves. The breakdown of an eigenmode system due to the finite coherence length has not been investigated in detail. It is advantagous for the study of coherence effects that eigenmodes with distinct frequencies are located in different spatial regions. More precisely a magnetic element with a gradually changing internal magnetic field as a function of the position is needed so that the eigenmodes are clearly separated in space and frequency in order to detect the separation with the experimental setup.

Ring shaped elements magnetized in the so-called onion state can fulfill these requirements. The magnetization distribution for this domain state is shown in Fig. 1a for a ring with an outer diameter D of 2 µm, a width w of 400 nm and an externally applied field of 400 Oe. The inhomogeneity of the internal field can be tuned by changing the geometry of the ring structure, like the outer diameter and width, or by varying the externally applied field. The distribution of the internal field for rings with $D = 1, 2$ and 3 µm, $w = 400$ nm and an externally applied field of $H = 400$ Oe is shown in Fig. 1b as a function of the azimuthal angle α. The values of the internal magnetic field are extracted from OOMMF [11] simulations along a circle with radius $R = \frac{D}{2} - \frac{w}{2}$, i.e., along the middle of the ring. In the pole regions of the ring ($\alpha = 0^\circ$ and 180° in Fig. 1b), the internal field is drastically reduced by the demagnetizing field, which arises from the non-zero magnetization component perpendicular to the ring boundaries. In the equatorial regions ($\alpha = 90^\circ$ and 270°) the

[1] In collaboration with H.T. Nembach, NIST, Boulder, Colorado, USA, A.N. Slavin, Department of Physics, Oakland University, Rochester, Michigan, USA.

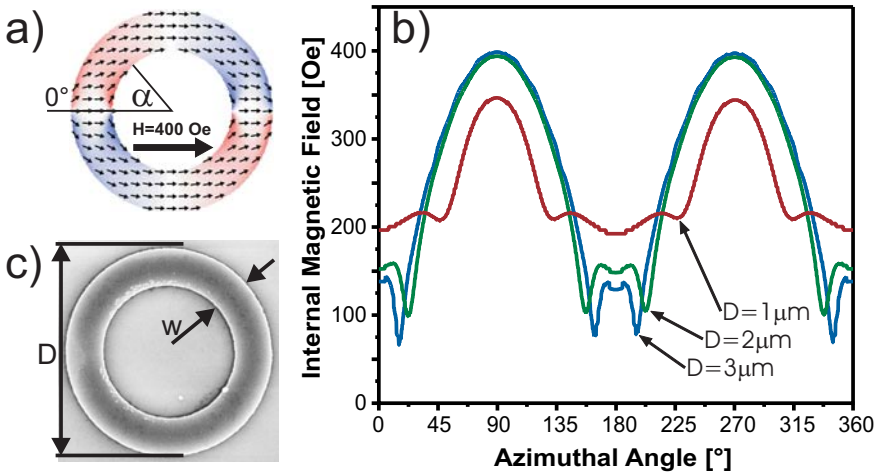

Fig. 1: (a) Equilibrium position of the magnetization calculated with OOMMF [11] for a ring with $D = 2\,\mu m$ diameter, width $w = 400\,nm$ and an externally applied field of $H = 400\,Oe$. The domain pattern for this field is the so-called onion state. Starting point for the azimuthal angle is the pole region where the magnetization is aligned perpendicular to the ring perimeter. (b) Distribution of the internal magnetic field along path with radius $R = \frac{D}{2} - \frac{w}{2}$ for three different diameters of $D = 1,2$ and $3\,\mu m$ and constant width of $w = 400\,nm$. (c) SEM image of a $Ni_{81}Fe_{19}$ring structure with diameter $D = 2\,\mu m$ and width $w = 400\,nm$ prepared by molecular beam epitaxy and electron beam lithography and lift-off technique.

magnetization is aligned parallel to the ring perimeter; consequently at these positions the internal field is determined mostly by the external one. As shown in Fig. 1b, the variation of the diameter of the rings changes the gradient of the internal field and therefore the difference of the internal field between the pole and the equatorial region.

Here we report about microfocus Brillouin light scattering (BLS) spectroscopy on permalloy rings with outer diameters of $D = 1,2$ and $3\,\mu m$ and a width of $w = 400\,nm$. The structures were prepared by electron beam lithography and lift-off technique. The $Ni_{81}Fe_{19}$ layer with a thickness of $t = 15\,nm$ was grown by molecular beam epitaxy in an UHV system. A SEM image of one of the investigated ring structures is depicted in Fig. 1c. The microfocus BLS enables for the determination of the excitation spectrum of single magnetic elements with a spatial resolution better than 300 nm and a frequency resolution of 0.1 GHz. To measure the spin waves inside small magnetic rings we scanned along a circle around the ring center with a radius $R = \frac{D}{2} - \frac{w}{2}$ in azimuthal direction. At each scanning point a BLS spectrum was acquired. Figure 2a-c shows the results for rings with diameters of $D = 1$, 2 and $3\,\mu m$, respectively, and a constant ring width of $w = 400\,nm$. In the figure, each line parallel to the frequency axis is one BLS spectrum, with the greyscale code proportional to the intensity of the peaks. At first glance the frequency follows the magnitude of the internal field (see Fig. 1b) along the ring perimeter. In the pole regions, where the internal field is smaller due to the demagnetizing field, the measured spin waves have lower frequencies than in the equatorial regions, where the internal field nearly matches the externally applied field of 400 Oe. In the high field regions ($\alpha = 90^\circ$ and 270°) higher satellite modes are observed; although they have smaller intensities they match the angular dependence of the lower modes. The anti-Stokes BLS spectra for the different ring geometries at $\alpha = 270^\circ$ are plotted in the subpanels d-f of Fig. 2, corresponding to a cross section of the greyscale map in the equatorial region. The higher satellite modes are marked with arrows and will be discussed below.

In the following, we focus on the spatial dependence of the spin wave frequencies when increasing the diameter of the ring structures from $1\,\mu m$ to $3\,\mu m$. In the case of the $1\,\mu m$ ring (Fig. 2a) we

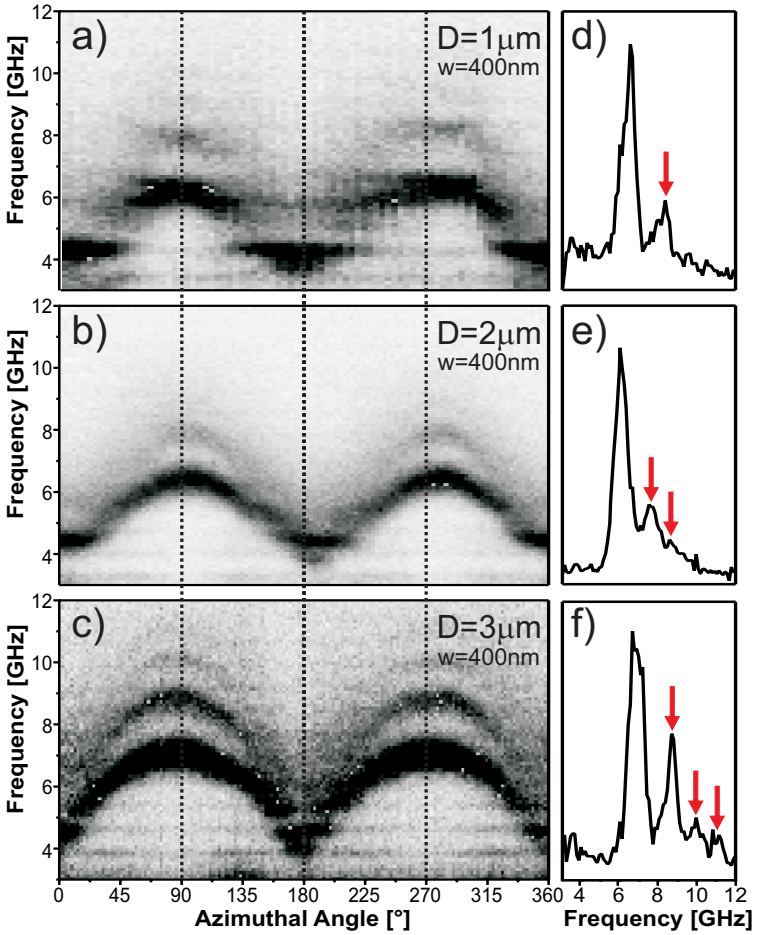

Fig. 2: (a)-(c) The greyscale maps represent the microfocus Brillouin light scattering spectra for rings with outer diameter of 1,2 and 3 µm respectively and constant width of 400 nm as a function of the azimuthal angle. Black indicates high microfocus-BLS signal. The scans were performed along the middle of the rings. Start point is at 0° in the pole region of the onion state. (d)-(f) BLS spectra for three different outer diameters measured at 270° in the equatorial region. Arrows are indicating the higher modes that are explained in the text.

observe constant spin wave frequencies as a function of the azimuthal angle. When continuously changing the position on the ring from the pole region to the equatorial region, the measured spin-wave frequency jumps from 4.3 GHz to 6.2 GHz; moreover higher modes appear as shown in Fig. 2d. On the contrary, for the 3 µm ring (Fig. 2c) we see a continuous change of the spin wave frequency as a function of the azimuthal angle. We remark that an eigenmode system (i.e., standing waves) is expected to exhibit constant frequencies inside the confining region. While this is observed for the 1 µm ring, in agreement with recent works [4–8], no angular regions with constant frequencies can be observed between the poles in the case of the 2 µm and 3 µm rings. This behaviour indicates that the coherence length of the spin waves is not large enough to produce constructive interference in azimuthal direction, and as a result only incoherent excitations are observed in azimuthal direction. On the other hand, standing waves can still arise in radial direction because of the smaller confining length; hence the higher modes observed in the equatorial region can be identified as radial eigenmodes with larger quantization numbers.

This conclusion is also supported by the results of micromagnetic simulations. The free code OOMMF [11] is used to calculate the dynamic response of the rings after a field pulse of short

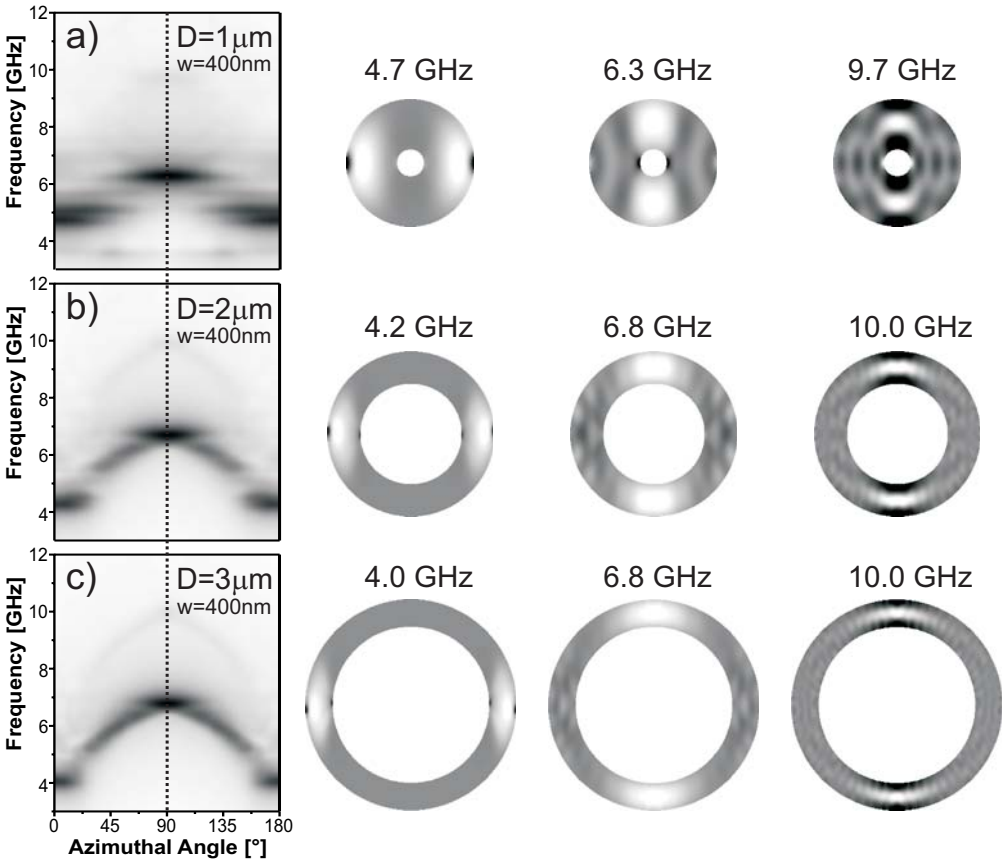

Fig. 3: Micromagnetic simulations for the 1 µm (top row), 2 µm (middle row) and 3 µm (bottom row) diameter rings. The equilibrium configuration of each ring is excited through a field pulse and the following dynamical magnetic response is locally analyzed via Fourier transformations. The greyscale maps on the left side summarize the power spectra intensities as a function of the azimuthal angle and the frequency. While for the 1 µm ring (panel a) two modes with constant frequencies are located in the polar and equatorial regions, respectively, for the 2 µm and 3 µm rings (panels b and c) a continuously changing frequency is observed between the same regions. For each ring, the mode profiles corresponding to the frequencies with larger intensities are also reported and they confirm the spatial localization of the modes already observed in the greyscale maps. Furthermore, the number of radial nodes of the modes located in the equatorial region (middle and last columns) suggests that the higher frequency modes are due to quantization in radial direction.

duration (0.01 ns) and small amplitude (1 Oe). In the calculations, an external field of 400 Oe is applied along the *x*-axis ($\alpha = 180^\circ$), while the field pulse is parallel to the *y*-axis ($\alpha = 90^\circ$). The other parameters used for the calculations are 650 G for the saturation magnetization (smaller than the literature value for permalloy due to reasons discussed below), an exchange stiffness of $1.6 \cdot 10^{-6}\,\mathrm{erg \cdot cm^2}$ and a gyromagnetic ratio of $1.76 \cdot 10^{-2}\,\frac{\mathrm{GHz}}{\mathrm{Oe}}$. The simulations yield the time evolution of the magnetization configuration inside the ring. These data are transformed point-by-point to the frequency domain through a Fourier analysis. In panels a-c of Fig. 3 the intensities of the Fourier transformations are reported as a function of both the azimuthal angle (abscissa axis) and the frequency (ordinate axis) in a greyscale plot, similar to the presented BLS spectra. When comparing the simulation results with the experimentally obtained data (see Fig. 2a-c) it can be seen that the BLS spectra are fully corroborated. Due to the uniform spatial distribution of the pulse only radial modes with an odd quantization number can be excited. Therefore the second highest order mode observed in the experiment cannot be seen in the simulations. This dependence of the excited modes on the symmetry properties of the pulse is well known and was reported previously [12]. Figure 3 also shows the spatial distribution of the most significant modes

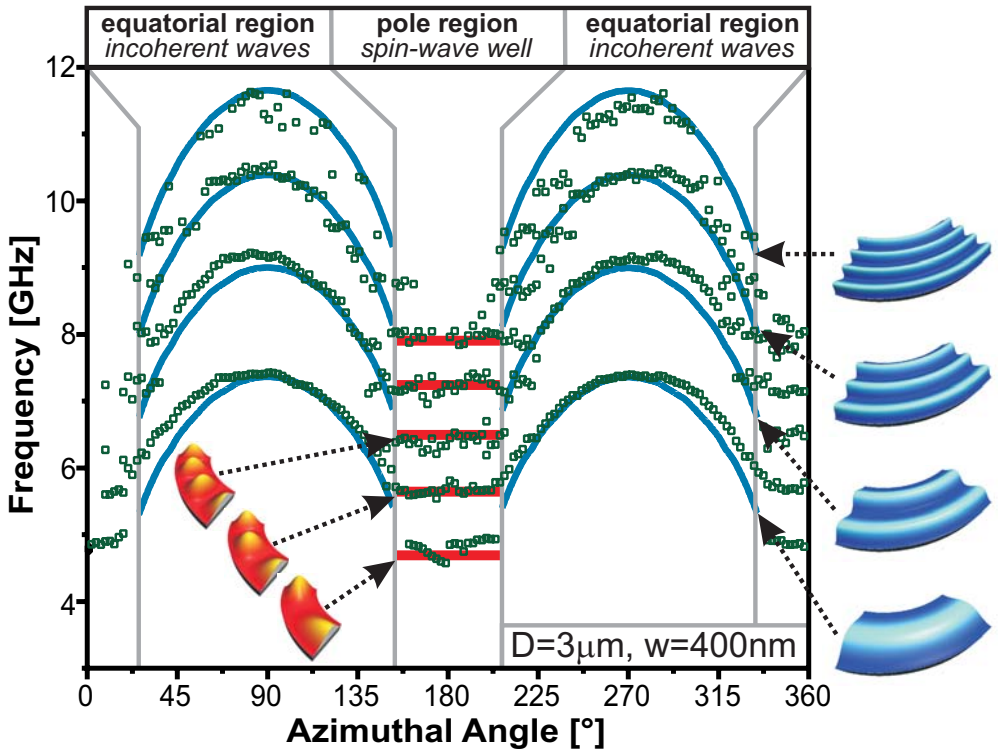

Fig. 4: Spin-wave resonances as a function of the azimuthal position in a ring with diameter $D = 3\,\mu\text{m}$ and width $w = 400\,\text{nm}$ at an externally applied field of 400 Oe measured with microfocus BLS. The data plotted with open boxes are extracted out of the raw data presented in Fig. 2 by the means of fitting. The data can be splitted in two regions of different spin-wave character. In the equatorial regions the frequencies are changing continuously as a function of the position whereas in the pole regions resonances with constant frequencies as a function of position are observed. The lines are representing our calculations for the different ring segments. The calculation shows that spin waves are only quantized in radial direction in the equatorial region as indicated with the schematic mode profiles on the right side of the graph. In the pole region the spin waves are trapped in an effective spin-wave well. The higher frequencies correspond to spin waves with a higher quantization number in azimuthal direction.

observable in the greyscale maps. Concerning the modes located in the equatorial region, the profiles of the lower frequency modes exhibit only one node, while three nodes in radial direction are present for the higher modes. This is a clear indication that the higher modes observed in the experiments are due to quantization effects along the radial direction.

A more quantitative analysis is carried out for the $D = 3\,\mu\text{m}$ ring. We fitted the experimental frequencies and compared them with calculations based on the spin-wave dispersion equation for thin films [13]. Both the experimental data and the calculated frequencies are reported in Fig. 4. In the following we discuss the details of the performed calculations. In the equatorial region, where the frequencies are changing continuously and the coherence length is not sufficiently long enough in azimuthal direction to lead to standing spin waves, we approximate each section of the ring structure with an infinitely extended stripe aligned tangentially to the ring, as shown schematically in Fig. 5a. Taking into account the effective dipolar pinning [14] of the spin waves at the lateral edges of the stripe, the effective width w_{eff} to be considered is 440 nm instead of the ring width (400 nm). Due to the lack of boundary conditions along the long axis of the stripe no quantization of the azimuthal wave vector is included in the modeling of the spin waves in the equatorial region. The quantization in radial direction is accounted for by the following formula for the radial wave

vector:

$$k_{\mathrm{r}} = \frac{n\pi}{w_{\mathrm{eff}}} \quad . \tag{1}$$

The quantization number $n = 1, 2, 3, \ldots$ starts from 1 because the magnetization is pinned at the ring boundaries due to the effective dipolar pinning and consequently uniform modes are not allowed. For the frequency dispersion of the spin waves in confined magnetic elements in first approximation the dispersion for an infinite in-plane magnetized film, as shown in [13, 15], can be employed. The dispersion relation of the spin waves with the in-plane wave vector $\mathbf{k}$ is

$$\nu_0(k) = \frac{\gamma}{2\pi}\sqrt{\left(H_{int} + \frac{2A}{M_{\mathrm{s}}}k^2\right)\left(H_{int} + \frac{2A}{M_{\mathrm{s}}}k^2 + 4\pi M_s F_{00}(k)\right)} \quad . \tag{2}$$

The matrix element $F_{00}(k)$ of the dipole-dipole interaction is given by:

$$F_{00}(k) = 1 + P_{00}(k)[1 - P_{00}(k)]\frac{4\pi M_s}{H + \frac{2A}{M_{\mathrm{s}}}k^2}\sin^2\theta_k - P_{00}(k)\cos^2\theta_k \tag{3}$$

with:

$$P_{00}(k) = 1 - \frac{1 - e^{-kt}}{kt} \quad . \tag{4}$$

The angle θ_k in Eq. (3) is defined between the in-plane wave vector and the direction of the static magnetization. However, if we assume only wave vectors perpendicular to the approximated stripe, i.e., in the radial direction of the rings, the angle between the wave vector and the magnetization is changing continuously when traveling in azimuthal direction along the ring (Fig. 5b). In order to determine the dependence of θ_k on the azimuthal angle (Fig. 5c), we calculated the equilibrium magnetic configuration for an external field of 400 Oe using the OOMMF [11] code. At the pole regions the magnetization is aligned in radial direction, whereas in the equatorial region it is aligned in azimuthal direction. So, not only the internal field is changing when moving in azimuthal direction, but also the spin-wave character is continuously varying from Damon-Eshbach like spin waves to Backward Volume spin waves. When taking into account both the varying internal field and the magnetization direction, Eq. (1) combined with Eq. (3) yields the dependence of the frequency upon the azimuthal angle for the different radial modes. It is worthy to remark that the azimuthal angle enters Eq. (3) through the variation of the internal field H and the angle θ_{k} between the magnetization and the in-plane wave vector. The results of these calculations for the equatorial region are plotted in Fig. 4 as continuous lines. The only fitting parameter was the saturation magnetization M_{s} and the fit yields $M_{\mathrm{s}} = 650\,\mathrm{G}$. A reduction of M_{s} from the literature value is expected due to heating of the sample in the focus of the laser beam. The area of the focus in the micro-focus BLS setup is about 30.000 times smaller than in a conventional BLS setup. This leads to a significantly higher intensity as the power cannot be reduced by a similar factor due the small cross section of the scattering process. In more detail the material parameters used in the calculations are $1.6 \cdot 10^{-6}\,\mathrm{erg \cdot cm^2}$ for the exchange stiffness A and $1.76 \cdot 10^{-2}\,\frac{\mathrm{GHz}}{\mathrm{Oe}}$ for the gyromagnetic ratio γ. Note that except for the adjustment of M_{s} there are no free parameters in the calculation of the spin wave frequencies. The excellent agreement of the calculations with the experimental results (Fig. 4) substantiates the existence of spin waves, which are incoherent in azimuthal direction within the equatorial region for the 3 µm diameter rings.

A closer look at the spin-wave frequencies of the 3 µm ring in Fig. 4 reveals further features of the magnetization dynamics other than the above mentioned continuous change of frequency in the equatorial regions. In the pole positions ($\alpha = 0^\circ$ and 180°) we observe several modes with

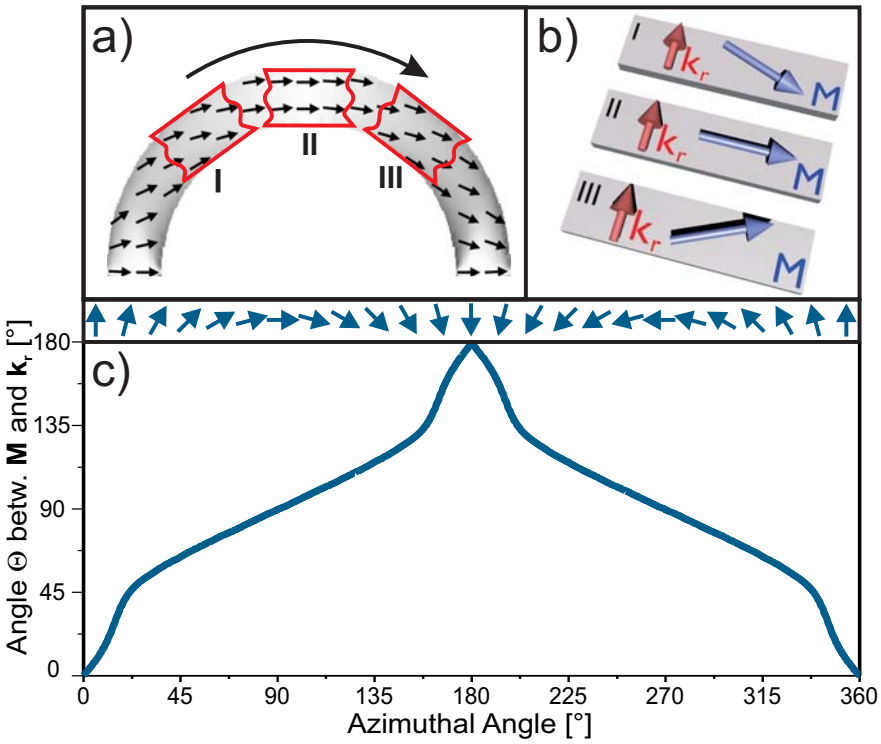

Fig. 5: (a) Schematic description for the model we are using to calculate the incoherent spin waves in the equatorial region of the onion state. At each azimuthal position we approximate the ring with an infinitely extended stripe aligned tangentially to the ring (b). The angle θ between the magnetization and the wave vector in radial direction is changing when moving from position I to III. (c) The exact values for θ are extracted out of an OOMMF simulation of the equilibrium state of the magnetization for an externally applied field of 400 Oe and plotted versus the azimuthal position.

constant frequencies in a narrow angular section around the poles. The frequency spacing of these spin waves differs from the resonances found in the equatorial region, thus indicating that their discretization is not due to confinement in radial direction. These modes correspond to spin waves trapped in spin-wave wells formed by the spatial inhomogeneity of the internal field, as shown in Fig. 1c. For spin waves propagating in azimuthal direction at the poles, that is, perpendicular to the local magnetization, the dispersion of the Damon Eshbach like spin waves will be shifted to higher frequencies because the internal field is increasing. Above a certain value of the field, no real wave vector exists for this spin wave and the propagation in azimuthal direction is not possible anymore. This quantization mechanism is well understood and was first observed in perpendicular magnetized stripes [2]. In Figure 4 the experimental data are shown together with calculations results for the spin wave frequencies in this ring section. Around the pole position we approximated the ring section with a rectangular element having lateral sizes of 440 nm and 1180 nm in radial and azimuthal direction respectively. The length of the rectangular element corresponds to the effective length of the spin wave well. In the first approximation this length is taken as constant for all the modes in the pole region, because of the abrupt change of the internal field. Despite this approximation, the calculated frequencies for higher modes in azimuthal direction are in good agreement with the measured data. As shown by the schematic mode profiles in Fig. 4, we assumed spin waves pinned at the ring boundaries because of the dipolar pinning.

In conclusion we investigated spin wave quantization in small magnetic rings with different diameters by means of micro-focus BLS. In the case of the smallest ring a two dimensional quantization

in radial and azimuthal direction was found, whereas loss of coherence of the spin waves in azimuthal direction was observed for the rings with larger diameter. For calculating the continuously changing spin-wave frequencies in the 3 µm ring we developed a simple model using an infinte extended stripe aligned tangentially to the ring structure. In this approximation we take into account both the inhomogeneous magnetization distribution and the variation of the internal field present in the onion state. Also numerical simulations of the magnetization dynamics carried out with the OOMMF code are in very good agreement with the experimental data for all the investigated ring geometries. All the main features of the measurements, like the mode profiles of the spin waves and frequency distances of higher modes, could be reproduced quantitatively within the simulations.

Support by the Priority Program SPP 1133 of the Deutsche Forschungsgemeinschaft and the NEDO International Joint Research Program 2004IT093, Japan, is gratefully acknowledged. The authors acknowledge S. Trellenkamp and S. Wolf from the Nano + Bio Center, University of Technology Kaiserslautern, for technical support.

References

[1] S.O. Demokritov, Physics Reports, **348**, 441-489 (2001).
[2] J. Jorzick, S.O. Demokritov, B. Hillebrands, M. Bailleul, C. Fermon, K.Y. Guslienko, A.N. Slavin, D.V. Berkov, N.L. Gorn, Phys. Rev. Lett. **88**, 047204 (2002).
[3] M. Buess, R. Hollinger, T. Haug, K. Perzlmaier, U. Krey, D. Pescia, M.R. Scheinfein, D. Weiss, C.H. Back, Phys. Rev. Lett. **93** 077207 (2004).
[4] F. Giesen, J. Podbielski, T. Korn, D. Grundler, J. Appl. Phys. **97** 10A712 (2005).
[5] J. Podbielski, F. Giesen, D. Grundler, Phys. Rev. Lett. **96** 167207 (2006).
[6] G.Gubbiotti, M. Madami, S. Tacchi, G. Carlotti, H. Tanigawa, T. Ono, L. Giovannini, Phys. Rev. Lett. accepted for publication.
[7] X. Zhu, M. Malac, Z. Liu, H. Qian, V. Metlushko, M.R. Freeman, Appl. Phys. Lett. **86** 262502 (2005).
[8] I. Neudecker, M. Kläui, K. Perzlmaier, D. Backes, L.J. Heyderman, C.A.F. Vaz, J.A.C. Bland, U. Rüdiger, C.H. Back, Phys. Rev. Lett. **96** 057207 (2006).
[9] J. Jorzick, S.O. Demokritov, C. Mathieu, B. Hillebrands, B. Bartenlian, C. Chappert, F. Rousseaux, A.N. Slavin, Phys. Rev. B **60** 15194 (1999).
[10] C. Bayer, J.P. Park, H. Wang, M. Yan, C.E. Campbell, P.A. Crowell, Phys. Rev. B **69** 134401 (2004).
[11] M.J. Donahue, D.G. Porter, Report NISTIR 6376, National Institute of Standards and Technology, Gaithersburg, MD (1999).
[12] M. Bolte, G. Meier, C. Bayer, Phys. Rev. B **73** 052406 (2006).
[13] B.A. Kalinikos, A.N. Slavin, J. Phys. C: Solid State Phys. **19** 7013 (1986).
[14] K.Y. Guslienko, S.O. Demokritov, B. Hillebrands, A.N. Slavin, Phys. Rev. B **66** , 132402 (2002).
[15] C. Bayer, J. Jorzick, B. Hillebrands, S.O. Demokritov, R. Kouba, R. Bozinoski, A.N. Slavin, K.Y. Guslienko, D.V. Berkov, N.L. Gorn, M.P. Kostylev, Phys. Rev. B **72**, 064427 (2005).

6.2 Phase-sensitive Brillouin light scattering spectroscopy

T. Schneider, A.A. Serga, and B. Hillebrands

Recently we have reported on the implementation of phase sensitivity into Brillouin light scattering spectroscopy (BLS) [1]. Here we demonstrate the feasibility of phase front visualization. It is known that inelastically scattered light, which is used in the BLS measurements, contains information on both the amplitude and the phase of the scattering wave. However, the detection technique used (photon counting) destroys the phase information. As a result a conventional BLS-setup only allows the measurement of a signal that is proportional to the square of the precession angle of the spin wave, i.e., the spin wave intensity. In order to access phase information, interference between the signal, created by the spin wave under investigation, and a coherent reference signal is used.

Using microwave technique, phase measurements have already been realized, although without spatial resolution. Here the spin waves are detected using a pick-up antenna. The phase sensitivity is realized by mixing the output signal with a coherent electronic reference signal. The resulting interference patterns contain information on both the amplitude and the phase of the signal. Measurements with different phase shifts of the reference signal allow a separation of the amplitude and the phase of the signal (see [2] for an example). However, this approach only allows the measurement of the integral spin-wave characteristics at the position of the antenna, whereas BLS investigations allow the measurement of the phase quantities at any given point of the propagation [3, 4].

In order to access the phase information an interferometric approach is used, in which we spatially combined the signal and reference beam as shown in Fig. 1. In comparison with the classical Mach-Zehnder approach (with separated pathes) this setup has the advantage of better thermal and mechanical stability.

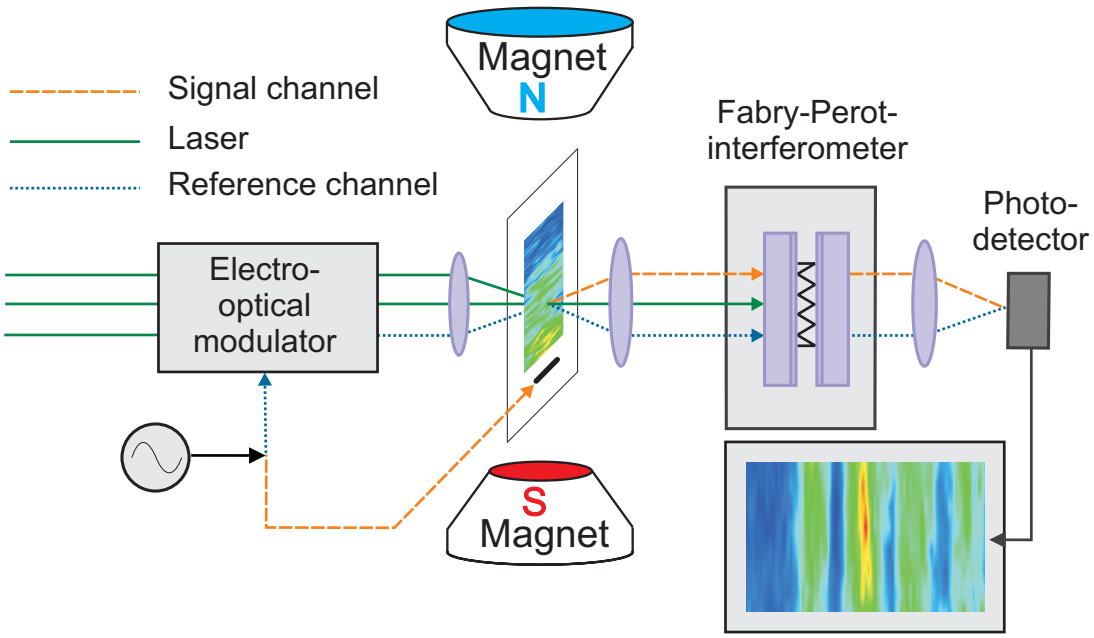

Fig. 1: Experimental setup. Phase sensitivity is realized by interference between the light inelastically scattered by the spin waves (dashed line) and a coherent reference beam (dotted line).

The frequency shifted reference light is created using an electro-optical resonance modulator based on a Lithium Niobat crystal. As this modulator is driven by the same microwave signal that is used for the excitation of the spin waves, coherency between the frequency shifted and the inelastically scattered light is ensured.

It is necessary to note that both the intensities of the reference and the inelastically scattered light are many orders of magnitude lower than the total intensity of the laser beam (approximately 10^{-8}). Thus, second order effects, e.g. inelastic scattering of the reference wave by the spin waves, can be neglected.

The light inelastically scattered from spin waves is rotated by 90° in polarization, whereas for the used electro-optical modulator the modulated beam keeps the polarization of the incident beam. In order to create interference between the two waves, their polarizations should be aligned. This has been realized using an additional polarizer with its polarization plane oriented between 0° and 90°, which was placed in front of the Fabry-Perot-interferometer.

The combination of the phase-sensitivity with the space- and time- resolution descried in [3, 4] is possible. The resulting interference pictures allows us to visualize the phase fronts of a spin wave and thus measure the wavelength with a spatial resolution of approximately 50 µm[1] .

Figure 2 demonstrates the feasibility of phase front measurements. The upper part shows a space-resolved BLS measurement of a spin wave pulse propagating parallel to the magnetic field ($H_0 = 1846\,\mathrm{Oe}$, $\nu = 7.125\,\mathrm{GHz}$) in a YIG waveguide ($4\pi M_S = 1750\,\mathrm{G}$, thickness 4.5 µm) with a mechanical gap (width 20 µm) perpendicular to the propagation direction. A small part of the spin-wave energy is transmitted (i.e., tunnels) through the gap. Therefore most of the intensity is reflected at the gap and forms a standing wave in front of it. The lower part of Fig. 2 shows a phase-sensitive measurement of the same spin wave pulse just before the reflection at the gap. The observed pattern is created by the interference between the reference beam and the inelastically scattered light.

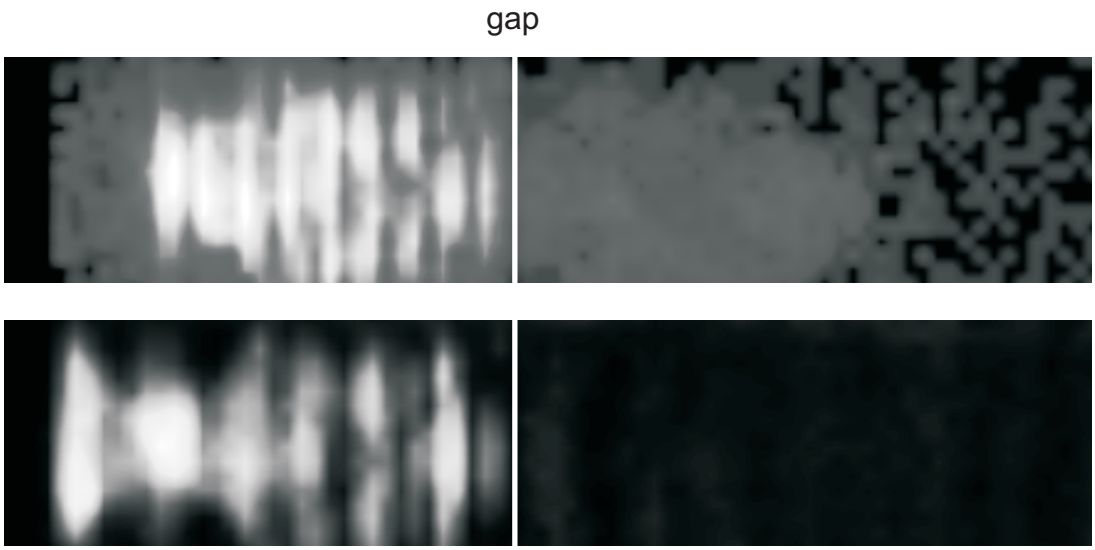

Fig. 2: Upper picture: Space-resolved picture of a spin-wave pulse propagating in a YIG film with a mechanical gap. Reflection at the gap leads to the formation of a standing spin wave in front of it. Lower picture: Phase-sensitive measurement of the same spin wave pulse before the reflection.

[1] In addition the measured phase maps allows us to calculate the phase profiles of the spin waves under investigation. See Section 6.3 for an example of this technique.

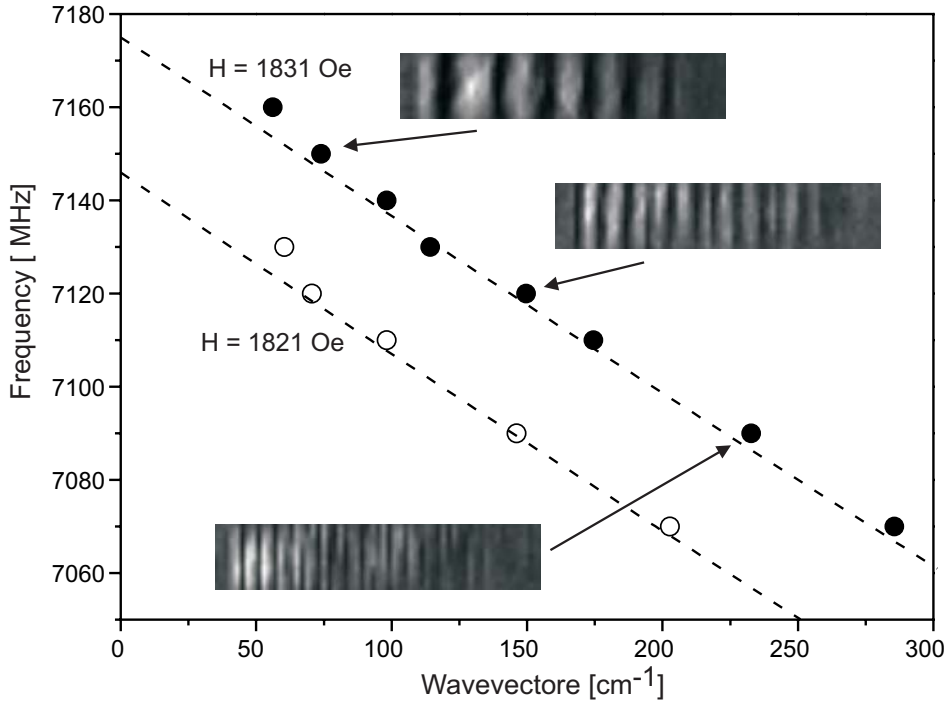

Fig. 3: Measured dispersion relation for BVMSW in YIG. Dashed curves indicate the calculated dispersion relations for the applied bias fields. Insets show typical examples of phase fronts.

Comparison of both intensity maps reveals that the distance between the maxima in the lower panel is twice as long as in the upper one (standing spin-waves).

It is known that the distance between the maxima for a standing wave is half of the wavelength λ, therefore the distance between the maxima in the lower picture is equal to λ. This proves that our new setup is capable of clearly visualizing the phase fronts of a traveling spin wave.

This technique has been used to directly measure the spin-wave wavelength and thus the wavevector $k = 2\pi/\lambda$ as demonstrated in Fig. 3. The Figure shows the measured wavevector for different bias fields B_0 (parallel to the propagation direction, Backward Volume Magnetostatic Spin Waves) and spin-wave frequencies ν. One can observe a good agreement between theoretical (dashed curves, see [5]) and experimental data.

In conclusion we have shown that the phase sensitive BLS can be used to visualize phase fronts and measure the wavelength and thus the wavevector of propagating spin waves.

Support by the Deutsche Forschungsgemeinschaft and the Graduiertenkolleg 792 is gratefully acknowledged.

References

[1] A.A. Serga, T. Schneider, B. Hillebrands, S.O. Demokritov, M.P. Kostylev, Appl. Phys. Lett. , **89**, 063506 (2006).
[2] S.O. Demokritov, A.A. Serga, V.E. Demidov, B. Hillebrands, M.P.Kostylev, B.A. Kalinikos, Nature , **426**, 159 (2003)
[3] M. Bauer, O. Büttner, S.O. Demokritov, B. Hillebrands, V. Grimalsky, Yu. Rapoport, A.N. Slavin, Phys. Rev. Lett. , **81**, 3769 (1998).
[4] O. Büttner, M. Bauer, S.O. Demokritov, B. Hillebrands, Y.S. Kivshar, V. Grimalsky, Yu. Rapoport, A.N. Slavin, Phys. Rev. B , **61**, 11576 (2000).
[5] R.W. Damon, J.R. Eshbach, J. Phys. Chem. Solid, **19**, 308 (1961).

6.3 Phase accumulation and nonlinear phase splitting of spin waves in yttrium-iron-garnet waveguides

T. Schneider, A.A. Serga, and B. Hillebrands[1]

In Section 6.2 of this report we show the feasibility of the visualization and measurement of spin-wave phase fronts using the phase sensitive Brillouin light scattering spectroscopy (BLS). Phase sensitive BLS can also be used to measure the phase profile, i.e., the time dependent phase difference between the exciting microwave signal and the spin wave at any given point of a spin-wave pulse. These profiles can give an insight into a variety of different phenomena, such as the propagation of linear and nonlinear spin waves as well as the formation of bullets or solitons. To obtain the phase profile it is necessary to measure interference maps with different additional phase shifts between the reference and the signal and then calculate the phase (see [1] for a more detailed description of the necessary procedure). Here we report on our investigations of phase accumulation and nonlinear phase splitting observed in propagating spin-wave packets undergoing strong nonlinear decay.

We investigated spin-wave packets in an yttrium-iron-garnet spin-wave waveguide magnetized parallel to the propagation direction. In this geometry the so-called backward volume magnetostatic spin waves (BVMSW) exist [2]. The first measurements have been performed on a long, low intensity spin-wave pulse (200 ns, 7.132 GHz). A long pulse ensures that the wave can be treated as monochromatic and thus the influence of dispersion can be neglected while the low intensity allows us to use a pure linear description. The lower inset in Fig. 1 demonstrates a typical example of a phase profile of such a spin-wave pulse ($H_0 = 1840$ Oe). As expected one observes a rectangular pulse (dashed line in the inset) and a time-independent phase shift with the exciting microwave signal (solid line). If we perform a space-resolved measurement we observe a spin-wave phase accumulation as shown in Fig. 1. One can clearly see that the phase is decreasing linearly with

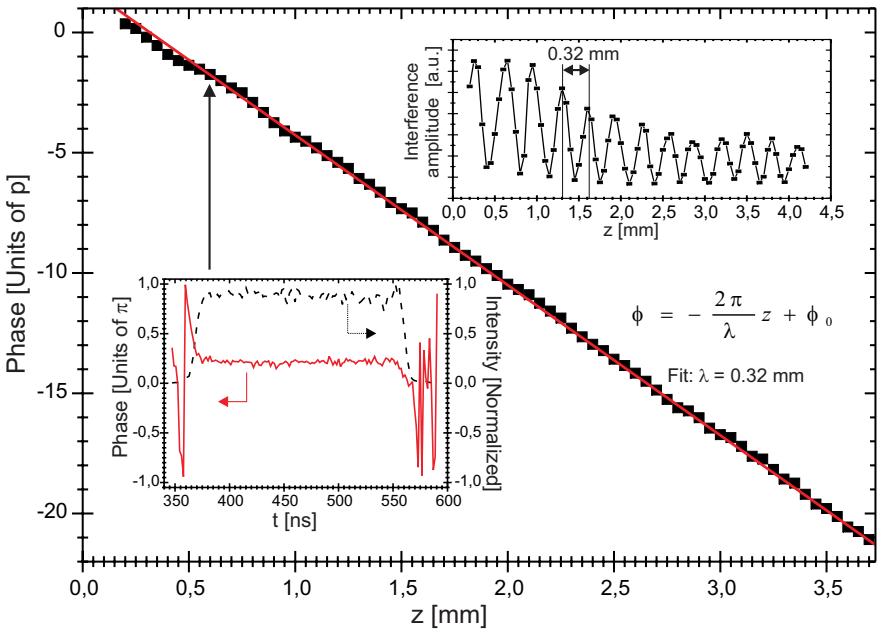

Fig. 1: Linear phase accumulation. Lower inset: Intensity (dashed line) and phase profiles (solid line) versus time of a linear spin wave measured at a distance of 0.6 mm from the exciting antenna. Upper inset: One dimensional interference pattern measured along the long axis of the YIG waveguide. The bias field is 1840 Oe. Pulse duration and carrier frequency are 200 ns and 7.132 GHz, respectively.

[1] In collaboration with M.P. Kostylev, School of Physics, University of Western Australia, Crawley, Australia.

propagation distance. This is in accordance with the theory for BVMSW [2] as group velocity and phase velocity point in opposite directions for this type of wave. The spin wave propagation in the YIG waveguide can be described using a plain wave approximation, thus the phase ϕ should change linearly with the propagation distance z as

$$\phi = k \cdot z + \phi_0 \quad , \tag{1}$$

where $|k| = 2\pi/\lambda$ is the wavevector and ϕ_0 is the initial phase difference between spin wave and reference. This is confirmed by the measurements shown in Fig. 1. Using the fit of Eq. (1) one can calculate the wavelength as $\lambda = 0.32\,\mathrm{mm}$. This value coincides very well with the value estimated from the interference pattern (upper inset of Fig. 1) and thus again confirms the validity of our approach.

If we increase the intensity of the spin wave we observe a change of shape of the spin-wave packet due to nonlinear effects. The lower inset of Fig. 2 demonstrates the shape for such a nonlinear pulse (dashed line, 200 ns, 7.132 GHz as in the linear measurement). One observes a sharp peak at the leading part of the pulse and a flat low intensity area at the tail, which is formed due to a nonlinear decay near the input antenna and caused by four-magnon interaction [3]. While the amplitude in the tail part is decreased the leading part stays at a high intensity since the four-magnon process has not enough time to develop. After the first half millimeter of propagation, the shape stabilizes.

To describe the phase of such a nonlinearly shaped spin wave pulse we must take into account that a high spin wave intensity implies a high angle of precession, leading to a decrease in the static magnetization M_z oriented along the magnetic field H_0. This reduction leads to a down-shift of the dispersion relation for a high-intensity spin-wave pulse as shown in the upper inset of Fig. 2

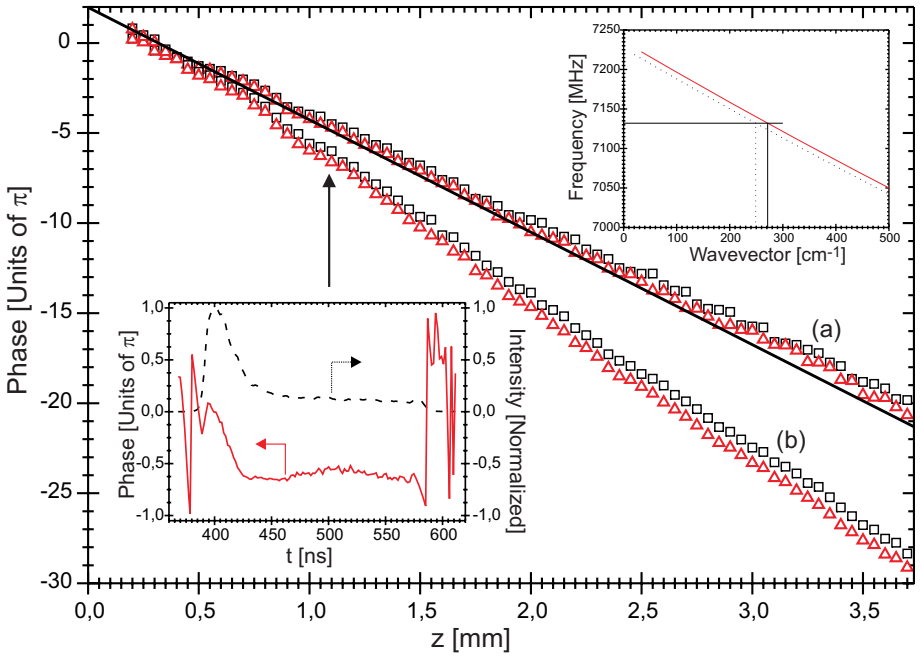

Fig. 2: Nonlinear phase accumulation. Lower inset: Intensity (dashed line) and phase profile (solid line) of a nonlinear spin-wave packet. Upper inset: Spin-wave dispersion for $H_0 = 1850\,\mathrm{Oe}$ for unchanged (solid line) and reduced M_z (dashed line). Pulse duration and carrier frequency are 200 ns and 7.132 GHz, respectively. The bias field is 1840 Oe (a) and 1850 Oe (b), respectively. Rectangles indicate phase at peak of pulse, triangles at tail of pulse. The solid line shows the fit from the linear measurement.

and thus to a lower absolute value for the wavevector in comparison with a low intensity pulse. As described above we can distinguish two areas with highly different intensities in the observed pulse and thus should expect different phase values for the different areas. The phase profile shown in the lower inset of Fig. 2 (solid line) confirms this nonlinear phase splitting. As expected, the phase only changes in the regions where the intensity changes and is practically constant in the tail area.

A space-resolved measurement was performed to observe the phase accumulation both for the nonlinear peak and the linear tail part of the spin-wave pulse. The results can be seen in Fig. 2 for different magnetic fields ((a) $H_0 = 1840\,\mathrm{Oe}$, (b) $H_0 = 1850\,\mathrm{Oe}$). Similar spin-waves intensities were chosen for both fields. To compare with the linear case, the fit according to this measurement is shown as a solid line.

For the first 2.5 mm of propagation one sees nearly no difference between the phase at the tail of the nonlinear spin wave and the one measured in the linear case (the difference at the end of propagation is due to the higher signal-to-noise ratio). In accordance with the inset, the phase at the peak (high intensity part of the pulse) is significantly higher than at the tail of the pulse over the complete propagation range. This corresponds to a lower absolute value for the wavevector and confirms the model given above.

Since the phase accumulation for the nonlinear case depends on the spin-wave amplitude one can expect to see an effect of spin-wave decay on the phase accumulation. During the propagation the peak amplitude decreases due to damping. This leads to an increase of the static magnetization M_z up to the saturation magnetization M_S, which also leads to an increase of $|k|$. After the peak has been reduced to an amplitude for which the reduction of M_z can be neglected one can assume that both the peak and tail have an identical (linear) wavevector.

Figure 3 shows the difference $\Delta\phi$ between the phase at the tail and at the peak of the pulse for different magnetic fields ((a) $H_0 = 1840\,\mathrm{Oe}$, (b) $H_0 = 1850\,\mathrm{Oe}$, similar spin-wave intensity for both fields). If we interpret the derivation of $\Delta\phi$ as wavevector difference Δk we can confirm the effect described above. During the propagation, Δk decreases monotonically until it vanishes after approximately 3 mm for the higher field and 2.5 mm for the lower field. The measured Δk values can be used with the dispersion relation [2] to estimate the necessary decrease of M_z and

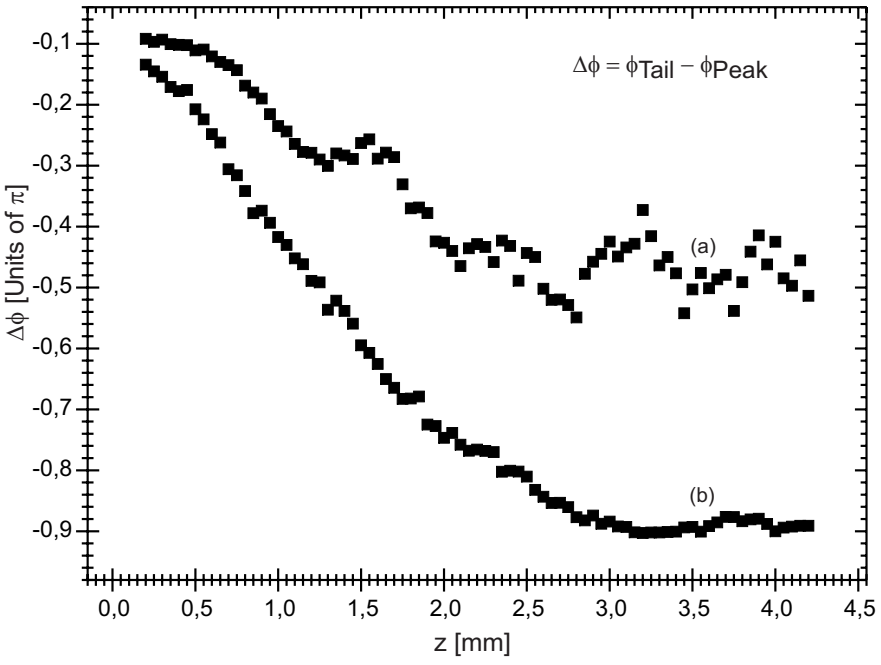

Fig. 3: Phase difference between phase at tail and peak of a nonlinear pulse ($H_0 = 1840\,\mathrm{Oe}$ (a) or $H_0 = 1850\,\mathrm{Oe}$ (b), $\nu = 7.132\,\mathrm{GHz}$).

thus the dynamic component of the total magnetization m at each point of the sample. Performing these calculations with the data shown in Fig. 3 for $H_0 = 1850\,\mathrm{Oe}$ reveals a damping time of approximately 140 ns and an initial precession angle at the peak of approximately 6°. While the damping time is reasonable for YIG the precession angle is rather high, but still acceptable, when taking into account that the peak is nearly unaffected by four-magnon decay as described above and therefore confirms the validity of our model.

It is necessary to note that the wavevectore difference Δk during the initial steps of propagation should only be a function of ΔM and thus of the spin-wave intensity. Since the intensities in our measurements were chosen to be similar for both bias magnetic fields one should expect to observe identical Δk at the beginning of the propagation ($z = 0\,\mathrm{mm}$), which is confirmed by an exponential fit of our experimental data within the precision of the measurement. However, the resulting maximal phase splitting as well as the propagation distance needed to reach the saturation value deviates significantly for the different fields (see Fig. 3). This effect cannot be interpreted by the simple model given above. Therefore additional experimental and theoretical work has to be performed to fully understand this effect.

In conclusion we obtained phase accumulation and phase splitting of nonlinear spin-wave packets using the capabilities of our phase-sensitive BLS setup. We were able to observe nonlinear phase splitting caused by a changing of the static magnetization due to the huge amplitude difference between the peak and the tail of the spin-wave pulse. These results lay the groundwork for further investigations of nonlinear spin-wave propagation phenomena with the added value of high sensitivity to phase related phenomena.

Support by the Deutsche Forschungsgemeinschaft, the Graduiertenkolleg 792 and the Australian Research Council is gratefully acknowledged.

References

[1] A.A. Serga, T. Schneider, B. Hillebrands, S.O. Demokritov, M.P. Kostylev, Appl. Phys. Lett. , **89**, 063506 (2006).
[2] R.W. Damon, J.R. Eshbach, J. Phys. Chem. Solid, **19**, 308 (1961).
[3] V.T. Synogach, Y.K. Fetisov, C. Mathieu, C.E. Patton, Phys. Rev. Lett. , **85**, 2184 (2000).

6.4 Dynamics of spin waves at the bottom of spin wave spectrum

A.A. Serga and B. Hillebrands[1]

Bose-Einstein condensation [1,2] is one of the most fascinating phenomena predicted by quantum mechanics. It involves the formation of a collective quantum state composed of identical particles with integer angular momentum (bosons), if the particle density exceeds a critical value. To achieve Bose-Einstein condensation, one can either decrease the temperature or increase the density of bosons. It has been predicted [3,4] that a quasi-equilibrium system of bosons could undergo Bose-Einstein condensation even at relatively high temperatures, if the flow rate of energy pumped into the system exceeds a critical value. Here we report the observation of Bose-Einstein condensation in a gas of magnons at room temperature. The idea of these experiments was proposed by G.A. Melkov and S.O. Demokritov. The first attempt to observe BEC using the Brillouin light scattering technique was made in Kaiserslautern, where the design of the set-up was developed. Experimental results presented here were largely obtained by V.E. Demidov and O. Dzyapko. Theoretical support came from A.N. Slavin and G.A. Melkov. The complete version of the article is published in [5].

A gas of magnons is a very attractive candidate for the BEC transition [6,7]. It can be considered as consisting of relatively weakly interacting bosons at temperatures far below T_C, the temperature of magnetic ordering. Magnons are reminiscent of Bose particles in a quantum gas of atoms −many magnons can occupy the same quantum state, and the main mechanism of magnon thermalization is four-magnon scattering, which corresponds to particle-particle collision processes. The BEC transition of magnons at low temperatures has been discussed in many publications over the past few years [8–10].

Yttrium-iron-garnet (YIG) films comprise a very suitable medium for the experimental investigation of the magnon BEC transition. First, the well-known process of parametric pumping [11,12] offers an effective way to feed energy into the low-frequency part of the magnon spectrum, which then can relax into magnons with the minimum frequency, ν_m, where BEC should take place. This frequency, which is mainly determined by the applied magnetic field, is $2-3\,\mathrm{GHz}$ for the described experiments ($h\nu_m/k_B \approx 100\,\mathrm{mK}$; here h is Planck's constant, and k_B is the Boltzmann constant). Using parametric pumping, a pumped magnon density of $10^{18}-10^{19}\,\mathrm{cm}^{-3}$ can be reached [12]. Although this density is much smaller than that of thermal magnons at room temperature, $10^{21}-10^{22}\,\mathrm{cm}^{-3}$, this increase is enough to cause the BEC transition of magnons, as shown below. Second, YIG films provide a very long spin-lattice relaxation time of above $1\,\mu\mathrm{s}$. In contrast, the magnon-magnon thermalization time due to the two- and four-magnon scattering relaxation mechanisms can be as low as $100-200\,\mathrm{ns}$. As both mechanisms keep the number of magnons constant, a quasi-equilibrium state for the magnon gas can be realized with a non-zero chemical potential.

The total magnon density, N_0, and the total energy density of the magnon system, E_0, are determined at temperature T_0 by the integrals $N_0(T_0)=\int \rho(\nu)d\nu$ and $E_0(T_0)=\int h\nu\rho(\nu)d\nu$; where $\rho(\nu)$ is the magnon spectral density, which is equal to the product of the magnon density of states, $D(\nu)$,

[1] In cooperation with S.O. Demokritov, V.E. Demidov, O. Dzyapko, Institute for Applied Physics, University of Münster, Münster, Germany;
G.A. Melkov, Department of Radiophysics, National Taras Schevchenko University of Kiev, Kiev, Ukraine;
A.N. Slavin, Department of Physics, Oakland University, Rochester, Michigan, USA.

and the statistical occupation function $n(\nu)$:

$$\rho(\nu) = D(\nu)n(\nu) = \frac{D(\nu)}{\exp\left(\frac{h\nu-\mu}{k_B T_0}\right) - 1} \quad . \tag{1}$$

Here T_0 is the temperature of the system (room temperature in our case) and μ is the chemical potential. As mentioned above, the chemical potential of a magnon gas in thermodynamic equilibrium with the lattice is zero, as the number of magnons is not conserved, mainly owing to the energy exchange between the magnons and the lattice. The injection of additional magnons by parametric pumping increases both the number of magnons, N, and their total energy, E: $N = N_0 + \delta N$, $E = E_0 + \delta E$. The values δE and δN are directly related to each other: $\delta E = h\nu_p \delta N$, where ν_p is the frequency of the pumped magnons. If magnon-magnon interactions dominate over spin-lattice relaxation, the magnon gas reaches a quasi-equilibrium state with a non-zero chemical potential. Substituting the values typical for the described experiment ($\delta N \approx 5 \cdot 10^{18}\,\mathrm{cm}^{-3}$ and $\nu_p = 4\,\mathrm{GHz}$) into the above relations yields $\mu/k_B = 100\,\mathrm{mK}$. This estimate shows that μ can be made as large as $h\nu_m$, that is, using parametric pumping it is possible to bring the magnon system close to the condition of the BEC transition.

The experimental set-up for magnon excitation in YIG films and their detection using Brillouin light scattering (BLS) [13] spectroscopy is shown schematically in Fig. 1. The studies were performed on optically transparent YIG films of $2-10\,\mu\mathrm{m}$ thickness and lateral sizes of $2 \times 20\,\mathrm{mm}^2$. A microstrip resonator attached to the YIG film creates a microwave pumping field with frequency of $2\nu_p$ in the range of $6-9\,\mathrm{GHz}$. To avoid thermal overheating of the sample via microwave radiation, pumping was performed in an intermittent pulsed mode with an on/off ratio of $1/20$ and a pulse width in the range $1-100\,\mu\mathrm{s}$. The film was placed in a uniform static magnetic field, H, up to $1\,\mathrm{kOe}$. The pumping process is illustrated in Fig. 1 inset. The low-frequency part of the spectrum of the magnons with wavevectors parallel to the static magnetization is shown by the solid

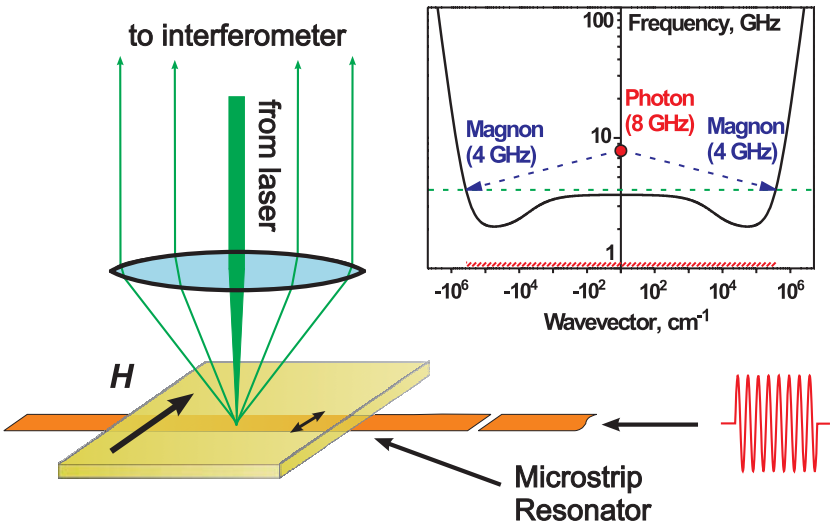

Fig. 1: The set-up for magnon excitation and detection. The resonator attached to the bottom of the yttrium-iron-garnet film is fed by microwave pulses. The laser beam is focused onto the resonator, and the scattered light is directed to the interferometer. Inset: the process of creation of two magnons by a microwave photon. The low-frequency part of the magnon spectrum for the applied field H, parallel to the film surface is shown by the solid line. It has a minimum at the wavevector $k_m = 5 \cdot 10^4\,\mathrm{cm}^{-1}$. The wavevector interval indicated by the hatching corresponds to the interval of the wavevectors accessible for Brillouin light scattering spectroscopy.

line in the log-log plot. Those magnons have the lowest frequencies among all the magnons [14], and a characteristic frequency minimum exists in their dispersion law [15, 16]. A microwave photon with a frequency of $2\nu_p$ creates two primary excited magnons of frequency ν_p and opposite wavevectors. These primary magnons relax very fast and create a quasi-equilibrium distribution of thermalized magnons, forming the magnon gas described by Eq. 1. As the chemical potential of the gas increases with pumping power, a possible BEC transition can take place near the minimum in the spectrum, as it corresponds to the state with the absolute minimum in magnon energy.

To examine the distribution of the magnons over the spectrum, BLS spectroscopy [13] was used. As shown in Fig. 1, the incident laser beam is focused onto the resonator. The beam passes through the YIG film, is reflected by the resonator, and passes through the film again. Then the light is collected by a wide-aperture objective lens and sent to the interferometer for frequency analysis of light photons inelastically scattered by the magnons. This approach allows a simultaneous detection of the magnons in a wide interval of inplane wavevectors, estimated as $\pm 2 \cdot 10^5\,\mathrm{cm}^{-1}$, which exceeds k_m, as indicated by the hatching in Fig. 1 inset. Thus, our BLS set-up is able to detect all magnons at and close to the frequency minimum, where the condensation should take place. The BLS experiments are performed with time resolution, wherein the start of the pumping pulse plays the role of the reference stroboscopic clock. The time evolution of $n(\nu)$ after the start of pumping is determined using time frames of 100 ns width.

From the general point of view, the scattering intensity at a given frequency, $I(\nu)$, is directly proportional to the reduced spectral density of scatterers (in our case magnons) [17], $I(\nu) \propto \tilde{\rho}(\nu) = \tilde{D}(\nu)n(\nu)$; where the reduced density of states $\tilde{D}(\nu)$ is calculated by integration over the wavevectors of only the particles accessible in the experiment. Thus, the occupation function of magnons, $n(\nu)$, can be obtained from the BLS experiments, provided their reduced density of states, $\tilde{D}(\nu)$, has been once determined independently.

The experiments were performed over a wide range of experimental conditions. Here we present the results corresponding to $H = 700\,\mathrm{Oe}$ and $\nu_p = 4.05\,\mathrm{GHz}$, which are typical for the range of $H = 600 - 800\,\mathrm{Oe}$ and $\nu_p = 3 - 4.5\,\mathrm{GHz}$. Figure 2 demonstrates a BLS spectrum of magnons

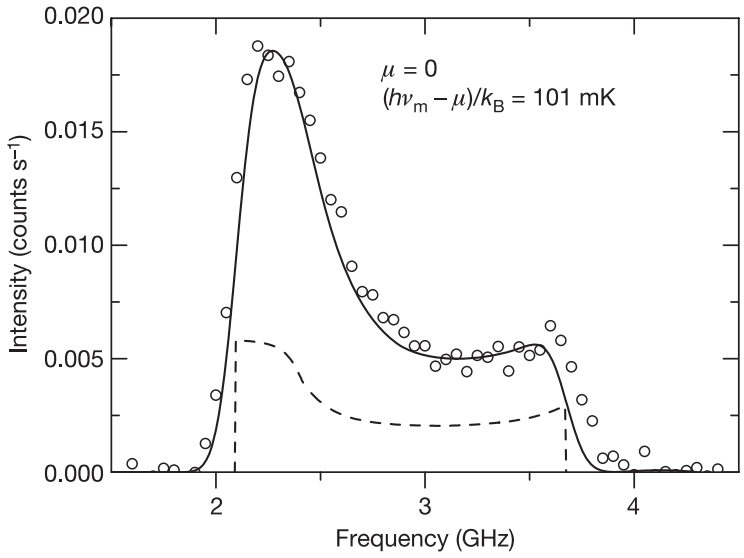

Fig. 2: BLS spectrum of thermal magnons recorded without pumping. The reduced density of states, $\tilde{D}(\nu)$; obtained from the fit of the experimental data (solid line) using Eq. 1 with the zero chemical potential, μ, is shown by the dashed line. ν_m is the minimum frequency of magnons, h is Planck's constant, and k_B is the Boltzmann constant.

without pumping; such magnons always exist in the sample owing to thermal fluctuation. The spectrum shows a minimum magnon frequency of $\nu_m = 2.1\,\mathrm{GHz}$ ($h\nu_m/k_B = 101\,\mathrm{mK}$) and a maximum cut-off frequency of 3.7 GHz, caused by the finite interval of the magnon wavevectors accessible in the experiment. This spectrum was used to independently determine the reduced density of states function, $\tilde{D}(\nu)$, as the calculated function $\tilde{D}(\nu)$ (ref. [15]) contains the value of the surface anisotropy of the YIG film, which is not known with the adequate accuracy. In fact, the BLS spectrum from thermally excited magnons corresponds to the known occupation function, $n(\nu)$, defined by Eq. 1 with $\mu = 0$. Using the value of the surface anisotropy and the proportionality factor between $I(\nu)$ and $\tilde{\rho}(\nu) = \tilde{D}(\nu)n(\nu)$ (the vertical scaling factor of the spectra) as the two fitting parameters, the measured spectrum has been fitted. The result of the fit is shown in Fig. 2 by the solid line, whereas the obtained function $\tilde{D}(\nu)$ is shown by the dashed line. We should emphasize that once determined from this fit, $\tilde{D}(\nu)$ has been used for the description of BLS from pumped magnons.

Figure 3 shows the BLS spectra of the pumped magnons recorded at different delay times, τ, as indicated, for pumping pulse duration 1 µs, and repetition period 20 µs. From the figure, it is seen that pumping continuously increases the number of magnons in the system with time (note the different vertical scales of the graphs). As four-magnon scattering is a nonlinear process, the thermalization time of the pumped magnons is inversely proportional to the magnon density.

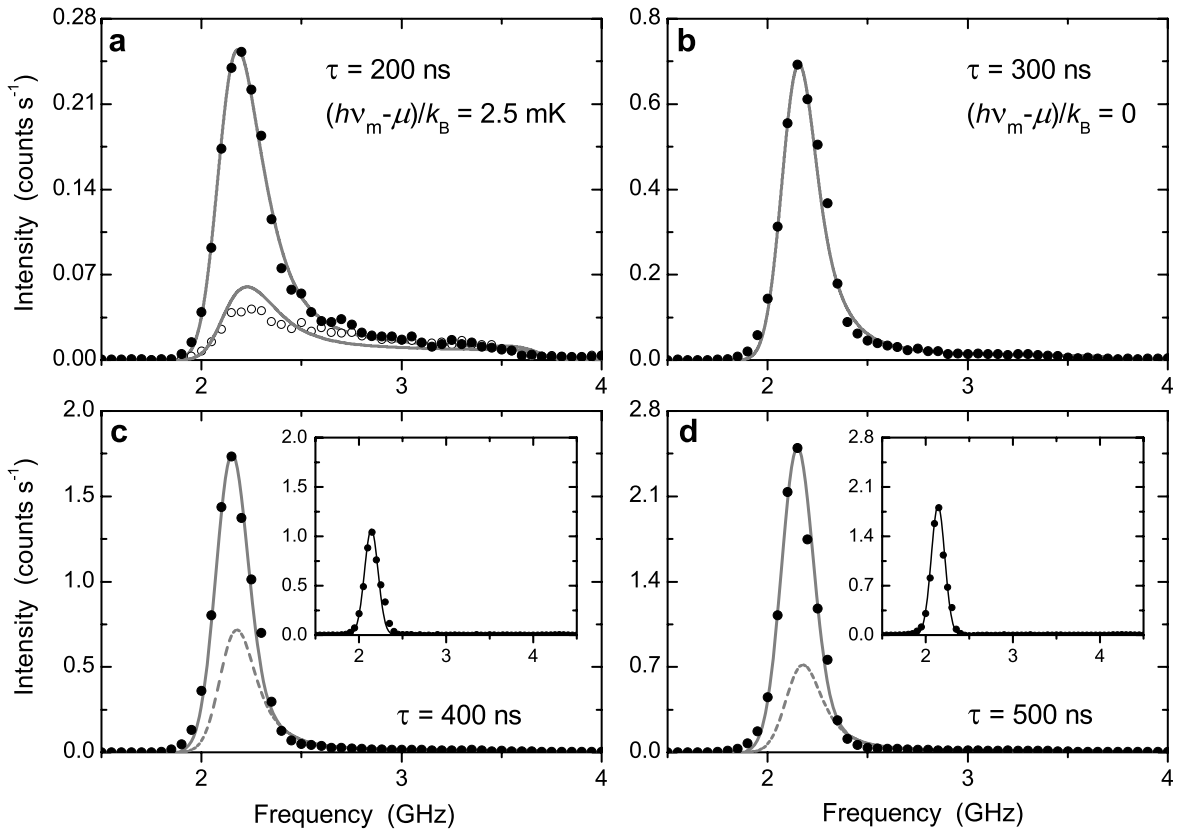

Fig. 3: BLS spectra from pumped magnons at different delay times, τ. a, $\tau = 200\,\mathrm{ns}$; b, 300 ns; c, 400 ns; and d, 500 ns. Filled circles (all panels) show data points recorded at pumping power $P = 5.9\,\mathrm{W}$, whereas open circles (panel a) represent the data recorded at $P = 4\,\mathrm{W}$. Solid lines in a and b show the results of the fit of the spectra based on Eq. 1 with the chemical potential being a fitting parameter. The fit of the spectra in c and d (solid lines) are the sums of the magnon density calculated using equation 1 (dashed line) with $\mu = h\nu_m$ and the magnon density due to the singularity at $\nu = \nu_m$. Insets in c and d illustrate the difference between the corresponding raw spectra and that at $\tau = 300\,\mathrm{ns}$; axes as main panels.

Figure 3a shows the data corresponding to $\tau = 200\,\text{ns}$ and two different pumping powers, $P = 4.0\,\text{W}$ (open circles) and 5.9 W (filled circles). The solid lines show the results of the fits based on Eq. 1 with the chemical potential being the fitting parameter. As seen in Fig. 3a, the data for $P = 4.0\,\text{W}$ cannot be described using the Bose-Einstein statistics, illustrating that the thermalization process at those magnon densities lasts more than 200 ns. By contrast, the data for the pumping power $P = 5.9\,\text{W}$ are described very well by the Bose-Einstein statistics at room temperature and a non-zero chemical potential μ, $\mu/k_\text{B} = 98 \pm 1\,\text{mK}$. Thus, for this pumping power the magnon-magnon interaction is fast enough to provide an efficient means for magnon thermalization for delay times above 100 ns. All the results discussed below correspond to this pumping power. From comparison of Fig. 2 and different panels of Fig. 3 with each other, we conclude that the magnon occupation is shifted towards lower frequencies as the number of the pumped magnons increases with time. The spectrum shown in Fig. 3b also follows the Bose-Einstein distribution, Eq. 1 with a non-zero μ, $\mu/k_\text{B} = 101 \pm 0.5\,\text{mK}$ (that is, $\mu \approx h\nu_\text{m}$), as shown by the solid line. An important intermediate conclusion is that the chemical potential increases with time, reflecting the growth of the magnon density caused by the pumping. For the above experimental conditions, it approaches $h\nu_\text{m}$ at $\tau = 300\,\text{ns}$.

The spectra presented in Fig. 3c and d differ significantly from those shown in Fig. 3a and b. They cannot be fitted using the above procedure based on Eq. 1. In fact, we obtain the highest possible magnon density at a critical value $\mu = h\nu_\text{m}$. The calculated curves are shown in Fig. 3c and d by the dashed lines. As shown in the insets, the magnon spectral densities at $\tau = 400\,\text{ns}$ and 500 ns deviate from those at $\tau = 300\,\text{ns}$ just in the vicinity of ν_m, whereas far from ν_m the difference is within the experimental error. The finite width of the profiles in the insets is due to the finite frequency resolution of the interferometer, $\Delta\nu = 250\,\text{MHz}$. To reach agreement with the experiment, we had to add a singularity peak $\propto \delta(\nu - \nu_\text{m})$ to the occupation function, $n(\nu)$. The corresponding fits are shown by the solid lines. The agreement between the experimental data and the results of the calculation is convincing. Thus, to describe the experimental data we need to postulate the existence of a Bose-Einstein condensate.

For the above experimental conditions, the growth of the magnon density saturates after $\tau = 500\,\text{ns}$. This is connected with the fact that stationary flow balance is achieved between the excitation of the primary magnons by the pumping, their relaxation into other magnons, condensation of those magnons in the condensate and the final energy relaxation to the lattice. After that, the magnon gas stays in the quasi-equilibrium state for the rest of the pumping pulse duration, which can be as long as 100 µs.

The observed condensation of pumped magnons demonstrates intrinsic features of BEC. However, the observed condensate differs in some aspects from those seen in other systems: first, it is found in quasi-equilibrium, which means that the maximum condensate density is governed by the pumping power; and second, it is observed when the lattice is at room temperature. In this way, our findings contribute both to the quantum thermodynamics and to the thermodynamics of non-equilibrium systems in general. They open a new route for the investigation of thermodynamics in systems of quasi-particles by showing that a non-zero chemical potential can be changed independently of the system temperature.

Support by the Deutsche Forschungsgemeinschaft is gratefully acknowledged.

References

[1] S.N. Bose, *Plancks Gesetz und Lichtquantenhypothese*, Z. Phys. **26** (1924).

[2] A. Einstein, *Quantentheorie des einatomigen idealen Gases. Teil I*, Sber. Preuss. Akad. Wiss. **22**, 261 (1924); *Quantentheorie des einatomigen idealen Gases. Teil II*, Sber. Preuss. Akad. Wiss. **1**, 3(1925).

[3] H. Fröhlich, *Bose condensation of strongly excited longitudinal electric modes*, Phys. Lett. A **26**, 402 (1968).

[4] M.V. Mesquita, A.R. Vasconcellos, R. Luzzi, *Positive-feedback-enhanced Fröhlich's Bose-Einstein-like condensation in biosystems*, Int. J. Quant. Chem. **66**, 177 (1998).

[5] S.O. Demokritov, V.E. Demidov, O. Dzyapko, G.A. Melkov, A.A. Serga, B. Hillebrands, and A.N. Slavin, *Bose-Einstein condensation of quasi-equilibrium magnons at room temperature under pumping*, Nature **443**, 430 (2006).

[6] Y.D. Kalafati, V.L. Safonov, *Thermodynamic approach to the theory of paramagnetic resonance of magnons*, Zh. Eksp. Teor. Phys. **95**, 2009 (1989); [in English] Sov. Phys. JETP **68**, 1162 (1989).

[7] M.I. Kaganov, N.B. Pustylnik, T.I. Shalaeva, *Magnons, magnetic polaritons, magnetostatic waves*, Phys. Usp. **40**, 181 (1997).

[8] T. Nikuni, M. Oshikawa, A. Oosawa, H. Tanaka, *Bose-Einstein condensation of dilute magnons in* $TlCuCl_3$, Phys. Rev. Lett. **84**, 5868 (2000).

[9] C. Rüegg, et al., *Bose-Einstein condensation of the triplet states in the magnetic insulator* $TlCuCl_3$. Nature **423**, 62 (2003.

[10] E. Della Torre, L.H. Bennett, R.E. Watson, *Extension of the Bloch* $T^{3/2}$ *law to magnetic nanostructures: Bose-Einstein condensation*, Phys. Rev. Lett. **94**, 147210 (2005).

[11] V.S. L'vov, *Wave Turbulence Under Parametric Excitation*, Springer, Berlin, (1994).

[12] A.G. Gurevich, G.A. Melkov, *Magnetization Oscillations and Waves*, CRC, New York, (1996).

[13] S.O. Demokritov, B. Hillebrands, A.N. Slavin, *Brillouin light scattering studies of confined spin waves: linear and nonlinear confinement*, Phys. Rep. **348**, 441 (2001).

[14] R.W. Damon, J.R. Eshbach, *Magnetostatic modes of a ferromagnet slab*, J. Phys. Chem. Solids **19**, 308 (1961).

[15] M. Sparks, *Ferromagnetic resonance in thin films. I. Theory of normal-mode frequencies*, Phys. Rev. B **1**, 3831 (1970).

[16] T. Wolfram, R.E. De Wames, *Magnetoexchange branches and spin-wave resonance in conducting and insulating films: perpendicular resonance*. Phys. Rev. B **4**, 3125 (1971).

[17] M. Cottam, D. Lockwood, *Light Scattering in Magnetic Solids*, Wiley, New York, (1986).

6.5 Kerr imaging of microwave assisted switching

P. Martín Pimentel, B. Leven, and B. Hillebrands[1]

Microwave assisted switching in $Ni_{81}Fe_{19}$ ellipsoids has recently been presented [1]. It has been suggested as an improvement of the actual concept for data storage processing. In this approach we applied a microwave field in the plane of the ferromagnetic ellipsoid shaped thin film element perpendicular to the easy axis in order to reduce the coercivity [1]. A clear reduction of the coercivity under the influence of the microwave field could be observed. In order to gain a deeper understanding of the observed effect, Kerr microscopy imaging has been performed. The understanding of the domain structure occurring during the magnetization reversal process under the influence of a microwave field is of crucial importance. When using a microwave assisted switching approach the microwave field is expected to reduce the switching field of a soft ferromagnetic element, even if the switching process is dominated by domain nucleation and growth [2]. The applied microwave field induces large angle oscillations of the magnetization of the element if the resonance condition is fulfilled. This reduces the effective energy barrier for domain nucleation, which cannot be overcome by thermal fluctuations alone [3–6].

We report on the distribution of magnetic domains during the magnetization reversal process in a $Ni_{81}Fe_{19}$ ellipsoid under the influence of a microwave field. We employ a non-scanning Kerr microscope Axiomat Zeiss West with a space resolution of 0.5 µm in longitudinal geometry, located at Sensitec Naomi, Mainz. The light source is a Mercury lamp BO75W HBO 100W. The images are made with a Hamamatsu dual mode cooled CCD camera C4880 integrated in the microscope. The sample is placed on top of a 300 µm wide microwave antenna. The long axis of the ellipsoid is aligned parallel to the quasi-static magnetic field, which is generated by an external ring coil. The microwave field is oriented transversally, i.e., perpendicular to the quasi-static field in the plane of the element. Fig. 1 shows a schematic drawing of the sample stage and the orientation of the applied fields.

To generate the microwave field an IFR 2032 signal generator with a frequency range of 10 kHz to 5.4 GHz in combination with an Aldetec microwave amplifier APL-0520P433 is used. We studied a 10 nm thick $Ni_{81}Fe_{19}$ ellipsoid with a long axis of 160 µm and a short axis of 80 µm. The ellipsoid was produced by a combination of UV-photo lithography and molecular beam epitaxy on a 100 µm thick glass substrate. The $Ni_{81}Fe_{19}$ layer is capped by a 2 nm thick Al protection layer. To induce an uniaxial anisotropy with the easy axis oriented along the long axis of the ellipsoid a magnetic field was applied during growth. The basic magnetic properties of the sample were characterized by time-domain ferromagnetic resonance experiments [1].

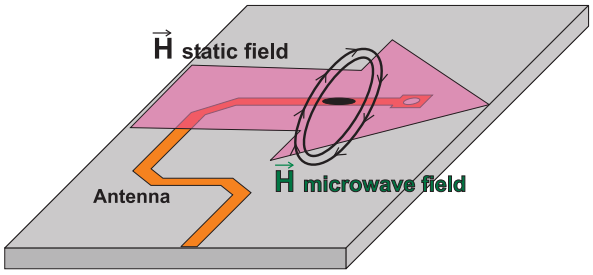

Fig. 1: Scheme of the sample (black ellipsoid) placed on top of microwave antenna. The long axis of the ellipsoid is aligned parallel to the quasi-static magnetic field (big arrow) which is generated by an external ring coil. The microwave field is oriented transversally, i.e., perpendicular to the quasi-static field in the plane of the element (circular field lines).

[1] In collaboration with H. Grimm, Sensitec Naomi, Mainz, Germany.

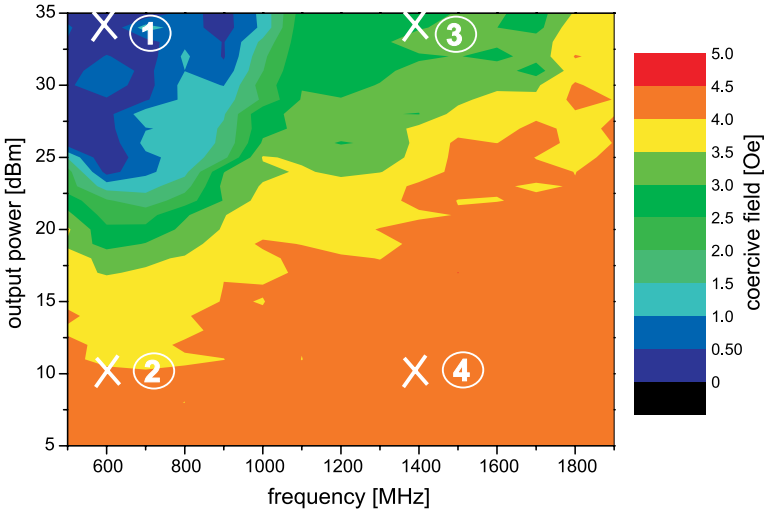

Fig. 2: The coercive field values are shown for frequencies (x-axis) in the range between 500 MHz and 2000 MHz with a output power range (y-axis) of 3.2 mW to 3.2 W. The crosses mark the values shown in the Kerr imaging studies. The mark number 1 is the value corresponding to 600 MHz, low output power 3.2 mW, number 2 corresponds to 600 MHz at high output power 3.2 W, number 3 is for a frequency of 1400 MHz and low output power 3.2 mW, and number 4, 1400 MHz at high output power 3.2 W (after [1]).

The switching behavior of the $Ni_{81}Fe_{19}$ ellipsoid was studied by Kerr microscopy. The microwave field was applied perpendicular to the quasi-static magnetic field (range between 0 Oe and −12 Oe). The sample was saturated before each measurement with a magnetic field of 60 Oe. We report only on one of the hysteresis branches due to fact that the behavior is symmetric. The frequency of the microwave field was varied in the range from 500 MHz to 1.5 GHz in steps of 100 MHz and the microwave power was increased from 0 mW to 3.2 W for each frequency, in steps of 3.2 mW.

The results of the microwave assisted switching experiments are summarized in the map shown in Fig. 2 [1]. The coercive field is plotted using a grey-color code as a function of the frequency (x-axis) and the power (y-axis) of the applied microwave field. As we can see in Fig. 2 the coercivity is strongly reduced for microwave frequencies between 500 MHz and 900 MHz, up to certain values of the output power. We marked on the map four different parameter points, see Fig. 2: Mark 1 and 2 correspond to the frequency of 600 MHz, whereas Mark 3 and 4 correspond to the frequency of 1400 MHz, for high and low power, respectively.

Reading from left to right in Fig. 2, the data Mark 1 show the maximum reduction of the coercive field. Mark 3 shows a smaller reduction, and in Mark 2 and 4 no modification of the coercivity occurs. Kerr images of the four corresponding parameters sets are shown in Fig. 3 and 4. A sequential substraction imaging process has been used, to easily identify any possible change in the magnetic contrast, each image is compared with the next and the differences are shown in a new picture. The first image of the sequence of images is always compared with the saturation state.

In Figure 3a, Kerr images corresponding to Mark 1 on the coercivity map of Fig. 2 are presented. The first image shows no magnetic contrast, there is no difference between the surrounding area and the ellipsoid. The second image shows a nearly full reversed magnetization state, i.e., the switching process occurred between −1 Oe and −2 Oe. In image three there is still a remaining domain approximately in the middle of the ellipsoid corresponding to the field range between −2 Oe and −3 Oe. Note that we show only the sequences of the switching process and omitted some of the beginning and ending images because they contain no relevant information. In Fig. 3b, which corresponds to Mark 2 on the coercivity map, the process of magnetization reversal starts at −3 Oe and ends at −9 Oe and is characterized by the formation of a multi-domain configuration. When comparing Fig. 3a and Fig. 3b it is obvious that the reversal processes, differ drastically.

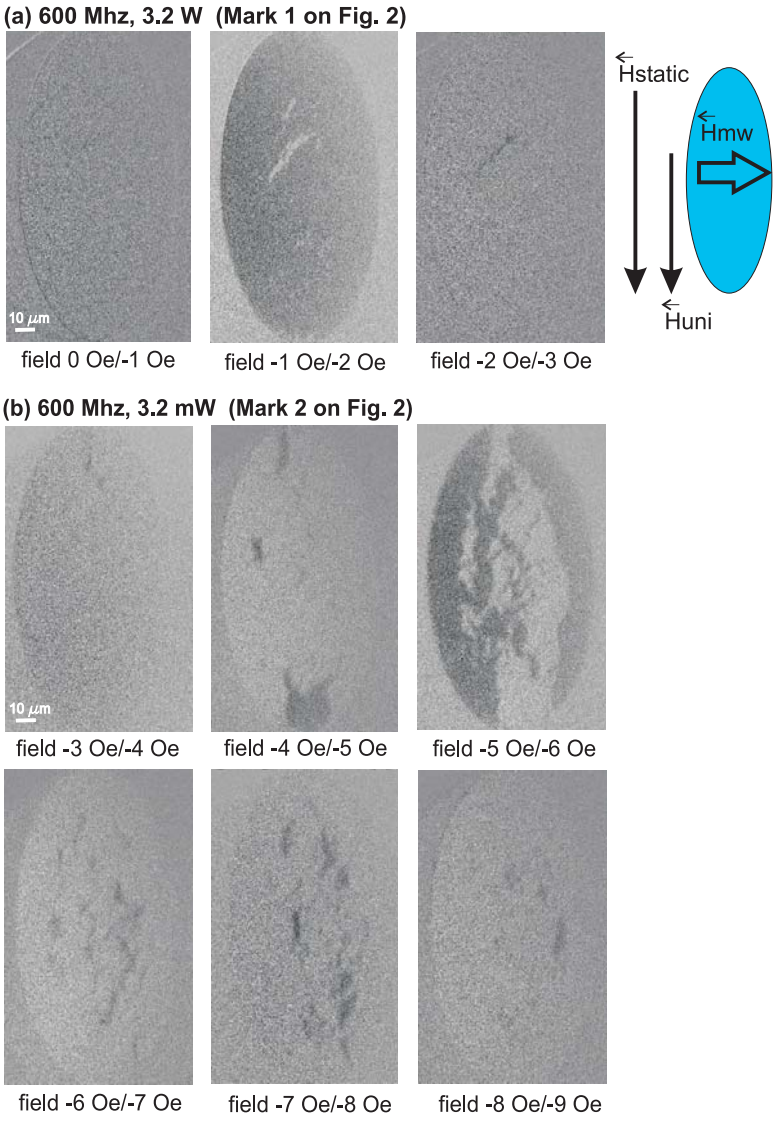

Fig. 3: (a) Shows the Kerr images correspond to the frequency of 600 MHz, for high power 3.2 W (Mark 1 in the map of Fig. 2) and (b) for low power 3.2 mW (Mark 2), respectively. The schematic draw in the right side of the first line of images, shows the distribution of the field during the experiment. H static is the magnetic field generated by the coils, H uni is the uniaxial anisotropy induced during the deposition process, and the H mw is the microwave magnetic field generated in the antenna which is perpendicular to the static magnetic field and to the H uni. The labels under each pictures show the two magnetic fields values corresponding to the Kerr imaging substraction process.

In Figure 4a, referring to Mark 3 in the coercive field map see Fig. 2, the first image shows no contrast variation between the surrounding area and the ellipsoid. There is no change in the magnetization configuration. The second image shows that the magnetization reversal process is finalized; The frequency of 1400 MHz at high output power of the microwave field the switching process occurs between -3 Oe and -4 Oe. In Fig. 4b, Mark 4 in the coercivity map, the output power is lower than in Fig. 4a and the magnetization reversal process takes place between -3 Oe and -10 Oe. Note that at low and high microwave power values a similar magnetization reversal behavior has been observed for both frequencies.

This behavior can be attributed to two dominating mechanisms. The first one is the enhancement of domain nucleation by a microwave field. To generate a reversed domain an energy barrier has to be overcome. The microwave induced precession of the magnetization lower the effective height of the barrier at smaller reversed fields, that is it supports the magnetization reversal process. The second mechanism is an enhanced growth of the reversed domain. The more microwave power is absorbed the higher the entropy becomes and the lower the Gibbs free energy is. It supports the fundamental principle that every physical system favors the state with the lowest Gibbs free energy.

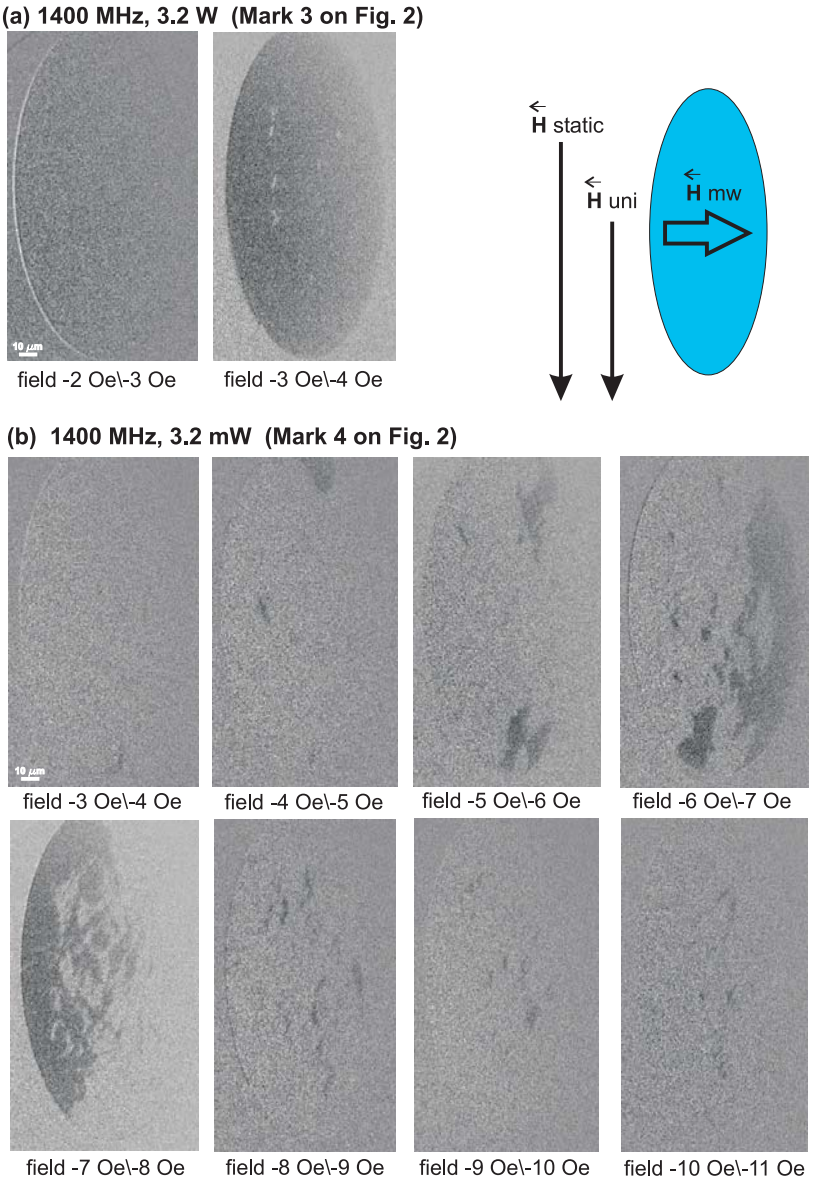

Fig. 4: (a) Shows the Kerr images correspond to the frequency of 1400 MHz, for high power 3.2 W (Mark 3 in the map of Fig. 2)and (b) for low power 3.2 mW (Mark 4 in Fig. 2), respectively.

So far, we qualitatively discussed the magnetization reversal process involved in the different behaviors exhibited in the Kerr images for low and high power of the microwave field. The following values obtained from the Kerr images are quantified and compared to the results presented in [1] (see also Fig. 2). The switching field values have been extracted from the Kerr images (see Figs. 3 and 4) and plotted versus the normalized magnetization M/Ms in Fig. 5. Fig. 5a shows the loops corresponding to Mark 1 and Mark 3, 600 MHz at 3.2 W and 1400 MHz at 3.2 W, respectively. The coercive field is smaller for Mark 1 than for Mark 3, with a relative difference of 2 Oe. This is also the same relative value extracted from Fig. 2 between the same two Marks. We have to take into account that both experimental results have been obtained using different setups with different techniques. Therefore, we restrict the comparison to the relative values. Fig. 5b shows the values extracted from the Kerr images of Marks 2 and 4 of the map in Fig. 2. We can see that there is no modification in the coercive field as expected from the extracted result of Fig. 2. It is also necessary to take into account the fact that in the experiment of Nembach et al [1] the spot size of the laser was 30 µm pointed to the center of the ellipsoid, whereas at the Kerr microscopy experiment we have the full element under study.

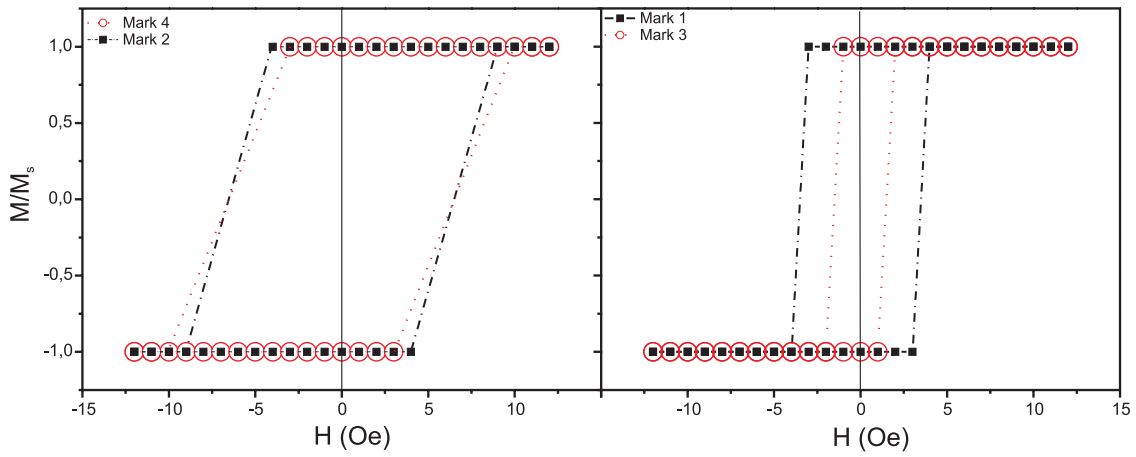

Fig. 5: (a) Shows the magnetization versus the magnetic field, extracted from the Kerr images, at 3.2 W for 600 MHz and 1400 MHz, respectively. (b) Shows the magnetization versus the magnetic field, extracted from the Kerr images, at 3.2 mW for 600 MHz and 1400 MHz, respectively.

We conclude that the strong reduction of the coercive field in the region from 500 MHz to 900 MHz is due to fact that domains are favorably nucleated in areas with reduced internal field. The mechanisms dominating the magnetization reversal process can be modified drastically by applying a transversal microwave field corroborating the results described in [1].

The authors thank the Nano+Bio Center of the University of Technology of Kaiserslautern for technical support, Andreas Beck for sample deposition, and H.T. Nembach for thorough discussions. Financial support by the European Commission within the EU-RTN ULTRASWITCH (HPRN-CT-2002-00318) is gratefully acknowledged. Furthermore, the work and results reported in this publication were obtained with research funding from the European Community under the Sixth Framework Programme Contract Number 510993: MAGLOG.

References

[1] H.T. Nembach, P. Martín Pimentel, S.J. Hermsdoerfer, B. Leven, B. Hillebrands, submitted to APL , (2006).
[2] A. Krasyuk, F. Wegellin, S.A. Nepijko, H.J. Elmers, G. Schoenhense, M. Bolte, C.M. Schneider, Phys. Rev. Lett. **95**, 207201 (2005).
[3] V.C. Chang, C.C. Chang, W.Z. Hsieh, H.M. Lee, J.C. Wu, IEEE Transations on magnetics **41**, 959 (2005).
[4] W. Scholz, D. Suess, T. Schrefl, J. Fidler, J. Appl. Phys. **91**, 10 (2002).
[5] A. Hubert, R. Schäfer: Magnetic domains, The analysis of magnetic structures, Springer (2000).
[6] W.K. Hiebert, L. Lagae, J. De Boeck, Phys. Rev. B, **68**, 020402(R) (2003).

B. Magnetic Films and Surfaces

6.6 Magnetization reversal and magnetic anisotropies in the $Co_2Cr_{0.6}Fe_{0.4}Al$ Heusler compound

J. Hamrle, S. Blomeier, O. Gaier, and B. Hillebrands[1]

Among the numerous Heusler systems already studied, the compound $Co_2Cr_{0.6}Fe_{0.4}Al$ (CCFA) attracted large attention [2–5]. CCFA is an interesting candidate due to its high Curie temperature of 760 K [3] and its high value of volume magnetization of $\approx 3\,\mu_B$ per formula unit at 5 K [5] (the theoretical value is $3.8\,\mu_B$ per formula unit [2]). At room temperature, CCFA exhibits a magnetoresistance of 88% if artificial Al_2O_3 grain boundaries [4] are used, whereas a tunnelling magnetoresistance ratio of 52% at RT was reported for the system CCFA/AlO_x/$Co_{75}Fe_{25}$ [5]. We report on magnetic anisotropies and magnetization reversal of epitaxial CCFA films deposited on Fe and Cr buffer layers [1].

We investigated two samples consisting of CCFA sputtered onto an epitaxial Fe or Cr buffer layer: Al(2.5 nm)/CCFA(80 nm)/Cr(8 nm)/MgO(001) (in the following called CCFA/Cr) and Al(4 nm)/CCFA(105 nm)/Fe(10 nm)/MgO(001) (in the following called CCFA/Fe). The buffer layers were deposited by electron beam evaporation onto a single-crystalline MgO(001) substrate, while the epitaxial CCFA films were subsequently deposited by dc magnetron sputtering [6]. The films grow in the B2 structure, as there is full disorder between the Cr-Fe and Al positions, but order on the Co positions [6]. The 4-circle X-ray diffraction scans showed that the in-plane strain is as small as $\approx 0.8 \pm 2.6\%$.

Magnetic anisotropies were investigated using magneto-optical Kerr effect (MOKE) magnetometry in longitudinal geometry performed with an angle of incidence near 45°. The MOKE hysteresis loops were measured as a function of the sample orientation α being the angle between the applied magnetic field and the in-plane [100] direction of the CCFA film (i.e., [110] direction of the MgO substrate). Typical loops as well as the corresponding polar plots of the obtained coercivity for CCFA/Cr and CCFA/Fe are presented in Fig. 1. Both the CCFA/Cr and CCFA/Fe samples show

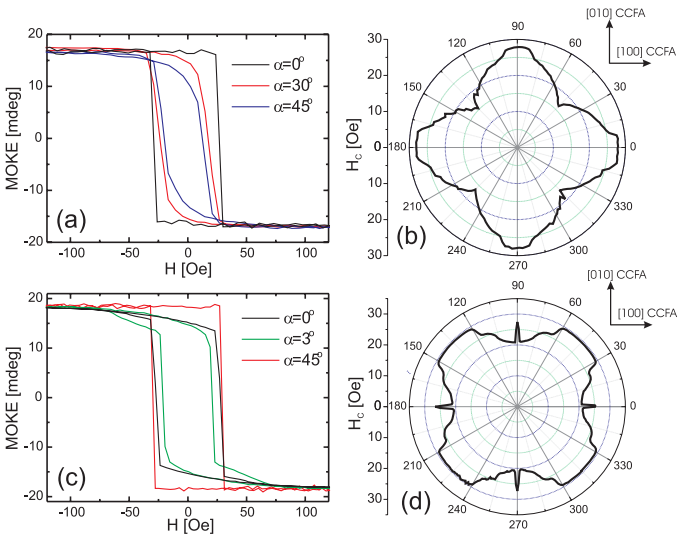

Fig. 1: (a,c) MOKE loops for different sample orientations as well as (b,d) polar plot of the coercivity H_C for CCFA/Fe and CCFA/Cr structures, respectively.

[1] In collaboration with M. Jourdan, Johannes-Gutenberg-Universität Mainz, Germany, and R. Schäfer, Leibniz-Institut für Festkörper- und Werkstoffforschung (IFW) Dresden, Germany.

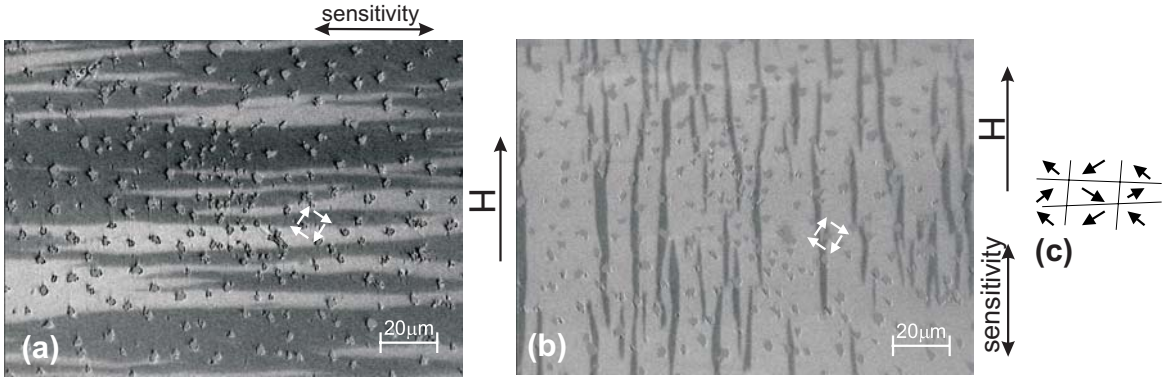

Fig. 2: Kerr microscopy images of the demagnetized state of CCFA/Cr. A demagnetizing AC field was applied in hard axis direction ($\alpha = 0°$). The images correspond to sensitivity to magnetization components (a) transverse and (b) parallel to H, respectively. Both images show an identical domain pattern, recorded under different sensitivity conditions. The magnetization directions are indicated by small white arrows. (c) Sketch of the underlying 90° domain structure.

a fourfold in-plane anisotropy reflecting the crystallographic symmetry of the CCFA film. Several interesting features can be observed: (i) The maximum coercivities for CCFA/Fe and CCFA/Cr are 28 and 29 Oe, respectively, and are thus very similar. (ii) The in-plane easy axes lie along the $\langle 100 \rangle$ CCFA axes for CCFA/Fe whereas in case of CCFA/Cr they are rotated by 45°, i.e. oriented along the $\langle 110 \rangle$ CCFA axes. At the moment, the reasons for this behavior are not clear. According to previous studies, both types of films grow with the same crystallographic orientation and thus should exhibit the same orientation of their magnetic easy axes. (iii) CCFA/Cr exhibits unique sharp peaks in H_C as a function of the in-plane angle α as narrow as 2°. These peaks are aligned parallel to the $\langle 100 \rangle$ CCFA hard axes. The origin of these peaks is discussed in following.

Magnetization reversal mechanisms were studied using a Kerr microscopy setup in Dresden described in Ref. [7]. By using different orientations of a nearly crossed polarizer and analyzer we are sensitive to magnetization components both parallel and transverse to the externally applied field H. The demagnetized state of CCFA/Cr is displayed in Fig. 2. The images shown in panels (a) and (b) are Kerr images of an identical domain structure, but with sensitivity to the magnetization components transverse and parallel to H, respectively. Both Kerr images (a) and (b) show a stripe domain pattern, with the stripe directions being parallel to the respective direction of the measured magnetization components. Therefore the demagnetized state exhibits a 90° domain structure, as it is sketched in panel (c). The dots in the Kerr images are small particles on the sample surface, which do not influence domain propagation or nucleation. The demagnetized state of CCFA/Fe is very similar to that of CCFA/Cr (it also exhibits a 90° domain structure), so we do not discuss it here any further.

We now address the origin of the peaks in the coercivity of CCFA/Cr. Figure 3a shows a Kerr image of CCFA/Cr at an angle of $\alpha \approx 3°$ (i.e., in an 'out-of-peak'orientation), after the sample had been saturated in a negative field and a field of 21 Oe had subsequently been applied. For the in-plane transverse magnetization component we did not get any contrast, i.e., this magnetization component is homogeneous. Hence, the magnetization reversal is solely characterized by the appearance of a stripe domain structure, as it is sketched in Fig. 3a. The magnetization within different domains points in different easy axis directions in such a way that the stripe domains are separated by 90° domain walls.

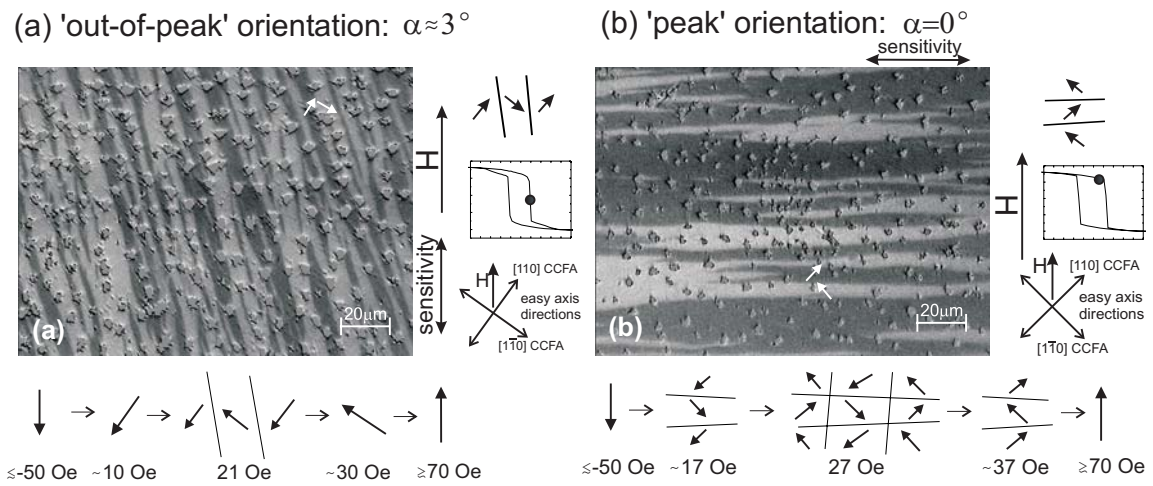

Fig. 3: Kerr microscopy image of CCFA/Cr (a) at $H = 21\,\mathrm{Oe}$ for $\alpha \approx 3^\circ$ ('out-of-peak' orientation) and (b) at $H = 18\,\mathrm{Oe}$ for $\alpha = 0^\circ$ ('peak' orientation). Magnetization directions are indicated by small white arrows. The image contrast is sketched in images. The bottom part of the image sketches the development of the magnetization reversal.

Figure 3b shows the reversal mechanism of CCFA/Cr when H is applied along the $\langle 100 \rangle$ CCFA hard axes direction ($\alpha = 0^\circ$). The sample had been saturated in a negative field and then the image was taken at a field value of 18 Oe before the jump in the hysteresis loop appears. At this field value no contrast was found for the magnetization component parallel to H. Therefore, the domain configuration consist of stripes, which are again separated by 90° domain walls, but now the stripe direction is *transverse* to H. The observed striped domain structure originates from a magnetic frustration effect, that is upon reduction of the external field the magnetization rotates into the direction of an easy axis, but has to choose between two of these axes which are energetically equivalent. Therefore the magnetization splits into domains corresponding to these axes, as sketched in Fig. 3b. If the external field is now further reduced, a jump in the respective hysteresis loop occurs, which is caused by the appearance of a 90° domain structure. Again a striped domain configuration with a stripe direction transverse to H is observed. The reversal mechanisms in both the 'peak'($\alpha = 0^\circ$) and the 'out-of-peak'orientation ($\alpha \approx 3^\circ$) are schematically illustrated in the bottom part of Fig. 3.

During the hard axis magnetization reversal of CCFA/Fe, no stripe domains transverse to the applied field H, but stripe domains oriented parallel to H, were observed. Therefore, this magnetization reversal process is similar to the 'out-of-peak'reversal of CCFA/Cr.

In conclusion, $Co_2Cr_{0.6}Fe_{0.4}Al$ (CCFA) films deposited onto Fe and Cr buffer layers exhibit a fourfold magnetic anisotropy as well as a 90° domain structure with 90° domain walls in their demagnetized state for both buffers. CCFA/Cr exhibits sharp peaks in H_C for H applied in hard axes directions. These peaks are related to the appearance of peculiar domain structures during the reversal originating from a magnetic frustration effect. In the case of CCFA/Fe, such effects have not been observed.

The project was financially supported by the Research Unit 559 *"New materials with high spin polarization"* funded by the Deutsche Forschungsgemeinschaft, and by the Stiftung Rheinland-Pfalz für Innovation. Financial support by the European Commission within the EU-RTN ULTRASWITCH (HPRN-CT-2002-00318) is gratefully acknowledged.

References

[1] J. Hamrle, S. Blomeier, O. Gaier, B. Hillebrands, R. Schafer, and M. Jourdan, in press, J. Appl. Phys. (2006), cond-mat/0606542 .
[2] I. Galanakis, J. Phys. Condens. Matter **14**, 6329 (2002).
[3] C. Felser, B. Heitkamp, F. Kronast, D. Schmitz, S. Cramm, H. A. Dürr, H. Elmers, G. H. Fecher, S. Wurmehl, T. Block, D. Valdaitsev, S. A. Nepijko, A. Gloskovskii, G. Jakob, G. Schönhense, and W. Eberhardt, J. Phys. Condens. Matter **15**, 7019 (2003).
[4] T. Block, S. Wurmehl, C. Felser, and J. Windeln, Appl. Phys. Lett. **88**, 202504 (2006).
[5] K. Inomata, S. Okamura, A. Miyazaki, M. Kikuchi, N. Tezuka, M. Wojcik, and E. Jedryka, J. Phys. D: Appl. Phys. **39**, 816 (2006).
[6] A. Conca, M. Jourdan, C. Herbort, and H. Adrian, cond-mat/0605698 (2006).
[7] A. Hubert and R. Schäfer, *Magnetic Domains: The Analysis of Magnetic Microstructures* (Springer-Verlag, Berlin, 1998).

6.7 Influence of the B2-$L2_1$ phase transition on the magnetic properties of Co_2MnSi-films

O. Gaier, J. Hamrle, S. Hermsdörfer, and B. Hillebrands[1]

We report on the magnetic properties of thin films consisting of the Heusler compound Co_2MnSi (CMS). The half-metallicity of this material crucially depends on the crystallographic order [1]. We have investigated the influence of disorder between Mn and Si sites on exchange interaction and coercivity of CMS films with crystal structures varying from the B2 to the $L2_1$ phase. Here, B2 denotes the crystal structure with disordered Mn and Si atomic sites whereas $L2_1$ is perfectly ordered. The investigated CMS films of 30 nm thickness were epitaxially grown in the group of Prof. Ando in Sendai, Japan by means of inductively coupled plasma-assisted magnetron sputtering. The x-ray diffraction measurements also performed in the group of Prof. Ando showed that the B2 crystal structure is predominant in the film annealed at $T_a = 350\,^\circ$C. The post-growth annealing at $T_a = 450\,^\circ$C provided a CMS film with an ordering degree of 100 % for the $L2_1$ phase.

To study the influence of the B2 to $L2_1$ phase transition on the spin wave frequencies of the CMS films we used the Brillouin light scattering (BLS) technique. All BLS spectra were measured at a transferred wave vector of $q_{\parallel} = 1.73 \cdot 10^5\,\mathrm{cm}^{-1}$ using laser light of $\lambda = 514.5\,$nm. The magnetization vector was oriented parallel to an in-plane easy axis direction of the CMS films and perpendicular to the wave vector of the incident light ($\mathbf{M} \perp \mathbf{k}$).

In the recorded BLS spectra, peaks originating from both magnonic and phononic scattering processes are visible. However, frequencies of phonons, unlike those of magnons, do not depend on the applied magnetic field H. Consequently, peaks originating from magnonic scattering processes can be easily identified by performing BLS measurements at various field values while all the other parameters remain fixed. Figure 1a shows spectra recorded from different samples at an applied field of 1500 Oe. There are two peaks in both the Stokes and the anti-Stokes regime originating from magnonic scattering processes. In particular, the peak at $\approx 20\,$GHz can be attributed to the Damon-Eshbach (DE) mode, while the peak appearing in the range of 30 GHz results from the excitation of the first perpendicular standing spin wave (PSSW).

Figure 1a makes evident that a phase transition from B2 to $L2_1$ does not lead to the emergence of new peaks in the BLS spectra. It is also notable that neither the existing magnon nor phonon peaks change their spectral position when the crystal structure is modified. The frequencies of DE and PSSW modes remain constant within an experimental error of 1 % as is shown in Fig. 1b. It is well known that the frequencies of the PSSWs are related to the exchange stiffness constant A and the saturation magnetization M_s [2]. Therefore, it can be concluded that A and M_s do not change their value upon the transition from the B2 to the $L2_1$ crystal structure in CMS films.

Furthermore, we investigated the influence of the B2 to $L2_1$ phase transition in CMS films on their coercivity. For this purpose, a standard magneto-optical Kerr effect (MOKE) set-up in the longitudinal geometry was used. For a description of the method and data analysis see [3] as well as section 6.8 in this report.

The hysteresis loops of all investigated CMS films acquired from MOKE measurements reveal a strongly asymmetric shape depending on the sample orientation with respect to the direction of the

[1] In collaboration with Y. Ando, Tohoku University, Sendai, Japan.

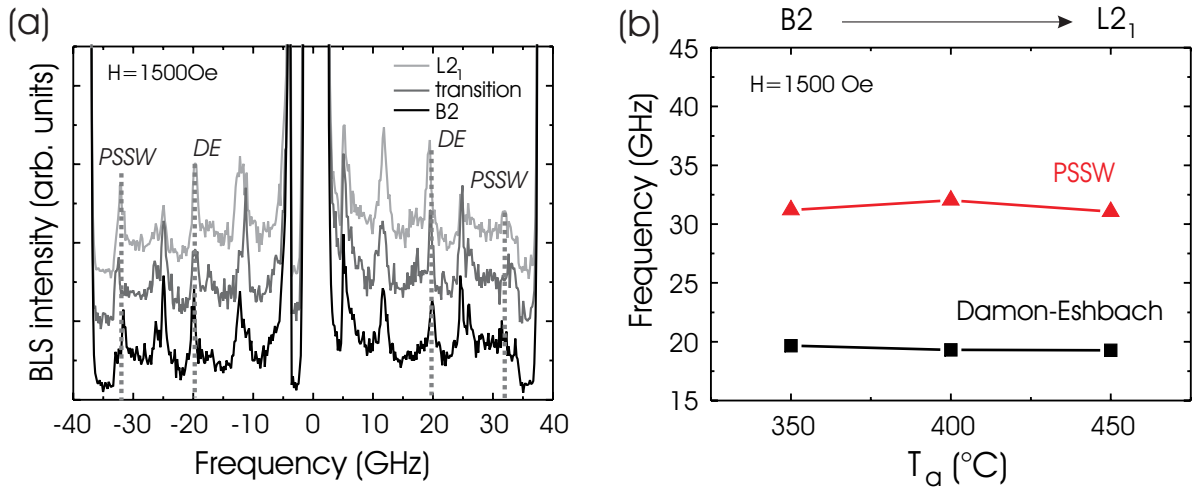

Fig. 1: (a) BLS spectra of CMS films with various crystal structures measured at an applied magnetic field of $H = 1500\,\mathrm{Oe}$ and a transferred wave vector of $q_{\parallel} = 1.73 \cdot 10^5\,\mathrm{cm}^{-1}$. (b) Dependence of spin wave frequencies on the crystal structure of the CMS films. T_a is the annealing temperature.

applied magnetic field. For example, Fig. 2 shows the hysteresis curve of the CMS film with the B2 crystal structure at a sample orientation of $\alpha = 44^\circ$ with α being the angle between the in-plane [110]-direction of the CMS film and the direction of the external magnetic field. The observed asymmetry can be attributed to the fact that the loops consist of two contributions, the longitudinal MOKE (LMOKE) giving rise to a signal odd in H and the quadratic MOKE (QMOKE) leading to a signal even in H. By symmetrization and antisymmetrization of experimental loops it is possible to separate LMOKE and QMOKE contributions, see section 6.8 in this report.

The LMOKE loops are used to determine the values of the coercive field H_C at different sample orientations and for different crystal structures. The resulting polar plots (Fig. 3) reveal four-fold magnetic anisotropy for all investigated samples, reflecting the cubic symmetry of the B2 and $L2_1$ structure. Moreover, in all cases sharp peaks in H_C appear when the applied magnetic field is aligned parallel to a hard direction. These peaks originate from a checkerboard domain pattern which occurs during the hard axes magnetization reversal processes as reported for thin $Co_2Cr_{0.6}Fe_{0.4}Al$ Heusler films in section 6.6 and in Ref. [4].

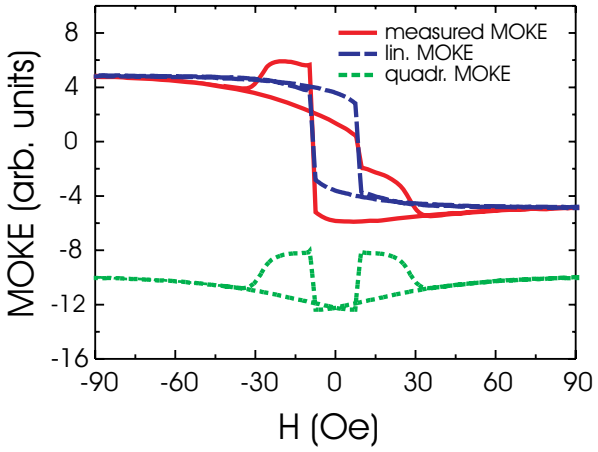

Fig. 2: Measured hysteresis loop for a B2 ordered CMS film at $\alpha = 44^\circ$ as well as LMOKE and QMOKE contributions determined from symmetrization and antisymmetrization of the experimental MOKE loop.

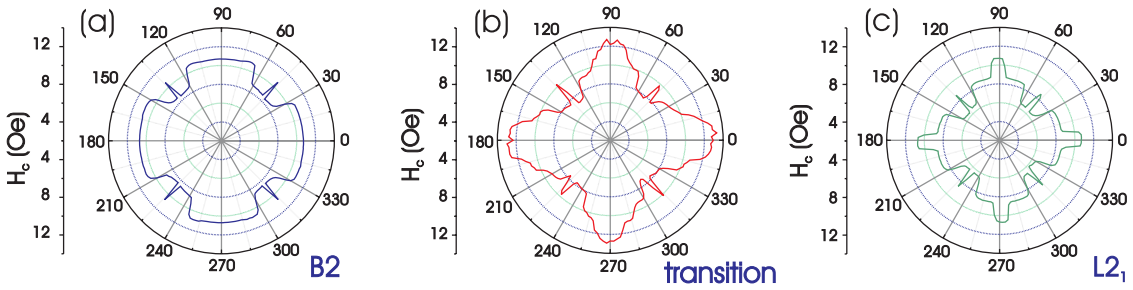

Fig. 3: Dependence of the coercive field H_C on sample orientation α for CMS films with (a) B2, (b) transition state and (c) $L2_1$ crystal structure. α denotes the angle between the in-plane [110]-direction of the CMS film and the plane of light incidence.

Figure 4 shows the dependence of H_C on the sample structure at four different values of α. At $\alpha = 0^\circ$ (i.e., reversal in the easy axis direction), the coercivity is 11 Oe for both the B2 and $L2_1$ structure. However, for the intermediate state, the coercivity is increased to 13 Oe. As the easy axis magnetization reversal is characterized by domain wall propagation, the increase of H_C for the transition sample is probably due to an increase of the number of pinning centers, which are provided by the existence of randomly distributed areas within the B2 and $L2_1$ structures during the transition. On the other hand, for all others sample orientations α (20°, 42° and 45°), H_C is reduced with increasing ratio of the $L2_1$ phase. At these orientations, the reversal starts by a coherent rotation of magnetization from the direction of the applied magnetic field towards the easy axis direction. In a subsequent stage, growth and propagation of magnetic domains takes place in which the magnetization is oriented in the easy axis direction. In both cases, the reversal behavior is governed by the anisotropy energy. Taking into account that the exchange interaction does not vary during the B2-$L2_1$ transition, the observed reduction of H_C is probably related to the reduction of the anisotropy energy during the transition from the B2 to the $L2_1$ structure.

In addition to standard linear MOKE, quadratic MOKE (QMOKE) was used to investigate the changes of magnetic properties of CMS films due to the B2 to $L2_1$ transition. QMOKE originates from second-order spin-orbit coupling as described in sections 6.8 and 6.9. It therefore exhibits

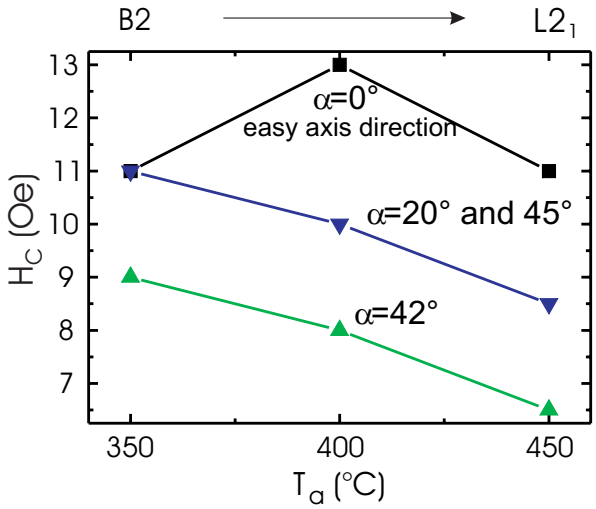

Fig. 4: Dependence of the coercive field H_C on the annealing temperature T_a for several sample orientations $\alpha = 0^\circ$, 20°, 42° and 45°. The coercivities for $\alpha = 20^\circ$ and $\alpha = 45^\circ$ are identical.

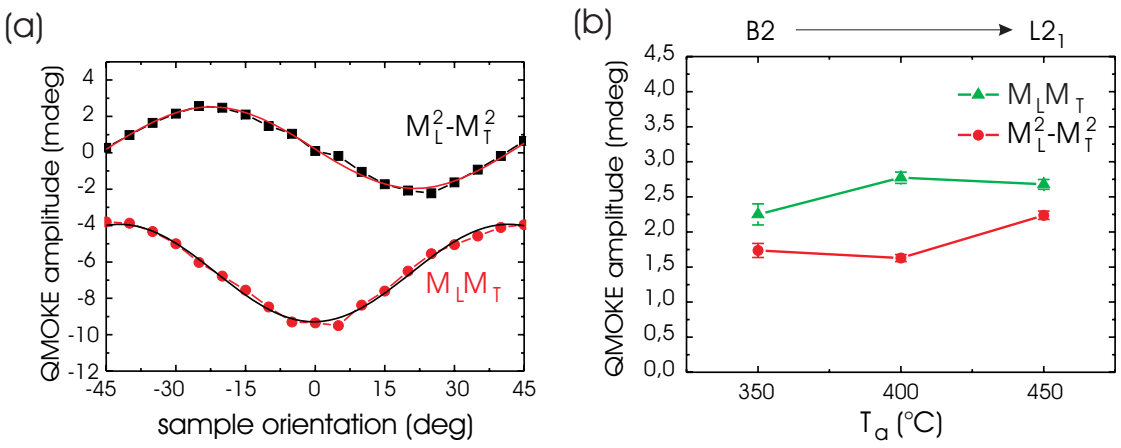

Fig. 5: (a) Dependence of the two contributions to the QMOKE on the sample orientation α for the CMS film with the $L2_1$ crystal structure. The data were acquired using the 8-directional method. (b) QMOKE amplitudes for both quadratic contributions $M_L M_T$ and $M_L^2 - M_T^2$ as a function of the crystal structure of the investigated CMS films.

high sensitivity to small changes of the crystal symmetry. In the experiment, the 8-directional method described for example in [5] was applied to determine the amplitudes of two contributions to the QMOKE signal being proportional to $M_L M_T$ and $M_L^2 - M_T^2$ terms.

Figure 5a shows both $M_L M_T$ and $M_L^2 - M_T^2$ contributions to the QMOKE signal for the CMS film with $L2_1$ structure. The data exhibit a clear oscillating dependence on the sample orientation α in accordance with theoretical predictions [5, 6]. The other two investigated CMS films reveal the same behavior (data are not shown here). When comparing the amplitudes of both quadratic contributions for films with various crystal structures (Fig. 5b) an interesting feature becomes evident. While the ratio for the QMOKE amplitudes proportional to $M_L M_T$ and $M_L^2 - M_T^2$ is nearly equal to one in the case of the B2 and $L2_1$ ordered samples, a splitting of amplitudes occurs for the sample in the intermediate state, which is clearly outside the experimental error. In particular, the amplitude of the $M_L M_T$ contribution is 60% larger compared to the corresponding value of $M_L^2 - M_T^2$. It should be emphasized that according to the theoretical predictions both amplitudes should be the same in the case of crystals with cubic symmetry. Therefore, the splitting of the amplitudes shows that during transition, the film does not exhibit a cubic symmetry any more. Additional structural studies are necessary to specify the distortion of the cubic symmetry which is present in this CMS film.

In conclusion, we have shown that the degree of disorder between the Mn and Si atomic sites does not influence the exchange interaction and the saturation magnetization of the CMS films by means of BLS technique. The coercivity, however, exhibits significant changes during the B2-$L2_1$ transition which depend on the crystallographic directions of the films. Finally, QMOKE studies indicate a distortion of the cubic symmetry in the intermediate state.

This work was supported by the NEDO International Joint Research Grant Program 2004/T093 and the Research Unit 559 *"New materials with high spin polarization"* funded by the DFG.

References

[1] S. Picozzi, A. Continenza, A.J. Freeman, Phys. Rev. B **69**, 094423 (2004).
[2] S.O. Demokritov, B. Hillebrands, A.N. Slavin, Physics reports **348**, 441 (2001).
[3] J. Hamrle, S. Blomeier, O. Gaier, B. Hillebrands, cond-mat/0609688 (2006).
[4] J. Hamrle, S. Blomeier, O. Gaier, B. Hillebrands, R. Schäfer, M. Jourdan, J. Appl. Phys. **100**, 103904 (2006).
[5] K. Postava, D. Hrabrovský, J. Pištora, A.R. Fert, Š. Višňovský, Y. Yamaguchi, J. Appl. Phys. **91**, 7293 (2002).
[6] R.M. Osgood, S.D. Bader, B.M. Clemens, R.L. White, H. Matsuyama, J. Magn. Magn. Mater. **182**, 297 (1998).

6.8 Huge quadratic magneto-optical Kerr effect in the Co_2FeSi Heusler compound

J. Hamrle, S. Blomeier, O. Gaier, and B. Hillebrands[1]

Studies of ferromagnetic half-metals are mainly driven by the possible applications for spintronic devices as a source of a 100% spin-polarized current. Heusler compounds (X_2YZ) are promising candidates for these applications due to the expected half-metallicity even for partially disordered systems, a high Curie temperature, high magnetic moments, as well as a good lattice mismatch allowing epitaxial growth on semiconductors.

We report on magneto-optical studies of the Co_2FeSi (CFS) Heusler compound [1], which recently attracted a lot of attention [2–4]. Up to now, CFS exhibits the highest observed Curie temperature (1100 K) and the highest magnetic moment (at 5 K average value $1.49\,\mu_B$ per atom) among the Heusler compounds and half-metallic ferromagnets [2].

We investigated CFS films with thicknesses of 11, 21, 42 and 98 nm, which were prepared by RF magnetron sputtering and deposited directly on MgO(001). CFS films were grown fully epitaxial forming a $L2_1$ structure [4]. All films were covered by a 4 nm thick Al protective layer. A detailed description of the sample preparation and its structural properties can be found in Ref. [4]. We investigated the CFS films using longitudinal (LMOKE) and quadratic (QMOKE) magneto-optical Kerr effect. As QMOKE is not a routinely used technique, we recall here some basic properties of both LMOKE and QMOKE.

The optical and magneto-optical properties of a magnetized crystal are described by the permittivity tensor ε_{ij}, which can be developed into a series in the components of the sample magnetization **M**:

$$\varepsilon_{ij} = \varepsilon_{ij}^{(0)} + K_{ijk}M_k + G_{ijkl}M_kM_l + \cdots \quad , \tag{1}$$

where the M_i are the components of **M**. The $\varepsilon_{ij}^{(0)}$, K_{ijk} and G_{ijkl} are constants, forming the dielectric tensor and the linear and quadratic magneto-optical tensors, respectively.

For cubic crystals (as in the case of CFS studied here), the number of independent tensor elements can be reduced expressively, resulting in only one free (complex) parameter in the constant term $\varepsilon_{ij}^{(0)}$, another one (called K) in the linear term K_{ijk} and three additional parameters called G_{11}, G_{12} and G_{44} in the quadratic term G_{ijkl} [5]

$$\varepsilon_{ij}^{(0)} = \varepsilon_d\delta_{ij} \tag{2-a}$$

$$K_{ijk} = -K_{jik} = K \quad , \quad K_{iik} = 0 \tag{2-b}$$

$$G_{ijkl} = G_{jikl} = G_{jilk} = G_{ijlk} \tag{2-c}$$

$$G_{iiii} = G_{11} \tag{2-d}$$

$$G_{iijj} = G_{12} \quad , \quad i \neq j \tag{2-e}$$

$$G_{1212} = G_{1313} = G_{2323} = G_{44} \quad , \tag{2-f}$$

[1] In collaboration with H. Schneider, G. Jakob and C. Felser, Johannes-Gutenberg-Universität Mainz, Germany, and K. Postava, Technical University of Ostrava, Czech Republic.

where δ_{ij} is the Kronecker delta-function. Assuming an in plane magnetization, the complex Kerr amplitudes $\Phi_{s/p}$ for a magnetized film with cubic symmetry, read

$$\Phi_{s/p} = \mp B_{s/p} K M_L \pm A_{s/p} \left[2G_{44} + \frac{\Delta G}{2}(1-\cos 4\alpha) \right] M_L M_T \mp A_{s/p} \frac{\Delta G}{4} \sin 4\alpha (M_L^2 - M_T^2) \quad , \quad (3)$$

where -(+) is related to using s(p) polarized incident light. M_L, M_T are longitudinal, transversal components of the sample magnetization, respectively, $A_{s/p}$, $B_{s/p}$ is even (odd) function of the angle of incidence, $\Delta G = G_{11} - G_{12} - 2G_{44}$ denotes the so-called magneto-optic anisotropy parameter, and α is sample orientation, being an angle between the plane of incidence of the light and the in-plane [100] direction of the CFS crystal lattice. Equation (3) shows several interesting features. (i) The first term, which is proportional to M_L, describes the ordinary LMOKE. (ii) The second and third terms are two separate QMOKE contributions, being proportional to $M_L M_T$ and $M_L^2 - M_T^2$, respectively. (iii) Contrary to LMOKE, the QMOKE signal strength depends on the crystallographic sample orientation α, characterized by the magneto-optic anisotropy parameter ΔG.

The Kerr measurements of CFS films were performed using s-polarized red laser light of a wavelength of $\lambda = 670\,\text{nm}$. Typical Kerr rotation MOKE loops $\theta(H)$ measured on CFS(21 nm) are presented in Fig. 1. The topmost two loops in Fig. 1 were measured at an angle of incidence of $\varphi = 45^\circ$ and a sample orientation of $\alpha = \pm 22.5^\circ$. Both loops are asymmetric as they contain LMOKE (odd in H) and QMOKE (even in H) contributions. The loops' asymmetric nature changes sign when the sample orientation is changed from $\alpha = 22.5^\circ$ to -22.5°, corresponding to changes of sign of the QMOKE contribution. On the other hand, when the sample orientation is 0° or 45° (not shown

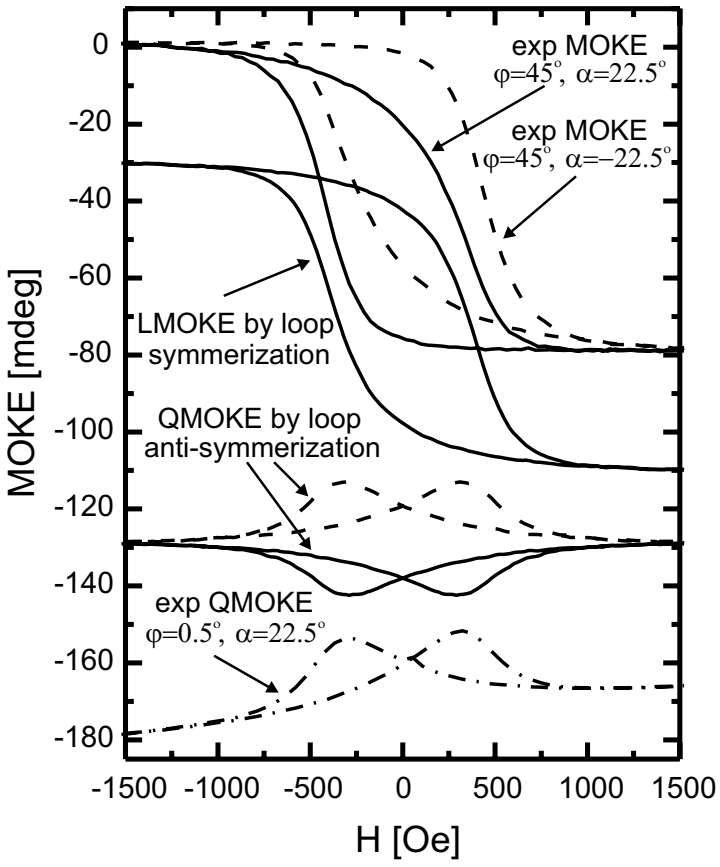

Fig. 1: MOKE loops recorded from the CFS(21 nm) sample. The topmost two loops were directly measured at $\varphi = 45^\circ$, $\alpha = 22.5^\circ$ (dashed line) and $\alpha = -22.5^\circ$ (full line), respectively. These two loops are symmetrized and anti-symmetrized (see text for details), providing LMOKE and QMOKE contributions. The bottom loop (dash-doted line) is a QMOKE loop directly measured at $\varphi = 0.5^\circ$ and $\alpha = -22.5^\circ$.

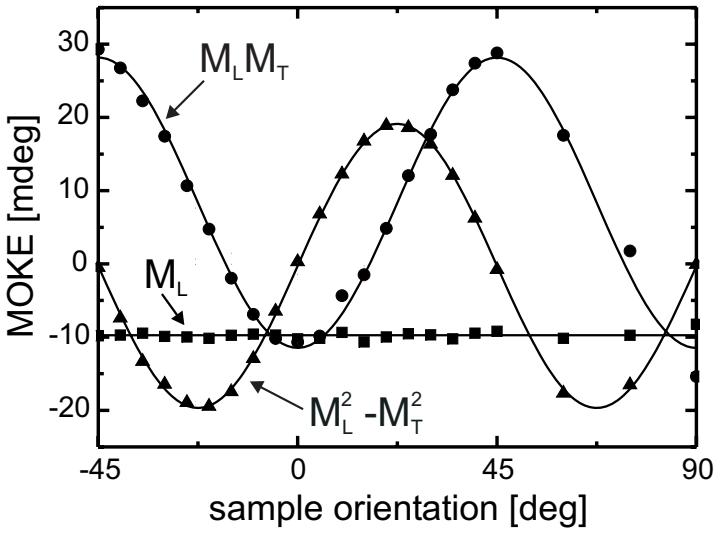

Fig. 2: Dependence of different MOKE signals at saturation for the CFS(21 nm) sample on the sample orientation α at $\varphi = 0.5°$, which are determined from the 8-directional method [5], see text.

in Fig. 1), the loops are symmetric, i.e., there is no QMOKE contribution in this case. These results are consistent with the expected fourfold symmetry of the QMOKE contribution, see Eq. (3).

Any Kerr rotation loop can be separated into its symmetric and antisymmetric parts as presented in Fig. 1 [6]. The symmetrized (LMOKE) loops are identical for $\alpha = \pm 22.5°$, so we show only one loop. Moreover, the antisymmetrized (QMOKE) loops differ only in sign in this case. Finally, the bottom loop (dash-dot line) shows the QMOKE loop as it is directly measured at a nearly normal angle of incidence of $\varphi \approx 0.5°$.

The LMOKE signal at saturation is experimentally determined as $\theta_{\mathrm{sat},M_\mathrm{L}} = [\theta(H_\mathrm{sat}) - \theta(-H_\mathrm{sat})]/2$, where H_sat is the saturation field of the sample. The QMOKE signal at saturation can also be determined by the so-called 8-directional method [5] where the Kerr signal is subsequently measured after application of an external field in eight different directions $\mathbf{H}_{0°}$ to $\mathbf{H}_{315°}$, when the field strength is sufficient to saturate the sample. $\mathbf{H}_\gamma$ denotes the in-plane magnetic field having an angle γ with respect to the plane of incidence of the light. Then, the LMOKE Kerr rotation signal at saturation is $\theta_{\mathrm{sat},M_\mathrm{L}} = [\theta(\mathbf{H}_{0°}) - \theta(\mathbf{H}_{180°})]/2$, while the QMOKE signal at saturation proportional to $M_\mathrm{L}M_\mathrm{T}$ and $M_\mathrm{L}^2 - M_\mathrm{T}^2$ reads

$$\theta_{\mathrm{sat},M_\mathrm{L}M_\mathrm{T}} = [\theta(\mathbf{H}_{45°}) + \theta(\mathbf{H}_{225°}) - \theta(\mathbf{H}_{135°}) - \theta(\mathbf{H}_{315°})]/4 \qquad \text{(4-a)}$$

$$\theta_{\mathrm{sat},M_\mathrm{L}^2 - M_\mathrm{T}^2} = [\theta(\mathbf{H}_{0°}) + \theta(\mathbf{H}_{180°}) - \theta(\mathbf{H}_{90°}) - \theta(\mathbf{H}_{270°})]/4 \quad . \qquad \text{(4-b)}$$

Figure 2 displays the angular dependence of the different MOKE signals at saturation of the CFS(21 nm) sample at an angle of incidence of $\varphi = 0.5°$. In agreement with Eq. (3), the LMOKE signal (■) is independent on α. The QMOKE signal related to $M_\mathrm{L}^2 - M_\mathrm{T}^2$ (▲) is proportional to $\sin(4\alpha)$, whereas the QMOKE signal related to $M_\mathrm{L}M_\mathrm{T}$ (•) is proportional to $\cos(4\alpha) + \text{const}$. The absolute vertical shift in the angular dependence of $M_\mathrm{L}M_\mathrm{T}$ is proportional to G_{44} [see Eq. (3)] whereas the amplitudes of both sinusoidal graphs are proportional to the anisotropy term ΔG. The QMOKE amplitude is 20 mdeg and the maximal QMOKE signal reaches 30 mdeg. To our knowledge, these values are the highest QMOKE amplitudes and signals in reflection that have ever been measured.

The experimental data in Fig. 2 show the same amplitude for both sinusoidal graphs whereas Eq. (3) predicts a factor of two between both amplitudes. This is due to $|M_\mathrm{L}| \leq |M|$, $|M_\mathrm{T}| \leq |M|$ and the product $|M_\mathrm{L}M_\mathrm{T}| \leq 1/2|M|^2$ due to the $\cos 45° = 1/\sqrt{2}$ factor entering as a prefactor both to M_L and M_T.

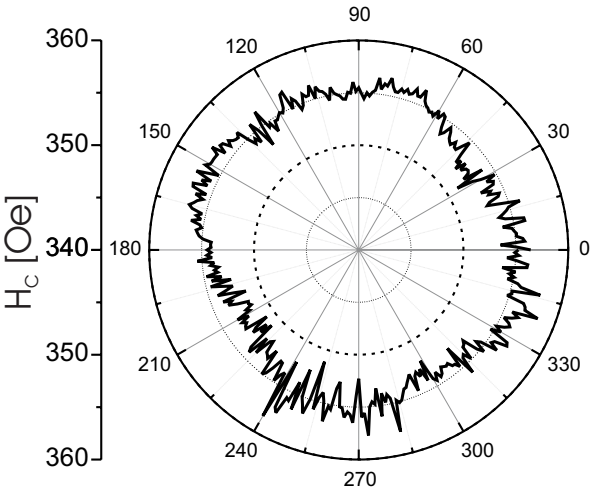

Fig. 3: Dependence of the coercive field on the sample orientation α as determined from symmetrized LMOKE loops in CFS(21 nm) sample.

Figure 3 displays a polar plot of the coercive field H_C as determined from LMOKE symmetrized loops for CFS(21 nm) sample. H_C is constant within the experimental error (which is about 1.5% in our case). The constant nature of H_C has been observed for all studied thicknesses of our CFS films. The reason for this is unclear at the moment. The constant nature of H_C is very surprising, as our CFS samples are epitaxial and therefore one should naively expect the presence of hard and easy axes. However, such hard and easy axes may still be present in our samples because, as has been shown from QMOKE loops [1], the magnetization reversal occurs by domain wall propagation.

In conclusion, the largest QMOKE observed thus far (up to 30 mdeg) was measured on the Co_2FeSi Heusler compound. It is a fingerprint of unusually large second or higher order spin-orbit coupling. Surprisingly, although the samples are epitaxial, they do not show an angular dependence of the coercivity.

The project was financially supported by the Research Unit 559 *"New materials with high spin polarization"* funded by the Deutsche Forschungsgemeinschaft, and by the Stiftung Rheinland-Pfalz für Innovation. Financial support by the European Commission within the EU-RTN ULTRASWITCH (HPRN-CT-2002-00318) is gratefully acknowledged.

References

[1] J. Hamrle, S. Blomeier, O. Gaier, and B. Hillebrands, (2006), submitted to J. Phys. D: Appl. Phys., cond-mat/cond-mat/0609688.
[2] S. Wurmehl, G. H. Fecher, H. C. Kandpal, V. Ksenofontov, C. Felser, and H.-J. Lin, Appl. Phys. Lett. **88**, 032503 (2006).
[3] K. Inomata, S. Okamura, A. Miyazaki, M. Kikuchi, N. Tezuka, M. Wojcik, and E. Jedryka, J. Phys. D: Appl. Phys. **39**, 816 (2006).
[4] H. Schneider, G. Jakob, M. Kallmayer, H. J. Elmers, M. Cinchetti, B. Balke, S. Wurmehl, C. Felser, M. Aeschlimann, and H. Adrian, in press, Phys. Rev. B (2006), cond-mat/0606666.
[5] K. Postava, D. Hrabovský, J. Pištora, A. R. Fert, Š. Višňovský, and T. Yamaguchi, J. Appl. Phys. **91**, 7293 (2002).
[6] T. Mewes, H. Nembach, M. Rickart, and B. Hillebrands, J. Appl. Phys. **95**, 5324 (2004).

6.9 Ion beam induced modification of exchange interaction and spin-orbit coupling in the Co_2FeSi Heusler compound

J. Hamrle, S. Blomeier, O. Gaier, and B. Hillebrands[1]

Here we study the influence of applied ion fluences on both the coercivity and the magneto-optical Kerr effect (MOKE) originating from Co_2FeSi (CFS) films [1]. The sample properties as well as the MOKE technique have been described in the previous Section 6.8.

We investigated a CFS film with a thickness of 11 nm, which was deposited directly on MgO(001). On the sample, 9 different areas of $\approx 1\,\mathrm{mm}^2$ size were defined, with eight of them being irradiated with different fluences of 30 keV Ga^+ ions varying from $3\times10^{14}\,\mathrm{ions/cm}^2$ to $9\times10^{16}\,\mathrm{ions/cm}^2$. The ninth area was left unirradiated for reference.

Magneto-optical Kerr effect (MOKE) hysteresis loops recorded from sample areas with different irradiation doses are shown in Fig. 1. The loops are measured at the incidence angle $\varphi = 45^\circ$ using s-polarized light at a wavelength of $\lambda = 670\,\mathrm{nm}$. The measured quantity is the Kerr rotation. The loops are presented for a sample orientation angle $\alpha = \pm 22.5^\circ$, which is the angle between the [100] CFS direction and the plane of incidence of the light. The loops in Fig. 1 exhibit several interesting features: (i) Both the coercivity H_C and the longitudinal MOKE (LMOKE) loop amplitude are decreasing as the ion fluence increases. The sample area which was irradiated with the highest fluence of $9\times10^{16}\,\mathrm{ions/cm}^2$ exhibits paramagnetic properties. (ii) The loops measured on the non-irradiated area show a large loop asymmetry. This asymmetry is related to a superimposed QMOKE contribution, as discussed in the previous Section 6.8. (iii) All loops recorded from the irradiated areas exhibit a much smaller asymmetry, i.e., a much smaller QMOKE contribution.

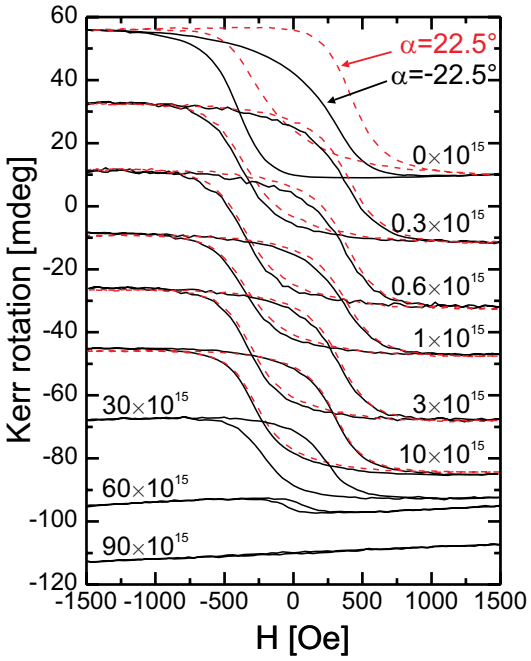

Fig. 1: MOKE hysteresis loops recorded from different areas of the CFS(11 nm) sample that were irradiated with different fluences of 30 keV Ga^+ ions. The sample orientation α is equal to 22.5° (dashed line) or -22.5° (full line), respectively.

[1] In collaboration with H. Schneider, G. Jakob, and C. Felser, Johannes-Gutenberg-Universität Mainz, Germany, B. Reuscher, A. Brodyanski and M. Kopnarski, Institut für Oberflächen- und Schichtanalytik, Technische Universität Kaiserslautern, Germany, and K. Postava, Technical University of Ostrava, Czech Republic.

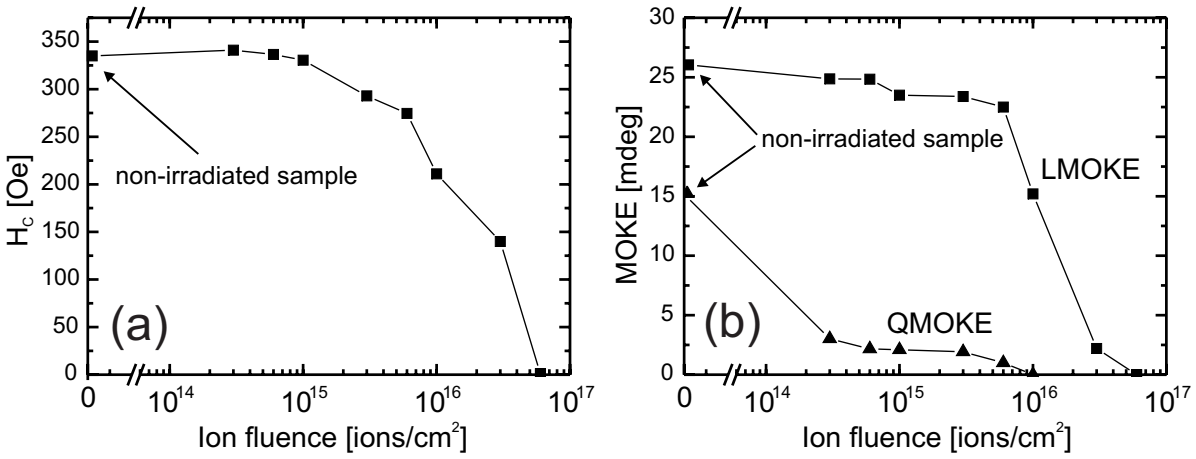

Fig. 2: Dependence of (a) H_C and (b) the amplitudes of the LMOKE and QMOKE of the CFS(11 nm) sample on the applied ion fluence.

The dependence of H_C, as well as the LMOKE and QMOKE amplitudes on the applied ion fluence is given in Fig. 2. H_C (Fig. 2a) and the LMOKE amplitude (Fig. 2b) show a similar behavior; they are decreasing very slowly with increasing ion fluence up to an ion fluence of $\approx 6 \times 10^{15}\,\mathrm{ions/cm^2}$. For higher fluences, both H_C and the LMOKE amplitude decrease faster and finally vanish at a fluence of $9 \times 10^{16}\,\mathrm{ions/cm^2}$ when the sample becomes paramagnetic. This behavior shows that the sample retains ferromagnetic properties up to high irradiation fluences, which is an indication that these properties are resistant to a certain degree of atomic disorder in the CFS structure.

Contrary to LMOKE, the QMOKE signal appears to be very sensitive to ion irradiation and, therefore, to atomic disorder of the CFS structure. The dependence of the QMOKE amplitude on the applied ion fluence is presented in Fig. 2b. The QMOKE amplitude of the non-irradiated area is equal to 15 mdeg, and it decreases rapidly to only 3 mdeg for the smallest ion fluence of $3 \times 10^{14}\,\mathrm{ions/cm^2}$. These results were corroborated by Kerr ellipticity measurements. We therefore conclude that the drop of the QMOKE signal upon irradiation is related to a change of the electronic structure of CFS.

It is known that QMOKE and LMOKE effects are related to the electronic structure of a given sample in different ways [2, 3]. Figure 3a presents a simplified sketch of the electronic structure of a ferromagnetic material for one point of the **k**-space [3]. Here, we limit ourselves only to $d \rightarrow p$ transitions, we assume no exchange between p-states, and we show only dipolar (i.e., optical) transitions to p states $|10\rangle$. In our simplified sketch, the exchange interaction E_{ex} splits only the d states into $d^{\uparrow}$ and $d^{\downarrow}$ for up- and down-electron levels, respectively. Furthermore, both $d^{\uparrow}$ and $d^{\downarrow}$ states are split by spin-orbit (SO) coupling E_{SO} according to the magnetic quantum number m of the electrons in the d states. Depending on the difference Δm of the magnetic quantum numbers between the final (here p) and initial (here d) states, circularly left ($\Delta m = -1$) or circularly right ($\Delta m = 1$) polarized photons can be absorbed by the electronic structure. The absorbtion spectra for both polarizations are sketched in Fig. 3b. When both exchange and SO coupling are present, the absorption spectra for the left and right polarized light are different. In such a case, a non-zero Kerr effect arises [3]. However, when either exchange or SO coupling is not present (i.e., $E_{\mathrm{ex}} = 0$ *or* $E_{\mathrm{SO}} = 0$), then the absorption spectra are identical, providing zero Kerr effect.

From a microscopic point of view, the LMOKE originates from a component of **M** parallel to **k** whereas the QMOKE originates from a component of **M** perpendicular to **k**, where **k** denotes the

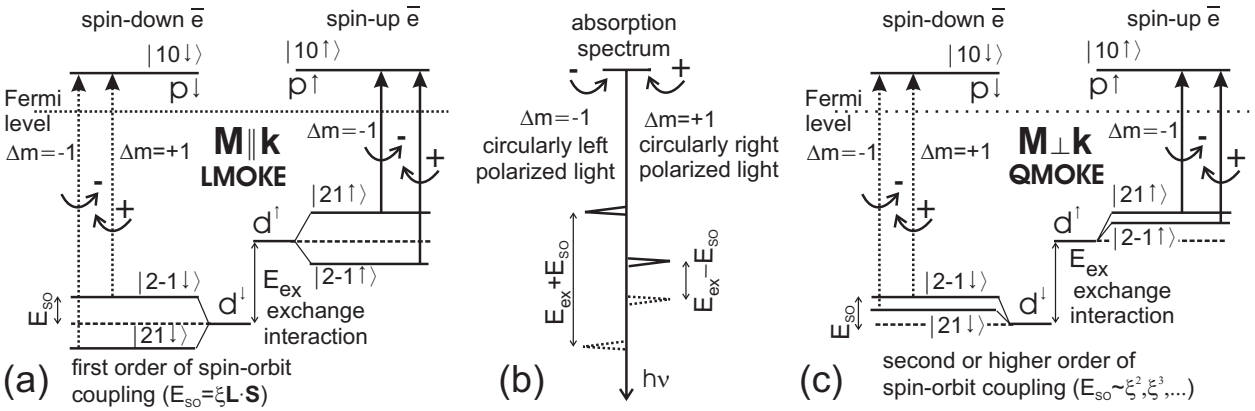

Fig. 3: Simplified sketch of the electronic structure for one point in the **k**-space for (a) $\mathbf{M} \parallel \mathbf{k}$ and (c) $\mathbf{M} \perp \mathbf{k}$, giving rise to LMOKE and QMOKE respectively. (b) illustrates absorption spectra of the dipolar (optical) transitions presented in (a). The presence of a Kerr effect requires that the absorption spectra must be different for left ($\Delta m = -1$) and right ($\Delta m = 1$) circularly polarized light, and therefore both exchange and spin-orbit interaction must be present. For more details see Ref. [1–3].

vector of propagation of light in matter [2]. In the following we discuss changes in the electronic structure for $\mathbf{M} \parallel \mathbf{k}$ (related to LMOKE) and $\mathbf{M} \perp \mathbf{k}$ (related to QMOKE), as sketched in Fig. 3a,c.

In the case of $\mathbf{M} \parallel \mathbf{k}$, the SO coupling is proportional to the spin-orbit coupling parameter ξ, $E_{\mathrm{SO}} = \xi \mathbf{L} \cdot \mathbf{S}$ (Fig. 3a). On the other hand, in the case of $\mathbf{M} \perp \mathbf{k}$, the first order SO coupling in ξ is zero, $\xi \mathbf{L} \cdot \mathbf{S} = 0$. Therefore only spin-orbit effects of second or higher order are able to remove the degeneracy of the initial or final state [2]. Usually, higher order SO coupling is much smaller than first order, $\xi \mathbf{L} \cdot \mathbf{S}$, leading to a much smaller QMOKE amplitude in comparison with the corresponding LMOKE amplitude in most materials.

According to the previous discussion, the suppression of the LMOKE amplitude by means of large applied ion fluences (from $\approx 6 \times 10^{15}\,\mathrm{ions/cm^2}$) may be understood either in terms of a reduction of exchange interaction or a reduction of the first order SO coupling. As the LMOKE exhibits a behavior similar to that of H_{C}, we may conclude that it is the exchange interaction in CFS which is reduced by large fluences of Ga^+ ions. On the other hand, the first order SO coupling seems to persist at such high fluences. If the SO coupling disappears for smaller fluences than the exchange, a decreasing LMOKE amplitude should be observed with increasing fluence but the magnetic properties of the sample (i.e., coercivity) should not vary drastically.

In conclusion, the effect of 30 keV Ga^+ ion irradiation on epitaxial Co_2FeSi (CFS) film having $L2_1$ structure and deposited onto MgO(001) was studied. Both the coercivity and the LMOKE exhibit a similar behavior on the applied ion fluence: they are nearly constant up to an ion fluence of about $6 \times 10^{15}\,\mathrm{ions/cm^2}$, after which they decrease and finally vanish at a fluence of about $9 \times 10^{16}\,\mathrm{ions/cm^2}$, when the sample becomes paramagnetic. The fluence dependence of the QMOKE signal varies significantly from the LMOKE behavior: The QMOKE amplitude is quickly reduced even for the smallest applied fluence of $3 \times 10^{14}\,\mathrm{ions/cm^2}$. The observed reduction of the QMOKE signal is attributed to an irradiation-induced degeneration of second or higher order contributions to the spin-orbit coupling, which already happens at small ion fluences. On the other hand, the reduction of the coercivity and the LMOKE amplitude at high ion fluences can be attributed to a reduction of exchange interaction within the irradiated areas.

The project was financially supported by the Research Unit 559 *"New materials with high spin polarization"* funded by the Deutsche Forschungsgemeinschaft, and by the Stiftung Rheinland-Pfalz

für Innovation. Financial support by the European Commission within the EU-RTN ULTRA-SWITCH (HPRN-CT-2002-00318) is gratefully acknowledged.

References

[1] J. Hamrle, S. Blomeier, O. Gaier, B. Hillebrands, H. Schneider, G. Jakob, B. Reuscher, A. Brodyanski, M. Kopnarski, K. Postava, and C. Felser, (2006), submitted to J. Phys. D: Appl. Phys., cond-mat/0609633.
[2] R. M. Osgood III, S. D. Bader, B. M. Clemens, R. L. White, and H. Matsuyama, J. Magn. Magn. Mater. **182**, 297 (1998).
[3] P. Bruno, Y. Suzuki, and C. Chappert, Phys. Rev. B **53**, 9214 (1996).

6.10 Domain wall fine structure in magnetically patterned multilayers

S. Blomeier, P. Candeloro, and B. Hillebrands[1]

Magnetic multilayers often exhibit physical properties which are different from those of magnetic single layers. This is especially true for the structure of magnetic domains and magnetic domain walls, which can be quite different from that of corresponding single thin films.

Antiferromagnetically coupled, epitaxial Fe/Cr/Fe (10 nm/0.7 nm/10 nm) trilayers magnetically patterned by ion irradiation are an excellent model system for the study of complex domain walls with different types of fine structure. It has been shown previously [1] that the irradiation of antiferromagnetically coupled Fe/Cr/Fe trilayers with sufficiently high fluences of keV ions leads to the destruction of the Cr interlayer and thereby induces a transition from antiferromagnetic to ferromagnetic interlayer coupling. Moreover, it has been demonstrated that if such an irradiation is performed locally, the irradiated areas exhibit properties of small ferromagnetic elements [2, 3]. Within this context it has also been shown that these elements are completely embedded into a surrounding, continuous, still antiferromagnetically coupled multilayer film, since the applied ion fluences are small enough that the topography of the bombarded samples is largely preserved. For this reason, elements of this type are referred to as “embedded elements” in the following.

Recent experimental investigations have shown that broad, complex domain walls with different types of fine structure form at the boundaries of these elements, i.e., at the boundaries between irradiated and non−irradiated areas. For example, Fig. 1a shows a magnetic force microscopy (MFM) image of a $5 \times 5\,\mu m^2$ square embedded element, whose edges are aligned parallel to the

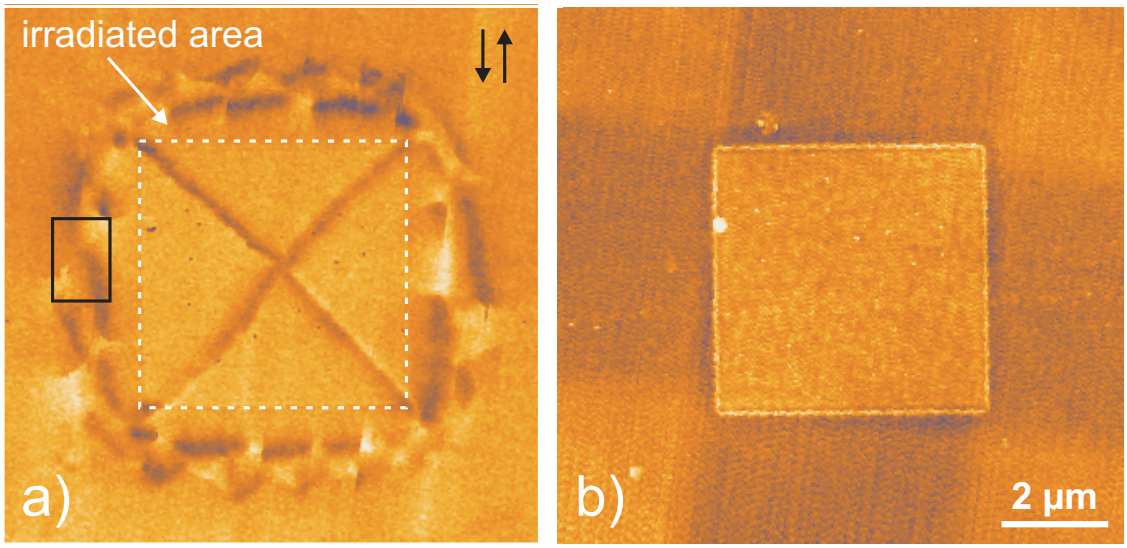

Fig. 1: MFM image of a $5 \times 5\,\mu m^2$ square element in remanence. The irradiated area is highlighted by a white dashed box, while a small black box marks the area which is shown in a blown up view in Fig. 5a. b) Corresponding AFM image. The difference in intensity within the non−irradiated area is an artifact resulting from an image processing procedure which is used to remove the mechanical tilt of the sample within the MFM setup. A topographic step of approximately 2 nm is measured between irradiated and non−irradiated areas.

[1] In collaboration with B. Reuscher, A. Brodyanski, M. Kopnarski, Institut für Oberflächen- und Schichtanalytik, Technische Universität Kaiserslautern.

easy axes of the fourfold magnetocrystalline anisotropy of the Fe layers. A classical Landau domain pattern within the irradiated area as well as domain walls at the boundary between irradiated and non−irradiated areas are clearly visible. Moreover, in contrast to previous measurements [3], the imaging resolution is now high enough to reveal that the domain walls at the boundary of the element are noticeably different from those walls inside the element. In particular, they are considerably broader than their counterparts inside the element and − unlike the latter − clearly exhibit an interesting, complex fine structure.

In order to understand the nature of these domain walls, some theoretical considerations concerning the magnetic configuration at the element boundaries are undertaken before the results displayed by Fig. 1a are discussed in more detail. For an element exhibiting a Landau−type flux−closure state like the one shown in Fig. 1a, two magnetic configurations at the boundary can be expected, as shown in Fig. 2. Each of these configurations corresponds to two of the four Landau domains depicted in Fig. 1a. It can be deduced from Fig. 2 that a domain wall must form at the boundary between irradiated and non−irradiated areas, but the exact nature of this domain wall remains a priori unclear. However, previous works [4–14] devoted to the nature of domain walls in magnetic trilayers provide some insight into what might be expected from a theoretical point of view. Within the scope of these works, trilayers of the form NiFe/X/NiFe were investigated, where X represents a non-magnetic interlayer material like C or SiO and both NiFe layers have the same thickness. These trilayers were either uncoupled or exhibited weak ferromagnetic coupling.

Some important results of these works which are relevant for the following considerations are now briefly summarized. Figure 3 shows several types of domain walls which were found to form within trilayers of the type mentioned above. In Fig. 3a, a superimposed Néel wall is shown, which consists of two Néel walls of opposite polarity forming on top of each other [4]. It was found that this type of wall is energetically more favorable than a single Néel wall in a magnetic single layer of comparable thickness, since the internal dipolar stray fields of the two walls largely compensate each other. In Fig. 3b, a so−called “twin wall” configuration is shown, which consists of a Néel wall and an adjacent-lying “quasi Néel wall” [9]. Although magnetic moments are tilted on a local scale in such a quasi Néel wall, the overall direction of magnetization does not change. Each quasi wall is either located on top or below a corresponding Néel wall and acts as a means to compensate the stray field of that wall, making this configuration energetically favorable. Twin walls of this type could indeed be detected experimentally [10–14], and, in addition, evidence was found that a Néel wall and its adjacent−lying quasi Néel wall companion can intercross each other [10].

Both Fig. 3a and Fig. 3b correspond to magnetic trilayers which are ferromagnetically coupled, as the magnetizations of the two ferromagnetic layers are always aligned parallel in the areas outside of the wall. For magnetically uncoupled systems, another possible configuration was found, which

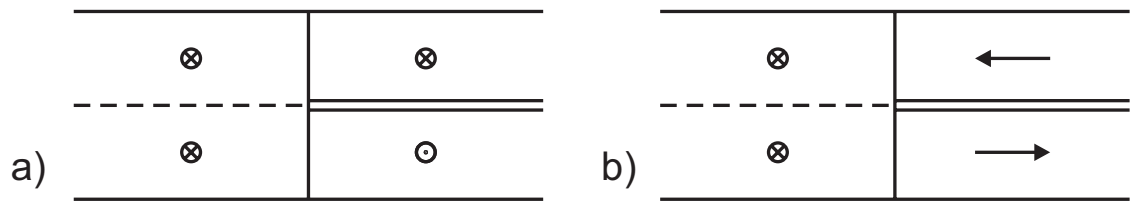

Fig. 2: Schematic illustration of two possible magnetic configurations in remanence at the boundary between irradiated and non−irradiated areas of the element shown in Fig. 1a. Panel a) corresponds to the left and the right of the four Landau domains shown in Fig. 1a, while panel b) displays the configuration at the boundary of the upper and lower Landau domains.

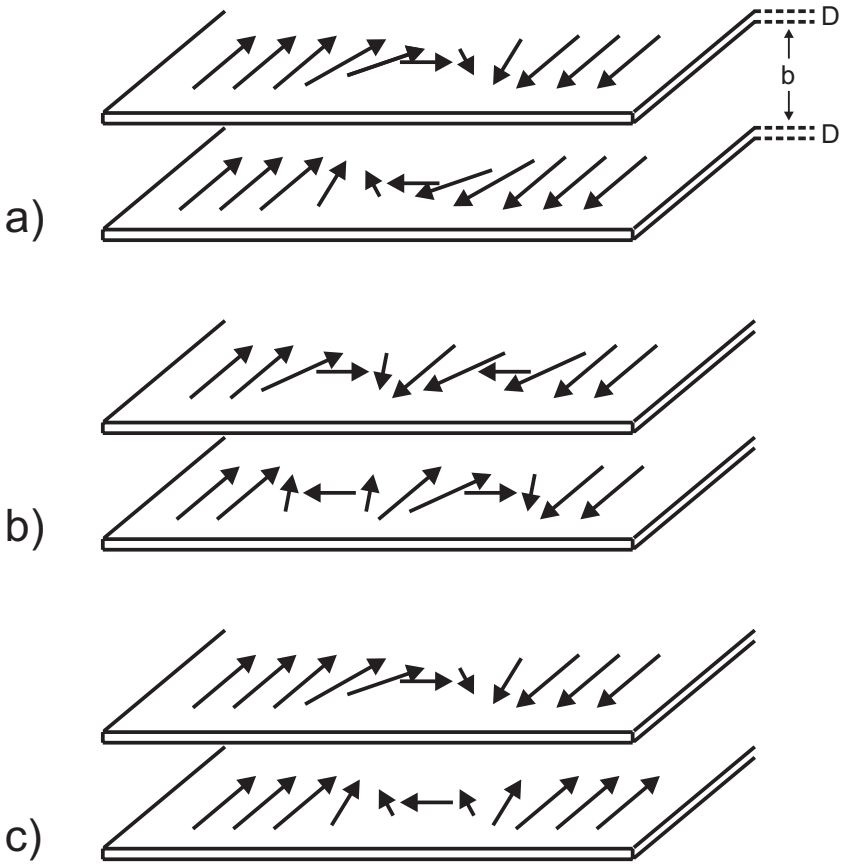

Fig. 3: Schematic illustration of domain wall configurations in magnetic trilayers. The trilayer shown here consists of two ferromagnetic layers of equal thicknesses D and an interlayer (omitted for the sake of clarity) of thickness b. a) Superposition of two 180°−Néel walls with opposite polarity. b) "Twin wall" configuration, consisting of a 180°−Néel wall and an adjacent−lying quasi Néel wall in each layer. Both panel a) and b) correspond to ferromagnetically coupled trilayers. c) Superposition of a 180°−Néel wall and a quasi Néel wall in a magnetically uncoupled trilayer.

is shown in Fig. 3c [8]. This configuration just consists of a single Néel wall in one of the layers and a corresponding quasi wall in the other layer. In the case displayed here, this domain wall forms between areas showing either parallel or antiparallel alignment of magnetizations, respectively. Experimental evidence was also found for the existence of this type of wall [10]. Moreover, there is no reason why a twin wall configuration similar to the one shown in Fig. 3b shouldn't also be possible in such systems. A twin wall of this type is shown in Fig. 4 (there also exists another possible configuration with oppositely aligned senses of rotation).

A comparison of Fig. 2 and Fig. 3c yields that the magnetic configurations which are investigated here are very similar to the situation encountered in magnetically uncoupled trilayers. In particular,

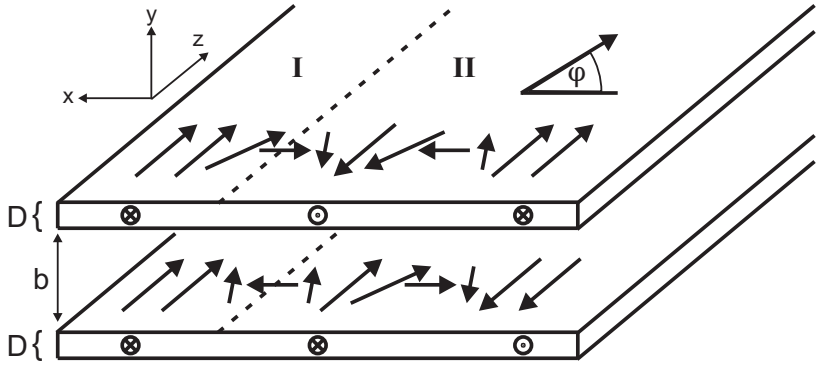

Fig. 4: Schematic illustration of a twin wall structure corresponding to the magnetic configuration shown in Fig. 3c. The left half of this configuration consists of a Néel/quasi Néel wall pair, while the right half is formed by two superimposed Néel walls of opposite polarity. φ denotes the local in−plane direction of magnetization.

the configuration displayed in Fig. 2a is equivalent to the ones shown in Fig. 3c and Fig. 4, either in the absence or in the presence of twin−like structures. Moreover, it is possible to approximate the width of the domain wall configuration displayed in Fig. 4. The width of the left wall segment marked by "I" can be calculated analytically by means of an integral wall width ansatz [15, 16], which is of the form

$$w = \int_0^{\pi/2} \sqrt{\frac{A + (A+S)\cos^2(\varphi)}{-2\frac{J_1}{D} + (4\frac{J_2}{D} + K_{c,1})\cos^2(\varphi)}}\ \mathrm{d}\varphi \quad , \tag{1}$$

where $A = 2.1 \cdot 10^{-11}\,\mathrm{J/m}$ and $K_{c,1} = 4.5 \cdot 10^4\,\mathrm{J/m^3}$ denote the exchange and the first order cubic anisotropy constants of Fe, while $J_1 = -1\,\mathrm{mJ/m^2}$ and $J_2 = -0.16\,\mathrm{mJ/m^2}$ represent the bilinear and biquadratic interlayer exchange coupling constants of the trilayer [17], which have been determined by Kerr magnetometry prior to irradiation. Moreover, the so−called "stray−field parameter" $S = \pi b D M_S^2$ contains information on the thickness $D = 10\,\mathrm{nm}$ and the saturation magnetization $M_S = 1800\,\mathrm{G}$ of the two ferromagnetic layers of the trilayer, as well as on the interlayer thickness $b = 0.7\,\mathrm{nm}$. A complete derivation of Eq. 1 through a variational minimization ansatz of the total wall energy can be found in Ref. [18].

Using the above values, Eq. 1 yields an integral wall width of $w = 85\,\mathrm{nm}$ by numerical evaluation. As it can be seen from Eq. 1, the interlayer exchange coupling formally plays the role of an additional anisotropy contribution that tends to decrease the wall width in this case. In the part of the wall marked by a "II", magnetic moments in the two layers are always aligned antiparallel, and the now constant contribution of the interlayer coupling to the total wall energy vanishes in the variational derivative and therefore also in Eq. 1. Hence, it can be estimated that the width of corresponding wall segments in this part of the wall is even larger. In the absence of twin−like structures, as shown in Fig. 3c, it can therefore be estimated that the total width of the wall is larger than twice the width calculated above, i.e. larger than 170 nm. If twin−like structures are present, as it is the case in Fig. 3, the wall width should even be at least four times larger than the value calculated by Eq. 1, i.e. larger than 340 nm. Unfortunately, a quantitative comparison of these values to experimental data from magnetic force microscopy measurements should not be feasible. As it has been shown by detailed micromagnetic simulations, the widths of domain walls measured by magnetic force microscopy are always noticeably larger than the widths of the underlying magnetic configurations [19, 20]. Hence, it may be expected that experimentally measured "widths" are significantly larger than the above results, possibly approaching values of 500 nm −1 µm. Moreover, it can be expected that these walls appear to be significantly broader than the classical 90° Néel walls within the Landau configuration of square embedded elements, which, according to micromagnetic simulations, exhibit an integral wall width of approximately 160 nm.

In the following, the configuration displayed in Fig. 2b is discussed. This configuration corresponds to a different situation. If $\mathbf{n}$ denotes the normal vector in the direction of the wall normal, $\mathbf{m}_F$ the magnetization direction within the irradiated, ferromagnetically coupled area, and $\mathbf{m}_{AF}^u$ and $\mathbf{m}_{AF}^l$ represent the magnetization directions within the upper and lower Fe layer in the antiferromagnetically coupled area, then it can be easily seen from Fig. 2b that

$$\mathbf{n} \cdot (\mathbf{m}_F - \mathbf{m}_{AF}^u) \neq 0 \tag{2-a}$$

$$\mathbf{n} \cdot (\mathbf{m}_F - \mathbf{m}_{AF}^l) \neq 0 \tag{2-b}$$

is valid for this configuration. This condition is equivalent with $\nabla \cdot \mathbf{M} \neq 0$ at the boundary between irradiated and non−irradiated areas for both cases (see, e.g., Ref. [16]), which means that the domain walls which are expected to form in the case displayed in Fig. 2b cannot be free of magnetic charges. Charged domain walls have indeed been observed experimentally (also in magnetic trilayers, but with a much wider spacing) [21], and a theoretical treatment of such walls in thin films has been performed in Ref. [22]. A striking feature of these walls is their tendency to assume a "zig−zag"−shaped configuration which is considerably broader than a classical uncharged domain wall [21, 22]. However, up to now only walls in materials with uniaxial anisotropy have been treated theoretically, in contrast to the situation with fourfold anisotropy which is encountered here. Still, the observation of a broadened, zig−zag−shaped wall configuration should not be totally unexpected also in this case.

To summarize the above considerations, several conclusions can be drawn on what might be expected at the boundary of the embedded ferromagnetic elements studied here. First, domain walls between irradiated and non−irradiated areas should form in the non−irradiated, still antiferromagnetically coupled regions outside of a particular element, due to the energetically more favorable stray−field compensation mechanism for such wall configurations. Second, domain walls of this type might exhibit some fine structure, in particular of twin wall or "zig−zag"−shape type. Finally, if such a fine structure is present, the corresponding domain walls at the boundary of an element should be noticeably broader than classical 90° Néel walls within a single Fe layer of comparable thickness, such as those forming inside an embedded element.

It is instructive to return to the study of the MFM image of the $5 \times 5\,\mu m^2$ square element depicted in Fig. 1a, in particular with respect to the complicated, broad domain walls at the boundary of this element. A comparison of the magnetic configuration with the size of the irradiated area (represented by a dashed white box), which is rather sharply defined and which can easily be determined from the corresponding AFM image (see Fig. 1b), yields that these domain walls indeed form directly outside of the element. A close inspection of these domain walls indicates a twin−like structure outside of all four of the square's edges. Moreover, while the outer wall segments outside of the two vertical edges appear to be rather smooth, the corresponding segments outside of the two horizontal edges exhibit a characteristic "zig−zag"−shape, indicating the presence of non−vanishing magnetic charges. It can thus be concluded that the magnetic configurations along the vertical square edges correspond to the configuration shown in Fig. 4, while the configurations along the horizontal square edges correspond to the situation displayed in Fig. 2b. Hence, the magnetizations of the two ferromagnetic layers within the antiferromagnetically coupled areas

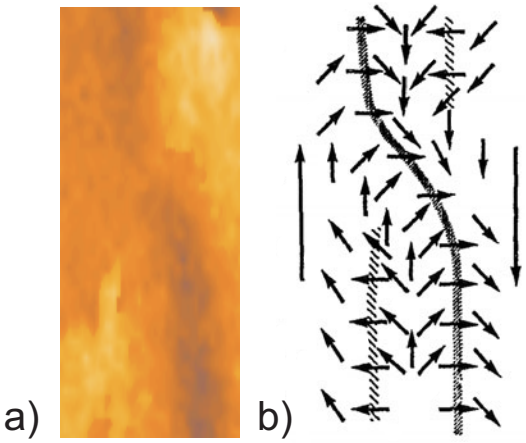

Fig. 5: a) Detail from the MFM image displayed in Fig. 1a, showing the area marked by the small black box. b) Micromagnetic configuration model of an intercrossing twin wall, adapted from Ref. [12].

should be aligned as indicated by the two small black arrows in Fig. 1a. Moreover, in all cases the observed magnetic contrast is much broader than the contrast obtained from the 90° walls within the Landau flux−closure pattern, as expected.

In addition, at the vertical boundaries of the magnetic configuration, the two wall segments of the twin wall appear to intercross each other (which seems to happen at the left edge) or change their polarity (which is more likely to happen at the right edge). In particular, a comparison of the area marked by a small black box in Fig. 1a, which is shown in Fig. 5a in a blown up view, with a micromagnetic configuration model of an intercrossing twin wall, which is shown in Fig. 5b and which has been adapted from Ref. [12], yields a remarkable coincidence.

Domain wall fine structure of the type discussed above has also been observed for elements with different geometries (see, e.g., Ref. [18]). The results presented here offer new insights into the physics of magnetic domain walls and into the magnetostatic properties of a classical magnetic multilayer system.

This work has been accepted for publication in Physical Review B. Support from the Deutsche Forschungsgemeinschaft is gratefully acknowledged.

References

[1] S.O. Demokritov, C. Bayer, S. Poppe, M. Rickart, J. Fassbender, B. Hillebrands, D.I. Kholin, N.M. Kreines, O.M. Liedke, Phys. Rev. Lett. **90**, 097201 (2003).
[2] V.E. Demidov, D.I. Kholin, S.O. Demokritov, B. Hillebrands, F. Wegelin, J. Marien, Appl. Phys. Lett. **84**, 2853 (2004).
[3] S. Blomeier, B. Hillebrands, V.E. Demidov, S.O. Demokritov, B. Reuscher, A. Brodyanski, M.Kopnarski, J. Appl. Phys. **98**, 093503 (2005).
[4] H. Clow, Nature **194**, 1035 (1962).
[5] J.C. Slonczewski, J. Appl. Phys. **37**, 1268 (1966).
[6] S. Middelhoek, Appl. Phys. Lett. **5**, 70 (1964).
[7] J.C. Slonczewski, S. Middelhoek, Appl. Phys. Lett. **6**, 139 (1965).
[8] S. Middelhoek, J. Appl. Phys. **37**, 1276 (1966).
[9] F. Biragnet, J. Devenyi, G. Clerc, O. Massenet, R. Montmory, A. Yelon, Phys. Stat. Sol. **16**, 569 (1966).
[10] H. Niedoba, A. Hubert, B. Mirecki, I.B. Puchalska, J. Magn. Magn. Mater. **80**, 379 (1989).
[11] H. Niedoba, H.O. Gupta, L.J. Heyderman, I. Tomas, I.B. Puchalska, IEEE Trans. Magn. **26**, 1527 (1990).
[12] H. Niedoba, L.J. Heyderman, H.O. Gupta, I.B. Puchalska, A. Hubert, J. Appl. Phys. **69**, 5865 (1991).
[13] H.O. Gupta, H. Niedoba, L.J. Heyderman, I. Tomas, I.B. Puchalska, C. Sella, J. Appl. Phys. **69**, 4529 (1991).
[14] L.J. Heyderman, H. Niedoba, H.O. Gupta, I.B. Puchalska, J. Magn. Magn. Mater. **96**, 125 (1991).
[15] M. Rührig, A. Hubert, J. Magn. Magn. Mater. **121**, 230 (1993).
[16] A. Hubert, R. Schäfer, Magnetic Domains. The Analysis of Magnetic Microstructures. Springer, Berlin−Heidelberg−New York (2000).
[17] D.E. Bürgler et al., Handbook of Magnetic Materials, Vol. 13, edited by K.J.H. Buschow, Elsevier, Amsterdam (2001).
[18] S. Blomeier, P. Candeloro, B. Hillebrands, B. Reuscher, A. Brodyanski, M.Kopnarski, Phys. Rev. B, in press.
[19] S. Müller-Pfeiffer, M. Schneider, W. Zinn, Phys. Rev. B **49**, 15745 (1994).
[20] S. Huo, J.E.L. Bishop, J.W. Tucker, J. Appl. Phys. **81**, 5239 (1997).
[21] L.A. Finzi, J.A. Hartman, IEEE Trans. Magn. **4**, 662 (1968).
[22] A. Hubert, IEEE Trans. Magn. **15**, 1251 (1979).

6.11 Observation of domain wall splitting in rectangular embedded ferromagnetic elements

S. Blomeier, P. Candeloro, and B. Hillebrands[1]

Magnetic domain walls are physical entities which come in great variety in nature. A multitude of parameters like film thicknes, exchange stiffness, magnetic anisotropy, absence or presence of magnetic charges, as well as the lateral geometry of a magnetic system determine the nature of its domain walls. A particularly interesting case are 180° walls in materials with fourfold anisotropy, like, for instance, epitaxial Fe. Usually, such domain walls are not encountered in bulk Fe crystals or thin Fe films, as the formation of energetically more favorable 90° walls in (110)−direction takes place instead. For example, the domain walls within the Landau configuration displayed by Fig. 1a of Section 6.10 of this report are of this type. These domain walls form within an embedded ferromagnetic microelement, whose lateral geometry influences the shape of its remanent magnetic domain configuration (see Section 6.10 for information on the fabrication of such elements).

If rectangular elements with an aspect ratio larger than 1 are investigated, the situation within the element itself changes. In Fig. 1a, a magnetic force microscopy (MFM) image of a $5 \times 2\,\mu m^2$ rectangular element is shown in remanence. A flux closure state is observed, which, however, in this case is no longer square−like. Instead, a 180° wall segment is observed within the center of the element. A close inspection of this wall segment reveals that it is considerably wider than the corresponding 90° walls of the flux closure state and exhibits an irregularly shaped but clearly visible “gap” in its center. This observation leads to the conclusion that this 180° wall consists of two 90° wall segments, which are separated at a small, but noticeable distance from each other. This phenomenon has been predicted by Néel [1] and Lifshitz [2] (see also Ref. [3]) for bulk materials and is specific to 180° walls in magnetic materials with fourfold anisotropy. In such a system, the 90° orientation in the center of the wall is energetically favorable as it corresponds

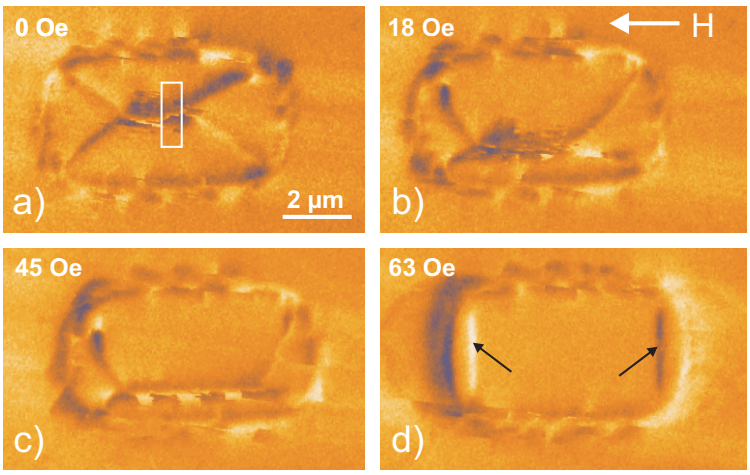

Fig. 1: Magnetization reversal of a $5 \times 2\,\mu m^2$ rectangular embedded ferromagnetic element, recorded by MFM. The images correspond to external field values of a) 0 Oe, b) 18 Oe, c) 45 Oe, and d) 63 Oe. The direction of the externally applied field is indicated by a white arrow in panel b).

[1] In collaboration with B. Reuscher, A. Brodyanski, M. Kopnarski, Institut für Oberflächen- und Schichtanalytik, Technische Universität Kaiserslautern.

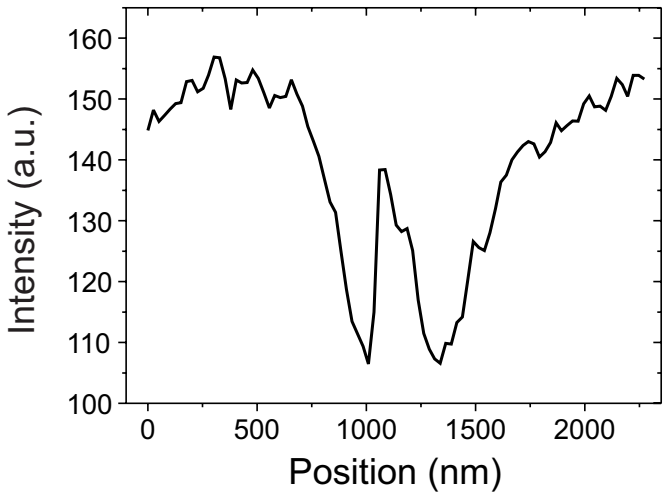

Fig. 2: Intensity profile of the 180° domain wall in the center of the flux closure state shown in Fig. 1a. The profile was averaged over the rectangular area highlighted by a white box in Fig. 1a.

to one of the magnetic easy axes. Hence, if only exchange and anisotropy contributions to the total wall energy are considered, the system becomes energetically degenerate, as the two 90° wall segments can be spaced at an arbitrary distance from each other without changing the wall's total energy. However, due to magnetostrictive contributions to the total wall energy, this distance is limited to a finite value, which is of the same order of magnitude as the gap observed in the experiment discussed here [3]. Figure 2 displays an intensity profile of this 180° wall averaged across the rectangular area which is highlighted by a white box in Fig. 1 a). Two wall segments which are separated from each other are clearly visible and confirm previous observations.

If an external field is applied, the 180° wall segment moves to the bottom edge of the configuration, thereby enlarging the now energetically favorable domain (Fig. 1b). It remains pinned there up to field strengths of at least 45 Oe (Fig. 1c). At a field strength of 63 Oe, however, the element has reached a saturated single domain state (Fig. 1d). In this state, two vertical lines of magnetic contrast are visible which are marked by black arrows. These lines appear due to a topographic contrast mechanism discussed in Ref. [4]. They indicate the precise location of the irradiated area within the magnetic image. From this image it becomes very clear that also for this element geometry the magnetic configuration always extends beyond the irradiated area and is limited by domain walls in the antiferromagnetically coupled region.

From the experiments discussed above it becomes evident that not only magnetic domain walls at the boundary of embedded ferromagnetic elements may exhibit an interesting fine structure but also those inside these elements.

This work has been accepted for publication in Physical Review B. Support from the Deutsche Forschungsgemeinschaft is gratefully acknowledged.

References

[1] L. Néel, Cahiers de Phys. **25**, 21 (1944).
[2] E. Lifshitz, J. Phys. USSR **8**, 337 (1944).
[3] A. Hubert, R. Schäfer, Magnetic Domains. The Analysis of Magnetic Microstructures. Springer, Berlin−Heidelberg−New York (2000).
[4] S. Blomeier, P. Candeloro, B. Hillebrands, B. Reuscher, A. Brodyanski, M. Kopnarski, Phys. Rev. B, in press.

6.12 Ion beam induced magnetic nanopatterning of Fe/Cr/Fe trilayers

S. Blomeier, P. Candeloro, and B. Hillebrands[1]

In recent years, ion irradiation has developed into a convenient tool for magnetic patterning. Material systems such as CoPt multilayers with out−of−plane anisotropy [1], exchange bias bilayers [2] and other magnetic thin film systems [3, 4] have been magnetically patterned through local irradiation with keV ions. A major advantage of this technique is that the fluence ranges which are necessary to achieve a magnetic patterning effect are usually low enough that the topography of the bombarded systems is largely preserved. This property makes ion irradiation a promising candidate for technological applications. Previous publications [5, 6] have shown that antiferromagnetically coupled trilayer systems can also be magnetically patterned by means of local irradiation with keV ions. This patterning process leads to the formation of so−called "embedded ferromagnetic elements", which is described in more detail within Section 6.10 of this report. Elements of this type of with lateral dimensions of $20 \times 20\,\mu m^2$ −were found to form a Landau−type domain structure if the areas have a square geometry with their edges aligned parallel to the easy axes of the fourfold magnetocrystalline anisotropy of the Fe layers [6]. In a recent work, elements of smaller (including submicron) sizes were investigated, using magnetic force microscopy (MFM), and an effective intrinsic spatial resolution limit of the patterning method employed here was determined.

MFM investigations yielded that elements of sizes $1 \times 1\,\mu m^2$ or larger consistently exhibit a Landau−type domain structure in remanence, as demonstrated for the $20 \times 20\,\mu m^2$ −element in Ref. [6]. Moreover, upon application of an external field, in each case a magnetization reversal process takes place which is qualitatively similar to the one displayed previously [6] (the field is applied in−plane and parallel to a square edge). However, the saturation field of each element, i.e., the value of the external field which is necessary to saturate such an element in a magnetic single domain state (as observed by MFM), was found to be dependent on its lateral size.

Figure 1 displays the dependence of the saturation field on the size of 20 nm thick square elements. For element sizes of 2 µm and larger, it is found that the saturation field decreases with increasing element size, which can be attributed to the demagnetizing field of these elements that is roughly inversely proportional to its lateral dimensions. However, for element sizes of 1 µm and smaller,

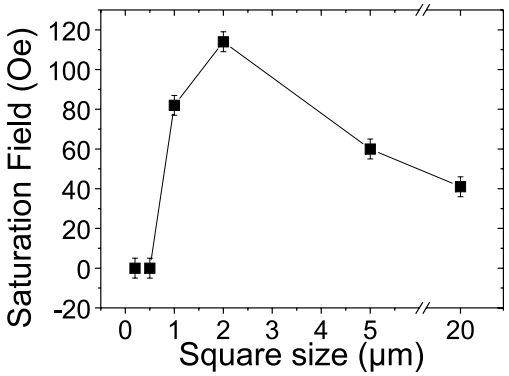

Fig. 1: Dependence of the saturation field on the size of 20 nm thick square embedded elements.

[1] In collaboration with B. Reuscher, A. Brodyanski, M. Kopnarski, Institut für Oberflächen- und Schichtanalytik, Technische Universität Kaiserslautern.

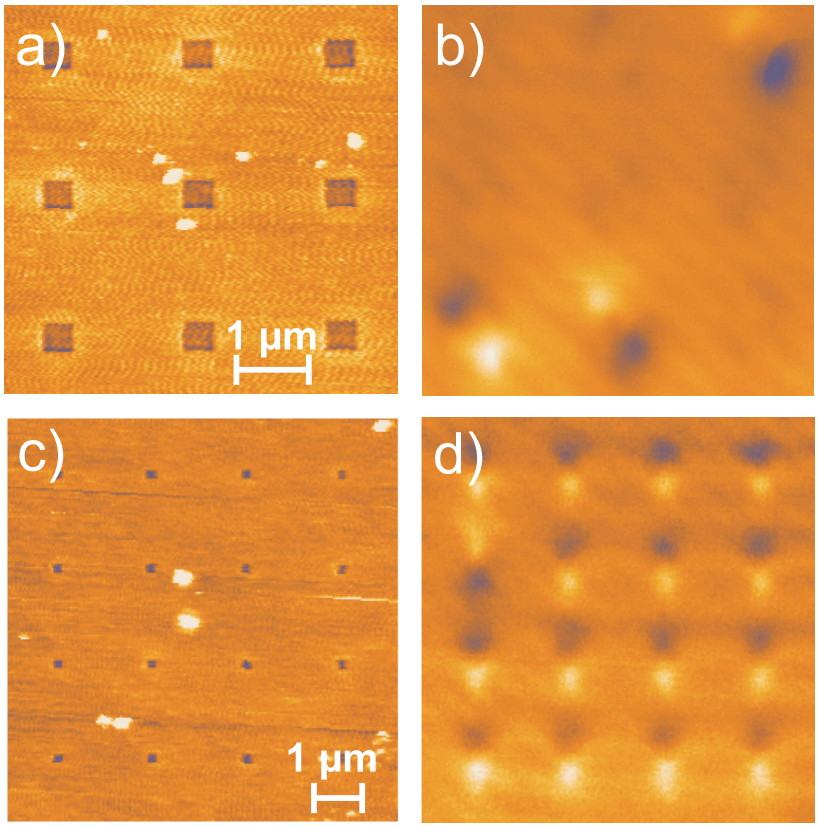

Fig. 2: a) AFM image of an array of $500 \times 500\,\mathrm{nm}^2$ or c) $200 \times 200\,\mathrm{nm}^2$ irradiated areas. b) + d) Corresponding MFM images in remanence.

the saturation field is found to decrease with *decreasing* element size. In particular, at an element size of 500 nm, a transition to a single domain state in remanence (i.e. a saturation field of 0 Oe) can be observed for some (but not all) elements. This is shown in Figs. 2a and b, which display an atomic force microscopy (AFM) image of an array of $500 \times 500\,\mathrm{nm}^2$ elements with a 2 µm spacing and the corresponding MFM image in remanence, respectively. Upon close inspection it can be observed in Fig. 2b that some of the elements still exhibit a Landau domain pattern (which is barely visible even in an enlarged view), while the remaining elements have assumed a magnetic single domain configuration that produces much stronger contrast. It can thus be deduced that a multi−domain to single domain transition, which is characteristic for many magnetically patterned material systems, occurs at this element size. This is not an unexpected result, as element sizes in the sub−micron range are approaching the width of the 90° domain walls of the Landau domain patterns within such elements in remanent configurations. Correspondingly, it can be expected that below a certain threshold it is energetically more favorable for such an element to assume a single domain state in remanence instead of the multi−domain configurations observed for larger element sizes.

If the element size is further reduced to 200 nm, all elements exhibit a single domain configuration in remanence, which is shown in Fig 2d. Moreover, it can be observed from Fig. 2d that the magnetic configuration surrounding each element is noticeably larger than the element itself and is of the order of 500 nm to 1 µm in size. This configuration is caused by magnetic interactions in lateral direction which are discussed in more detail within Section 6.10 of this report. These interactions constitute an effective intrinsic limit to the spatial resolution of the patterning method investigated here.

In conclusion, the feasibility of ion beam−induced magnetic nanopatterning of interlayer exchange coupled Fe/Cr/Fe trilayers was demonstrated, and an intrinsic resolution limit of this patterning method was determined.

This work has been accepted for publication in Journal of Magnetism and Magnetic Materials. Support from the Deutsche Forschungsgemeinschaft is gratefully acknowledged.

References

[1] C. Chappert, H. Bernas, J. Ferré, V. Kottler, J.-P. Jamet, Y. Chen, E. Cambril, T. Devolder, F. Rousseaux, V. Mathet, H. Launois, Science **280** 1919 (1998).
[2] J. Fassbender, S. Poppe, T. Mewes, A. Mougin, B. Hillebrands, D. Engel,M. Jung, A. Ehresmann, H. Schmoranzer, G. Faini, K.J. Kirk, J.N. Chapman, Phys. Stat. Sol. (a) **189** 439 (2002).
[3] D. McGrouther, J.N. Chapman, Appl. Phys. Lett. **87** 022507 (2005).
[4] J. McCord, T. Gemming, L. Schultz, J. Fassbender, M.O. Liedke, M. Frommberger, E. Quandt, Appl. Phys. Lett. **86** 162502 (2005).
[5] V.E. Demidov, D.I. Kholin, S.O. Demokritov, B. Hillebrands, F. Wegelin, J. Marien, Appl. Phys. Lett. **84** 2853 (2004).
[6] S. Blomeier, B. Hillebrands, V.E. Demidov, S.O. Demokritov, B. Reuscher, A. Brodyanski, M.Kopnarski, J. Appl. Phys. **98** 093503 (2005).

6.13 Remanence capabilities of embedded ferromagnetic elements

S. Blomeier, P. Candeloro, and B. Hillebrands[1]

Embedded ferromagnetic elements (see Section 6.10 for information on the fabrication of such elements) are interesting candidates for magnetic data storage applications, mainly for the following two reasons: Contrary to conventional patterned data storage media, a medium consisting of embedded elements does not exhibit any topographic steps, as the elements are completely integrated into a smooth, continuous multilayer film. In addition, the area surrounding the elements consists of an antiferromagnetically coupled trilayer system with a very low magnetic susceptibility and is therefore virtually free of perturbative dipolar stray fields. However, a magnetic element that is to be used for data storage purposes must not only be able to store information in the form of magnetic single domain states, but it must also be capable of maintaining these states when the externally applied writing field is switched off. For this purpose, the magnetic relaxation behavior of embedded elements with different geometries was studied.

Figure 1 displays several MFM images of elements in a saturated single domain state (Figs. 1a, c, e, and g) and corresponding images upon returning to remanence (Figs. 1b, d, f, and h). It can be observed that the transversely saturated rectangular element relaxes into a so−called “diamond” flux−closure state (which is somewhat blurred in the center), consisting of seven domains (Fig 1b). The square element relaxes into a more irregular state, which was found to be consistent for several square sizes (Fig. 1d). The longitudinally magnetized rectangular element nearly maintains its single domain state upon returning to remanence and assumes a so−called “S−state” with small flux closure domains at the ends of the rectangle (Fig. 1f).

The relaxation behavior of both the longitudinally and the transversely magnetized rectangular embedded element has been found to be similar to that of corresponding topographically patterned Fe elements, according to micromagnetic simulations by means of the OOMMF software [1]. The results of these simulations are shown in Fig. 2. Apart from the 180° wall segments containing two cross−ties each in the diamond configuration, which are not observed in the experiment, a general similarity between experimental and simulated configurations can be observed. In addition, the simulations performed here indicate that the S−state observed in the case of the longitudinally magnetized element is induced by a slight misalignment of the external field with respect to the element’s long axis.

Moreover, it was also found that embedded circular elements with a diameter of 10 µm are indeed capable of maintaining a saturated single domain state upon returning to remanence (see Fig. 1h). However, unfortunately this property is lost if the diameter of the element is reduced. Circular elements with a diameter of 2 µm were found to revert to a Landau type flux−closure state upon returning to remanence from saturation. This behavior can most likely be attributed to the higher demagnetizing field of such elements, which roughly scales with $1/d$, where d is the lateral diameter of the element. It thus appears that the longitudinally magnetized rectangular elements depicted in Fig. 1e and f, due to their shape anisotropy, exhibit the highest stability and might therefore be the most promising candidates for magnetic recording applications.

In conclusion, it is found that the magnetic relaxation behavior of embedded ferromagnetic elements is strongly dependent on their geometry. Longitudinally magnetized rectangular geometries

[1] In collaboration with B. Reuscher, A. Brodyanski, M. Kopnarski, Institut für Oberflächen- und Schichtanalytik, Technische Universität Kaiserslautern.

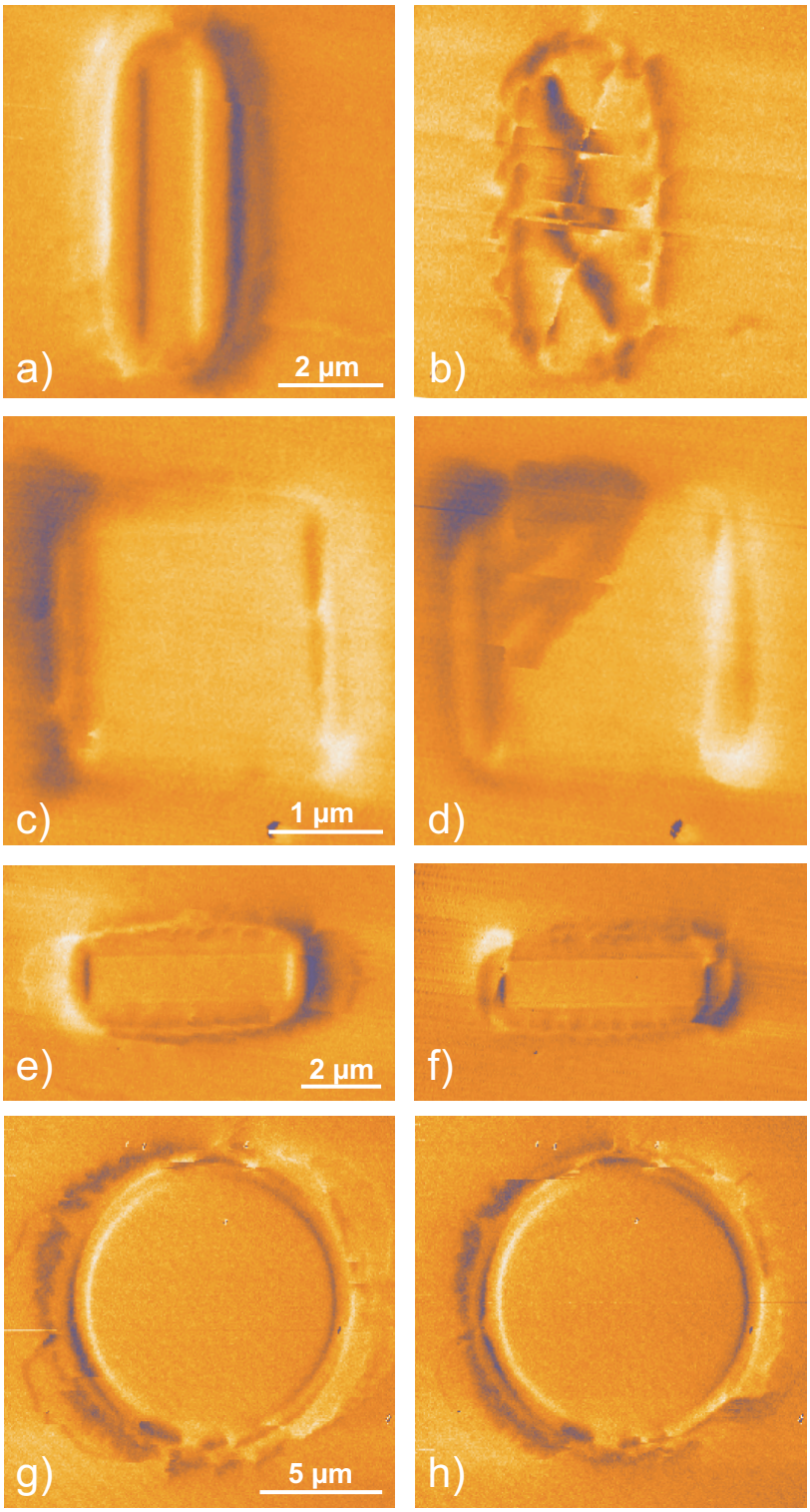

Fig. 1: MFM images of a a) $1 \times 5\,\mu m^2$ rectangular element, c) $2 \times 2\,\mu m^2$ square element, e) $5 \times 1\,\mu m^2$ rectangular element, and g) circular element with a diameter of 10 µm in saturation. The external field is applied in horizontal direction in each case. Panels b), d), f), and h) show corresponding images upon returning to remanence.

indeed appear to be suitable for magnetic data storage applications. However, the previously discussed formation of broad, complex domain walls appearing outside of embedded elements (see Section 6.10 of this report), which leads to inter−element coupling at small inter−element dis-

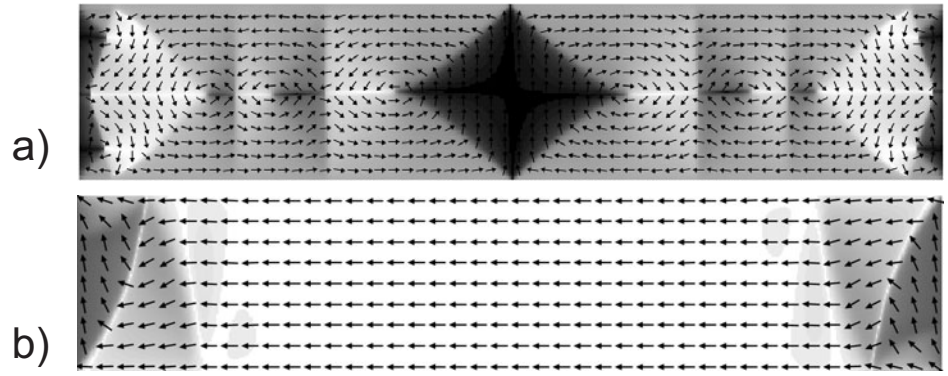

Fig. 2: Numerical simulation of the magnetic configuration of a a) $1 \times 5\,\mu m^2$ or b) $5 \times 1\,\mu m^2$ rectangular, topographically patterned Fe element, upon returning to remanence from a a) transversely or b) longitudinally saturated state. A small field of 3 Oe with an angle of 2° with respect to the long axis of the element shown in panel b) was assumed for the calculation, to simulate a slight misalignment of the external field when returning from a high field value to 0 Oe in the experiment. The dark/bright contrast in panel a) corresponds to up/down orientations of the magnetic moments while in panel b) it corresponds to right/left directions.

tances (see article 6.14), strongly indicates that high areal densities cannot be achieved by this patterning method, which severely limits its applicability for technological purposes.

This work has been accepted for publication in Physical Review B. Support from the Deutsche Forschungsgemeinschaft is gratefully acknowledged.

References

[1] M. Donahue, D.G. Porter, OOMMF v1.1b2 –Object Oriented MicroMagnetic Framework, Software, NIST (2004), available at: http://math.nist.gov/oommf.

6.14 Coupling effects in arrays of embedded ferromagnetic elements

S. Blomeier and B. Hillebrands[1]

The study of small magnetic element arrays has attracted considerable attention in the past, both for fundamental interest and due to their potential application as innovative magnetic data storage devices [1–8]. A detailed understanding of magnetic coupling effects between individual array elements is essential for the future design of such applications. Conventionally, the arrays in question are formed by small ferromagnetic "dots" or "islands", which are topographically separated from each other, i.e. there is no magnetic material in between individual elements. Hence, magnetic coupling effects within arrays of this type are limited to long-range dipolar interactions only. Such dipolar coupling effects have already been observed experimentally [1–6] and modelled theoretically [7, 8]. Moreover, in the particular case of arrays of Fe(110) nanowires on stepped W(110) surfaces, a system was studied which consisted of very thin magnetic elements (between 1.4 and 1.8 monolayer thick) that were surrounded by a 1 monolayer thick pseudomorphic Fe layer [9, 10]. Magnetic coupling effects, leading to antiferromagnetic order, were also observed in this system and were − again − identified to be of dipolar origin, in this case due to a growth−induced rotation of the magnetic easy axis into out−of−plane orientation within the elements [11]. Hence, within these systems the 1 monolayer Fe layer in between the elements did not play a principal role in mediating the observed coupling effects.

In the work presented here we focus our attention on a new type of magnetic array. The arrays studied here consist of exchange−coupled, 20 nm thick elements which are magnetized in−plane and which are completely embedded into a surrounding, continuous film. Fabrication of these elements is described in Section 6.10 of this report. For the experiments discussed in the following, $2 \times 2\,\mu m^2$ square elements were fabricated and were arranged in arrays of 4×4, with different inter−element spacings ranging from 200 nm to 2 µm. Within these arrays, unique inter−element coupling effects were observed in real space, using magnetic force microscopy. In the following, the experimentally obtained results will be discussed, starting with the array with the largest inter−element spacing and then continuously reducing this parameter.

Figure 1 displays magnetic force microscopy (MFM) images of an array of $2 \times 2\,\mu m^2$ elements with an inter−element spacing of 2 µm. It is clearly visible that at this distance the elements are still individual entities both in remanence (Fig. 1a) and in saturation (Fig. 1b). During magnetization reversal of these elements, no particular traces of inter−element coupling can be observed. However, if the spacing between the elements is reduced to 1 µm and below, the situation changes. Figure 2a shows an atomic force microscopy (AFM) image of such an element array, while Fig. 2d displays the corresponding MFM image in remanence. From this image it is clearly observable that the remanent magnetic state of the elements depends on their position within the array. For example, elements at the corners of the array exhibit an almost undisturbed Landau domain configuration similar to the remanent configuration of the elements shown in Fig. 1a. Those elements at the edge of the array, which are not situated at one of the four corners, also exhibit a Landau−type configuration, which in most cases, however, is significantly disturbed. Finally, the central elements within the array show a drastically disturbed remanent magnetic configuration, with the Landau pattern even being broken up in some cases.

[1] In collaboration with B. Reuscher, A. Brodyanski, M. Kopnarski, Institut für Oberflächen- und Schichtanalytik, Technische Universität Kaiserslautern.

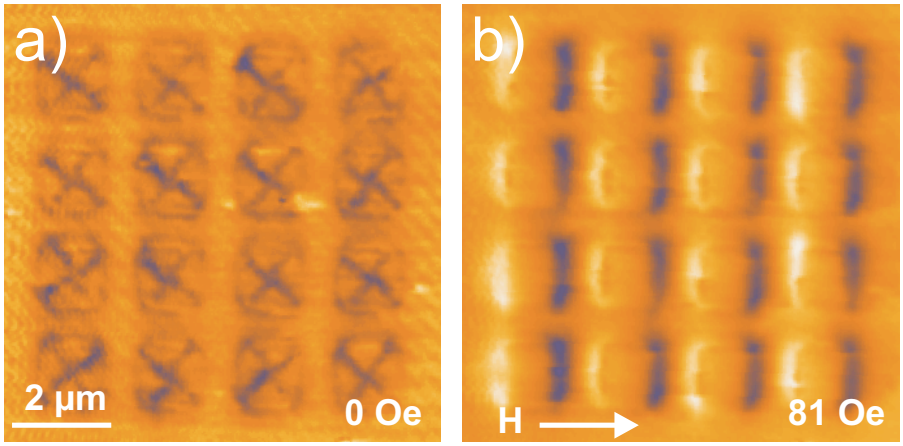

Fig. 1: MFM images of an array of $2 \times 2\,\mu m^2$ embedded Fe elements spaced at an inter−element distance of 2 µm in a) remanence and b) saturation at a field of 81 Oe. The direction of the applied magnetic field is indicated by a white arrow in panel b).

The above findings are a strong indication of inter−element coupling. In particular, central elements are affected most significantly by this coupling, due to the higher number of interacting nearest neighbors within the array, compared to elements at the array edges. Elements at the array corners are affected in the least way, since they only have two such nearest neighbors. Moreover, if an external field is applied (as indicated by the white arrow in Fig. 2g), the magnetic configuration of the corner elements tends to be more stable compared to that of the remaining elements. Furthermore, a saturated single domain state of all elements is reached at a field value of 54 Oe (Fig. 2j), which is noticeably smaller than the saturation field value of 81 Oe for the elements shown in Fig. 1b. These results are consistent with the earlier finding that the saturation field, i.e. the of value the external field which is necessary to saturate an embedded element in a single domain state, is decreasing with increasing lateral element dimensions for square elements of 2 µm and larger sizes (see Section 6.12 of this report). It is believed that the smaller demagnetizing field of larger elements is responsible for this behavior. In particular, if an inter−element coupling exists within an array of such elements, the elements start to behave as a collective entity and thus also exhibit properties of the array as a whole. Hence, also the lateral dimensions of the array should play a role in the magnetization reversal behavior of the elements, and, since the array is significantly larger than the dimensions of an individual element, this should lead to a decrease of their saturation field. Moreover, elements at the array corners should be affected in the least way by this effect. This is exactly what is observed in the experiment.

If the inter−element distance is reduced further down to 500 nm, magnetic coupling effects become even more apparent. Figure 2b shows an array of such elements, while Fig. 2e displays the corresponding MFM image in remanence. It is clearly observable that the array now nearly behaves as a single magnetic entity that exhibits a single large Landau domain structure in remanence. Only some elements at the edge of this array still exhibit individual magnetic properties in the form of smaller Landau configurations, which are superimposed upon the larger structure. Moreover, if an external field of 13 Oe is applied, the larger Landau domain structure starts to change its shape by enlarging the energetically now favorable domain, while the smaller Landau configurations remain stable (Fig. 2h). A similar magnetization reversal process for the smaller Landau structures takes place at higher external field values between 27 Oe and 40 Oe (not shown), when the larger Landau structure has already broken up. Hence, it is possible to study two magnetization reversal processes on two different length scales simultaneously in this system. Again at a field value of 54 Oe, the array has reached a saturated single domain state (Fig. 2k). The magnetic contrast that is still visible within the array in this state has a topographic origin, with the exact mechanism being discussed in Ref. [12].

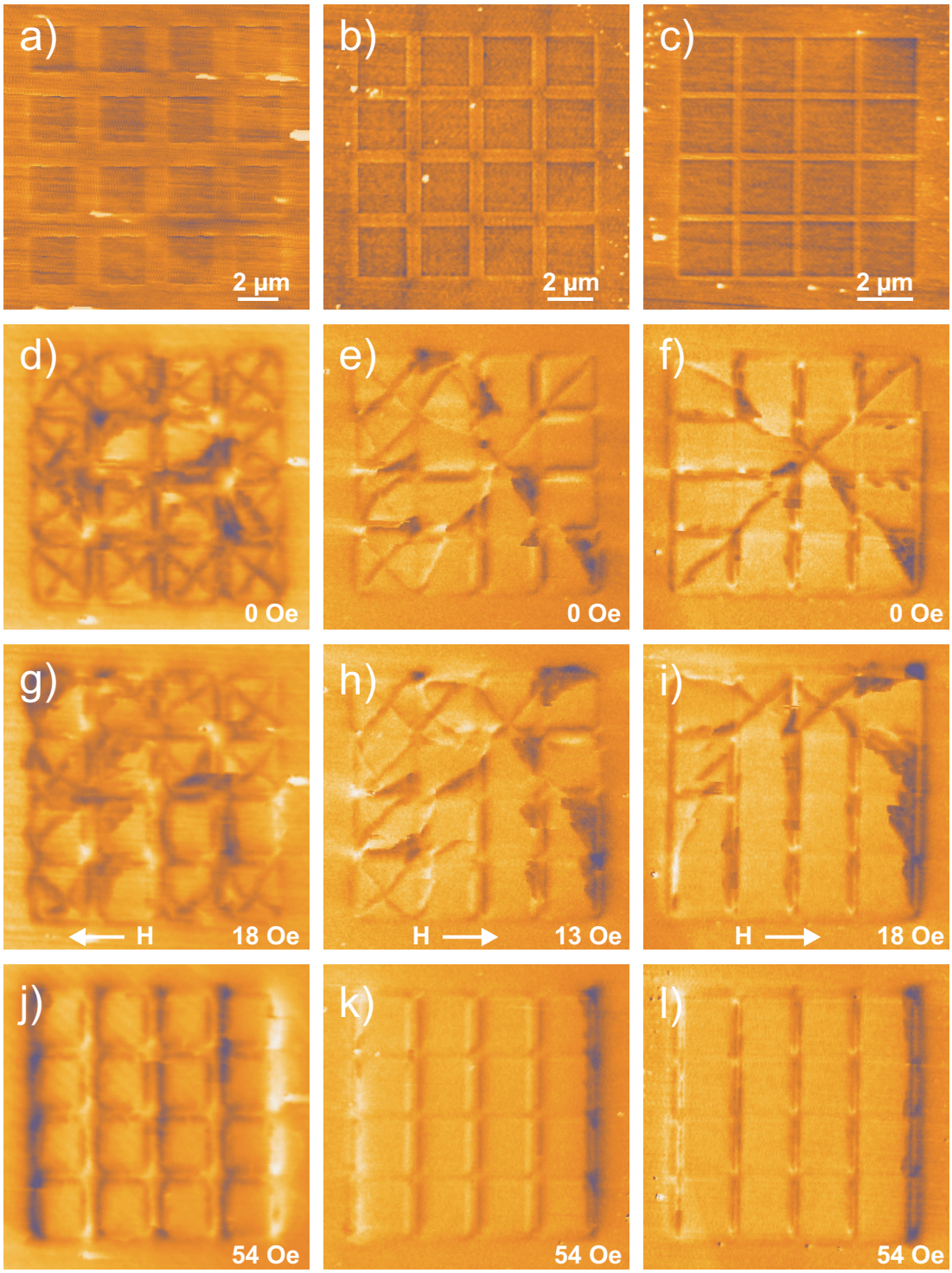

Fig. 2: a)–c) AFM images of arrays of $2 \times 2\,\mu m^2$ embedded Fe elements spaced at distances of a) 1 µm, b) 500 nm, and c) 200 nm. d)–l) Corresponding MFM images d)–f) in remanence, g)–i) at small field values of 13 Oe or 18 Oe as indicated in the panels, and j)–l) in saturation at a larger field value of 54 Oe. Each column corresponds to one array. In each case, the direction of the applied magnetic field is indicated by a white arrow in panels g), h), and i).

At an element separation of 200 nm, the elements do not exhibit individual properties anymore in remanence. Only a single large Landau structure extending over the whole array can be observed now (Fig. 2f). However, at an external field of 18 Oe, when this large Landau structure is in

the process of breaking up, the topmost two edge elements of the array exhibit smaller Landau structures and thus show that the elements still have not completely lost their individual properties (Fig. 2i). Again at a field of 54 Oe, the whole array is in a uniformly magnetized single domain state (Fig. 2l), with some magnetic contrast of topographic origin showing up also here.

The magnetic configurations observed in the arrays studied here suggest that the coupling within this type of system is primarily of exchange and not of dipolar origin. In particular, related studies on arrays of topographically patterned $2 \times 2\,\mu m^2$ square Fe elements of 20 nm thickness and similar inter−element distances did not reveal comparable magnetic configurations [6]. In that type of system, magnetic coupling effects were indeed detected but were rather weak and did not significantly distort the magnetic domain configuration within individual elements even at very close inter−element distances. Due to the topographic separation of the elements, only dipolar interactions can be responsible for the coupling effects observed in Ref. [6]. However, within the system studied here, due to the presence of magnetic material between individual elements, inter−element coupling can indeed be mediated via exchange interaction. Moreover, the drastically different results obtained in our case suggest that exchange interaction is mainly responsible for the observed magnetic coupling effects.

In Section 6.10 of this report it has been shown that complex domain walls must form at the boundary of an embedded element, and it has been demonstrated experimentally that these domain walls form within the antiferromagnetically coupled area immediately outside of a particular element. Moreover, the width of these domain walls has been approximated to be of the order of 500 nm. The lateral range of magnetic coupling effects between closely spaced elements mediated by exchange interaction should be governed by this width. In particular, it can be expected that elements should interact with each other in this way at inter−element distances of twice the wall width, i.e. approximately 1 µm, and below. This is indeed observed in the experiment.

In conclusion, unique magnetic coupling effects were directly observed in arrays of $2 \times 2\,\mu m^2$ Fe elements embedded into an antiferromagnetically coupled Fe/Cr/Fe trilayer. For the first time, inter−element coupling between ferromagnetic elements was observed which is primarily mediated by exchange interaction. With decreasing inter−element distance, a transition from an individual towards a collective behavior of the array elements is found. The lateral range of these coupling effects is governed by the width of domain walls forming immediately outside of individual elements.

This work has been submitted to Physical Review Letters. Support from the Deutsche Forschungsgemeinschaft is gratefully acknowledged.

References

[1] T. Aign, P. Meyer, S. Lemerle, J.P. Jamet, J. Ferré, V. Mathet, C. Chappert, J. Gierak, C. Vieu, F. Rousseaux, H. Launois, H. Bernas, Phys. Rev. Lett. **81**, 5656 (1998).

[2] C. Mathieu, C. Hartmann, M. Bauer, O. Buettner, S. Riedling, B.F.P. Roos, S.O. Demokritov, B. Hillebrands, B. Bartenlian, C. Chappert, D. Decanini, F. Rousseaux, E. Cambril, A. Müller, B. Hoffmann, U. Hartmann, Appl. Phys. Lett. **70**, 2912 (1997).

[3] Y.B. Xu, A. Hirohata, L. Lopez-Diaz, H.T. Leung, M. Tselepi, S.M. Gardiner, W.Y. Lee, J.A.C. Bland, F. Rousseaux, E. Cambril, H. Launois, et al., J. Appl. Phys. **87**, 7019 (2000).

[4] J. Jorzick, C. Krämer, S.O. Demokritov, B. Hillebrands, E. Sondergard, M. Bailleul, C. Fermon, U. Memmert, A.N. Müller, A. Kounga, U. Hartmann, E. Tsymbal, J. Magn. Magn. Mater. **226-230**,1835 (2001).

[5] R. Hyndman, A. Mougin, L.C. Sampaio, J. Ferré, J.P. Jamet, P. Meyer, V. Mathet, C. Chappert, D. Mailly, J. Gierak, J. Magn. Magn. Mater. **240**, 34 (2002).

[6] M. Bolte, R. Eiselt, G. Meier, D.-H. Kim, P. Fischer, J. Appl. Phys. **99**, 08H301 (2006).

[7] R.L. Stamps, R.E. Camley, Phys. Rev. B **60**, 11694 (1999).
[8] L.F. Zhang, C. Xu, P.M. Hui, Y.Q. Ma, J. Appl. Phys. **97**, 103912 (2005).
[9] J. Hauschild, U. Gradmann, H.J. Elmers, Appl. Phys. Lett. **72**, 3211 (1998).
[10] O. Pietzsch, A. Kubetzka, M. Bode, R. Wiesendanger, Phys. Rev. Lett. **84**, 5212 (2000).
[11] N. Weber, K. Wagner, H.J. Elmers, J. Hauschild, U. Gradmann, Phys. Rev. B **55**, 14121 (1997).
[12] S. Blomeier, P. Candeloro, B. Hillebrands, B. Reuscher, A. Brodyanski, M. Kopnarski, Phys. Rev. B, in press.

6.15 Structural effects of keV ion irradiation of Fe/Cr/Fe trilayers

S. Blomeier and B. Hillebrands[1]

Experimental investigations of embedded ferromagnetic elements by magnetic force microscopy (see Sections 6.10 −6.14) indicate that these elements exhibit a high degree of magnetic order even though the corresponding areas of the respective Fe/Cr/Fe trilayers have been exposed to rather high ion fluences of 30 keV Ga^+-ions. This finding is further confirmed by Kerr magnetometry measurements from a $1 \times 1\,\mathrm{mm}^2$ area which has been exposed to a fluence of $2.7 \cdot 10^{16}\,\mathrm{ions/cm}^2$. Figure 1 shows magnetization curves (black lines) which have been recorded from this area while the external field was applied along a) an easy axis or b) a hard axis direction, respectively. In addition, respective magnetization curves recorded from an epitaxial, 20 nm thick Fe layer are also shown for comparison (gray lines). The latter sample was grown in exactly the same way as the Fe/Cr/Fe trilayers normally studied, except that the Cr interlayer was omitted.

It can be seen from Fig. 1 that the shape of the respective curves is very similar in both cases, indicating that the irradiated area nearly exhibits the same properties as an as−prepared epitaxial Fe layer (see also [1–3] for magnetization curves of epitaxial Fe samples). While an increased easy axis coercivity of ≈ 13 Oe (compared to ≈ 6 Oe of the Fe layer) and a reduced anisotropy can be observed in the curves from the irradiated area in comparison to the reference system, the results displayed in Fig. 1 strongly indicate that the irradiated area still exhibits a high degree of crystalline order after ion bombardment.

These results could also be confirmed directly by high resolution transmission electron microscopy (HRTEM) measurements from a cross−sectional area of a trilayer which had been irradiated by a rather high ion fluence of $5 \cdot 10^{16}\,\mathrm{ions/cm}^2$. Figure 2a displays one of the images recorded during this measurement process.

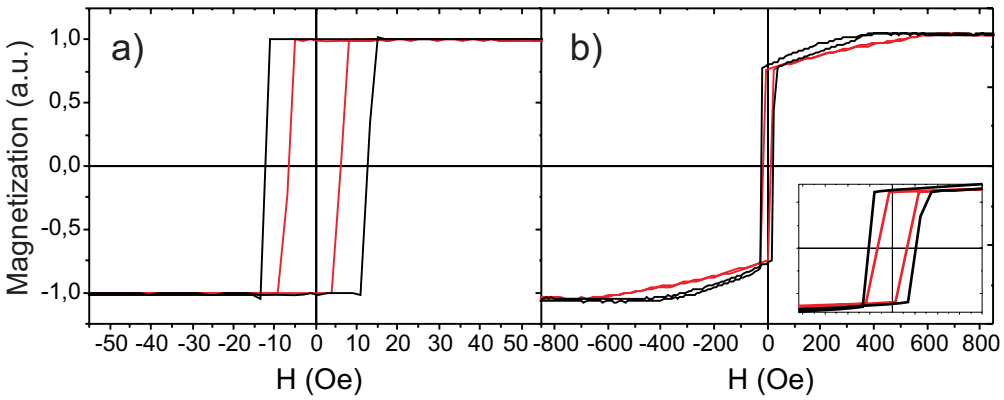

Fig. 1: Kerr magnetometry measurements of an Fe/Cr/Fe trilayer which has been exposed to a fluence of $2.7 \cdot 10^{16}\,\mathrm{ions/cm}^2$ within a $1 \times 1\,\mathrm{mm}^2$ area. The panels display magnetization curves recorded from the irradiated area (black) as well as reference measurements from a non−irradiated sample which did not contain a Cr interlayer (gray). a) Easy axis measurement. b) Hard axis measurement. An inset shows the central field region in an interval between −80 Oe and 80 Oe in a magnified view.

[1] In collaboration with B. Reuscher, A. Brodyanski, M. Kopnarski, Institut für Oberflächen- und Schichtanalytik, Technische Universität Kaiserslautern, V.E. Demidov and S.O. Demokritov, Institut für Angewandte Physik, Universität Münster, and H.M. Urbassek, Fachbereich Physik, Technische Universität Kaiserslautern.

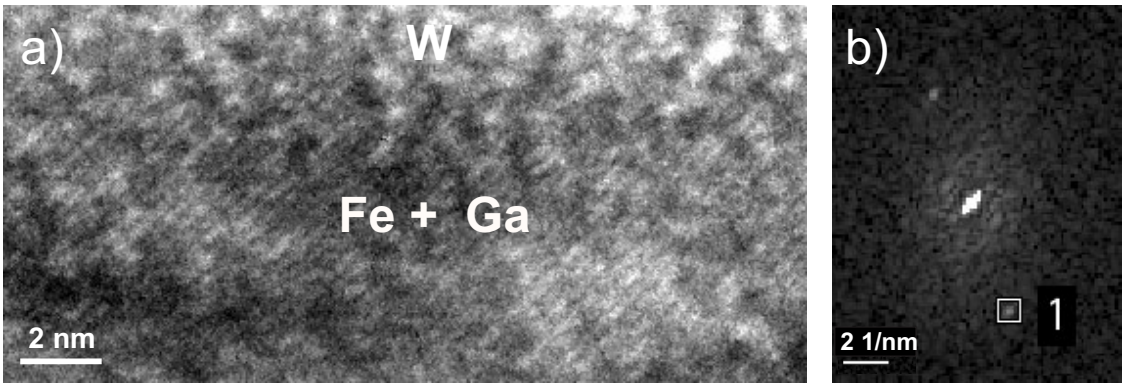

Fig. 2: a) HRTEM image of the crystal structure of an Fe/Cr/Fe trilayer which has been irradiated by a fluence of $5 \cdot 10^{16}\,\mathrm{ions/cm^2}$. The image primarily shows the upper Fe layer. b) Diffractogram of the spatial frequencies of the image displayed in panel a).

A pattern of diagonally oriented crystal planes can clearly be observed in the central and lower part of Fig. 2 a), while the upper part of this image shows an overlayer mainly consisting of tungsten. This overlayer is deposited onto the sample for technical reasons during the preparation process of the cross−tie specimen. Figure 2b displays a diffractogram of the spatial frequencies contained in the image shown by panel a). By means of the two clearly visible satellite peaks within this diffractogram the crystal planes depicted in a) can be identified to be the (110)-planes of a cubic lattice with lattice constant $a = 2.87\,\text{Å}$, which is a typical value for a bcc Fe lattice. It is directly observable from this image that the crystal lattice of the irradiated trilayer still exhibits a high degree of structural order even though it has been exposed to a rather high ion fluence of $5 \cdot 10^{16}\,\mathrm{ions/cm^2}$.

In addition to the TEM investigations discussed above, energy dispersive x−ray analysis (EDX) measurements were carried out on the same cross−tie specimen. These measurements provide information on the stoichiometry of the investigated sample. It was obtained that the ratio of implanted Ga^+−ions with respect to the total number of atoms in the depth region of the trilayer is equal to approximately 15%. At a first glance, the simultaneous observation of a high degree of crystalline order and this high amount of implanted ions is an amazing result. In order to investigate this phenomenon further, **S**topping and **R**ange of **I**ons in **M**atter (SRIM) [4, 5] simulations of the irradiation process studied here were performed. Figure 3 shows a typical result of these simulations in the form of a single trajectory of a 30 keV Ga^+−ion upon perpendicular incidence onto an Fe/Cr/Fe trilayer system.

The position where the incoming ion enters the target material is marked by a gray arrow in Fig. 3. Three distinctive areas around the subsequent trajectory (marked by “1” −“3”) can be observed, where so−called “nuclear collision cascades” are forming. These cascades are initiated by inelastic scattering processes of the ion with so−called “primary knock−on atoms”. These atoms gain enough energy that they are knocked out of their original lattice positions and can then themselves undergo scattering processes with other target atoms. If the initially deposited energy is high enough, this process can repeat itself a number of times, until a large number of atoms within a certain finite volume in the vicinity of the ion trajectory is in motion, forming the aforementioned collision cascade. As it has been shown in [6], the deposited energy Θ_D per target atom within the volume of such a cascade can be approximated by means of a straightforward, but efficient model. This approximation will be carried out in the following for the case of the irradiation of an

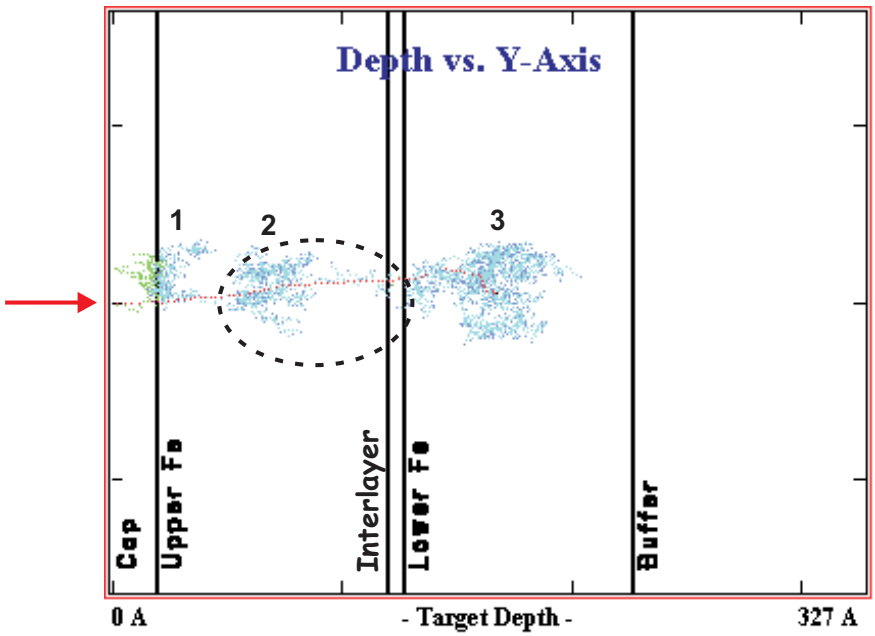

Fig. 3: SRIM simulation of the trajectory of a single 30 keV Ga^+−ion upon perpendicular incidence onto the investigated Fe/Cr/Fe trilayer system. The image also displays target atoms which have been knocked out of their original lattice positions in the process of nuclear collision cascades. The dashed ellipse is discussed in the body of the text.

Fe target by 30 keV Ga^+−ions, which is a good approximation of the experimentally investigated irradiation of Fe/Cr/Fe trilayers.

An ion entering a solid primarily loses its kinetic energy via two different mechanisms, which are electronic and nuclear scattering processes. SRIM simulations show that nuclear scattering processes account for more than 80 % of an incoming ion's energy losses in the case of the irradiation of an Fe target with keV Ga^+−ions. Hence, at least 24 keV of the energy of a 30 keV Ga^+−ion are deposited via nuclear collision cascades into the target material. Moreover, as it has been shown in [6], the energy Θ_D per target atom deposited through such nuclear scattering processes can be described by Gaussian distributions in all three spatial directions in first approximation. Hence, an ellipsoidal volume whose half axes are equal to the standard deviations of these distributions should contain $(68\%)^3 = 0.68^3 \approx 0.32 = 32\%$ of this energy. The average depth of the deposited energy density $< X >$ as well as the aforementioned standard deviations $\sqrt{< \Delta X^2 >}$ and $\sqrt{< Y^2 >}$ in normal direction and in the two in-plane directions of the sample, respectively, can be calculated from the average penetration depth R of the ions as well as from the mass ratio between target atoms and incoming ions.

In the case of the irradiation of an Fe target with 30 keV Ga^+−ions, the values $R \approx 11$ nm and $M_{Fe}/M_{Ga} \approx 0.8$ result in $< X > \approx 6.9$ nm, $< \Delta X^2 > \approx 17.4\,\text{nm}^2$ as well as $< Y^2 > \approx 7.3\,\text{nm}^2$. An ellipsoid of these dimensions has been drawn to scale into Fig. 3, to better illustrate this result. Moreover, its volume V_{ell} can be calculated according to the usual relation

$$V_{ell} = \frac{4}{3}\pi\sqrt{< \Delta X^2 >}< Y^2 > \quad . \tag{1}$$

Up to now it was assumed that the energy is transferred in a spatially homogeneous way to the lattice of the target. However, it can be seen from Fig.3 that the individual cascades, where energy

deposition takes place, are localized within a volume which is significantly smaller than that of the previously calculated ellipsoid. Therefore, a dimensionless correction factor $\delta^3_{\mathrm{corr}} < 1$, which also depends on the mass ratio between incoming ions and target atoms [6], must be multiplied with V_{ell}, in order to obtain a more realistic approximation of the volume of an individual cascade. In the case studied here ($M_{\mathrm{Fe}}/M_{\mathrm{Ga}} \approx 0.8$), this correction factor is equal to ≈ 0.39.

From these values, the deposited energy Θ_{D} per target atom can be calculated according to

$$\Theta_{\mathrm{D}} = \frac{0.32 \cdot \nu(E)}{N \delta^3_{\mathrm{corr}} V_{\mathrm{ell}}} \quad , \tag{2}$$

where $\nu(E) = 24\,\mathrm{keV}$ is the ratio of the ionic energy that is deposited via nuclear scattering processes and N denotes the density of the target. Inserting the previously calculated values into Eq. 2, one obtains a result of $\Theta_{\mathrm{D}} \approx 1.83\,\mathrm{eV/atom}$

It is instructive to compare the above value with the energy Θ_{melt} per atom which is necessary to melt Fe, starting from room temperature ($= T_0$). It is well known that this parameter can be calculated according to

$$\Theta_{\mathrm{melt}} = \int_{T_0}^{T_{\mathrm{melt}}} c_{\mathrm{V}}(T) dT + \Delta H_{\mathrm{melt}} \quad , \tag{3}$$

where T_{melt}, $c_{\mathrm{V}}(T)$, and ΔH_{melt} are the melting temperature, the specific heat, and the heat of fusion of Fe, respectively. While the specific heat is, according to Dulong−Petit's law, equal to $3k_{\mathrm{B}}$, the heat of fusion can be approximated by means of the so−called "Richards rule" (see, e.g. [7]) to be equal to $k_{\mathrm{B}}T_{\mathrm{melt}}$. A melting temperature of 1811 K therefore yields a result of $\Theta_{\mathrm{melt}} \approx 0.55\,\mathrm{eV/atom}$.

According to the above considerations, the important result is obtained that the average energy Θ_{D} per atom deposited via nuclear scattering processes is more than three times larger than the melting energy Θ_{melt} of Fe. Despite the approximative character of these considerations it can therefore be concluded that the irradiation processes studied here lead to a quasi instantaneous melting of the bombarded material within certain areas around the trajectories of the incoming ions. Hence, a large amount of irradiation−induced defects can be healed out during subsequent cooling and re−crystallization processes. Furthermore, the implanted Ga^+−ions can easily be integrated into the lattice of the target, as both Ga and the target material Fe are metals.

Moreover, from other experimental investigations it is known that the implantation of Ga into bcc Fe leads to a linear increase of the lattice constant a of the target material if the ratio of implanted atoms is small [8]. In particular, a ratio of $\approx 12\%$ (which is similar to the value of $\approx 15\%$ measured by EDX after irradiation with a fluence of $5 \cdot 10^{16}\,\mathrm{ions/cm^2}$) results in a lattice constant of $a = 2.89\,\text{Å}$, which is equal to $a_{\mathrm{Ag}}/\sqrt{2}$, where a_{Ag} is the lattice constant of the buffer material Ag. Hence, the irradiation of Fe/Cr/Fe trilayers with 30 keV Ga^+−ions in the low and medium $10^{16}\,\mathrm{ions/cm^2}$ fluence range leads to a reduction of the lattice mismatch to the Ag buffer layer of the system and therefore to an *improvement* of the conditions for the formation of highly epitaxial lattice structures.

Taking the above arguments into account, it becomes reasonable that the investigated trilayers still exhibit a highly ordered crystalline structure (and therefore also a pronounced magnetocrystalline anisotropy) even after irradiation with rather high fluences of keV Ga^+−ions. However, the phase diagram on the alloy formation of Fe and Ga (see, e.g., [8]) indicates that with further increasing

ion fluences (i.e. further increasing ratio of implanted ions) a structural phase transition of the form $Fe \rightarrow Fe_3Ga$ should take place, with the transition being complete at an amount of 25% implanted Ga. Previous experiments on the fluence dependence of the surface topography of bombarded areas indeed strongly indicated the occurrence of such a phase transition [9]. The most important results of these investigations are summarized in Fig. 4.

Figure 4a and b show two atomic force microscopy (AFM) images that were taken from the boundary region of irradiated $20 \times 20\,\mu m^2$ square areas. The left half of each image shows an area that was irradiated with a fluence of a) $2.7 \cdot 10^{16}\,ions/cm^2$ and b) $6.25 \cdot 10^{16}\,ions/cm^2$ of 30 keV Ga^+-ions, while the right half was left non−irradiated. It is clearly observable that the surface structure of the area irradiated with the higher ion fluence is noticeably different from its corresponding non−irradiated part, while there is a far smaller difference between irradiated and non−irradiated surface in the case of the lower fluence. In particular, the surface roughness of the highly irradiated area is drastically increased with respect to the non−irradiated area. This behavior can also be observed in the fluence dependence of the root mean square (rms) roughness of the bombarded surface, which is shown in Fig. 4c.

While the rms roughness increases monotonically, but rather moderately with increasing ion fluence for fluences $\leq 5 \cdot 10^{16}\,ions/cm^2$, a sudden jump by more than 500% can be observed if the fluence is further increased to $6.25 \cdot 10^{16}\,ions/cm^2$, which confirms previous observations. These findings are a strong indication of a structural phase transition. Extrapolating the 15% ratio of

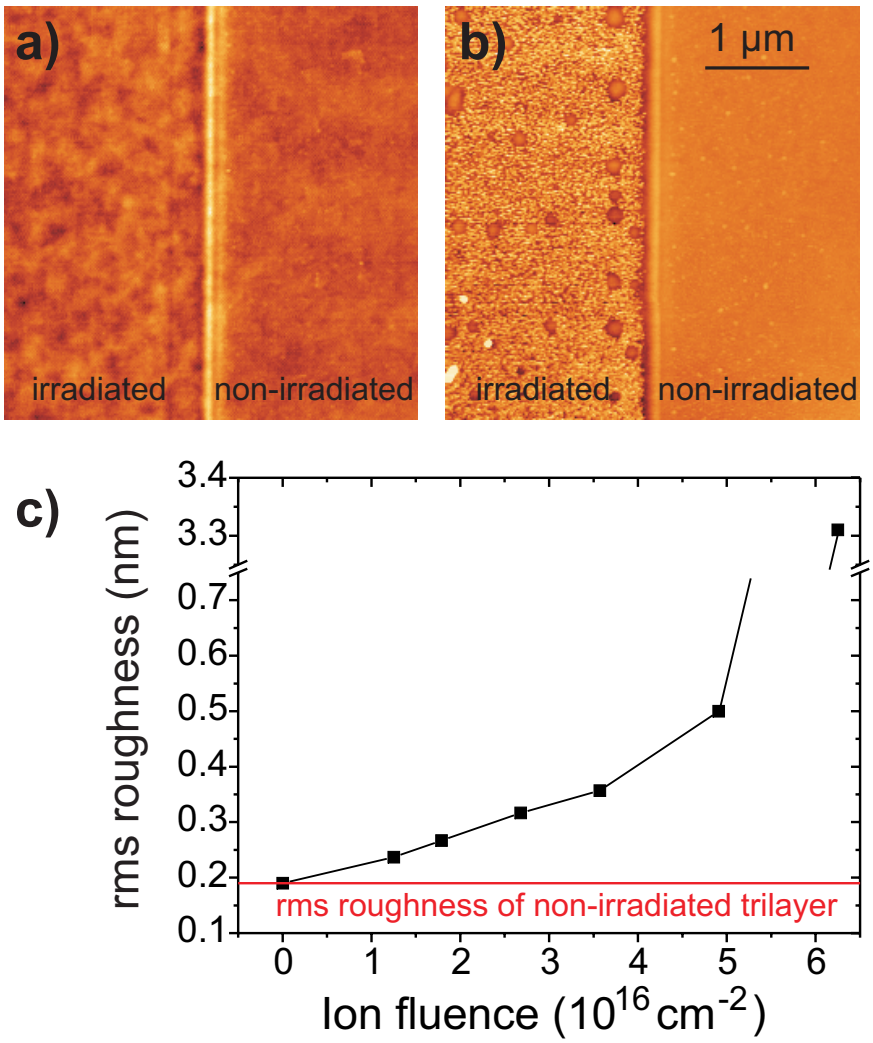

Fig. 4: AFM images of the boundary region of irradiated $20 \times 20\,\mu m^2$ square areas. The left half of each image shows an area that was irradiated with a fluence of a) $2.7 \cdot 10^{16}\,ions/cm^2$ and b) $6.25 \cdot 10^{16}\,ions/cm^2$ of 30 keV Ga^+-ions, while the right half was left non−irradiated. c) Fluence dependence of the rms roughness of the bombarded surfaces. The rms roughness of the non−irradiated trilayer is also shown for reference purposes as a gray line.

implanted Ga^+-ions at a fluence of $5 \cdot 10^{16}\,\mathrm{ions/cm^2}$ measured by EDX, it is obtained that this transition takes place at a ratio of $\approx 20\%$ implanted ions.

Moreover, at a high fluence of $6.25 \cdot 10^{16}\,\mathrm{ions/cm^2}$, no magnetic domain structures could be observed anymore by means of magnetic force microscopy within the irradiated areas. While it is known that Fe_3Ga exhibits ferromagnetic properties in an ordered state (Curie temperature of $\approx 740\,\mathrm{K}$ [10]), it does not form a bcc lattice, but an fcc$-$type $L1_2$ structure with a lattice constant of $a' = 5.8\,\text{Å}$ [8,11]. It is therefore reasonable to assume that this difference in crystallographic structure is the origin of the observed structural phase transition, which is also most likely responsible for the observed break$-$down of the magnetic order on the micrometer scale.

In conclusion, it has been demonstrated that the irradiation of epitaxial Fe/Cr/Fe trilayers with fluences of $\leq 5 \cdot 10^{16}\,\mathrm{ions/cm^2}$ of 30 keV Ga^+-ions largely preserves the high degree of structural order of the target material. The obtained results provide insight into why a local irradiation of this material system with Ga^+-ions is such an efficient method to fabricate highly ordered magnetic microstructures. Moreover, experimental evidence was obtained indicating the occurrence of a structural phase transition of the form $Fe \rightarrow Fe_3Ga$ at higher fluences. Further experiments by means of secondary ion mass spectroscopy depth profiling are planned in the near future to verify these findings. In addition, the above discussion has shown that the irradiation of Fe/Cr/Fe trilayers with 30 keV Ga^+-ions cannot be understood in terms of simple ballistic scattering models. Rather than that, quasi instantaneous melting and re$-$crystallization processes as well as implantation effects also play a crucial role in the irradiation$-$induced modification of the target material. These findings qualitatively agree with results of Rettner et al., who studied the ion beam induced intermixing of CoPt multilayers with 30 keV Ga^+-ions [12].

This work will be part of an upcoming publication. Support from the Deutsche Forschungsgemeinschaft and from the EU Marie Curie Research Training Network MRTN-CT-2003-504462 ULTRASMOOTH is gratefully acknowledged.

References

[1] J.M. Florczak, E.D. Dahlberg, Phys. Rev. B **44**, 9338 (1991).
[2] E. Gu, J.A.C. Bland, C. Daboo, M. Gester, L.M. Brown, R. Ploessl, J.N. Chapman, Phys. Rev. B **51**, 3596 (1995).
[3] Y.B. Xu, E.T.M. Kernohan, M. Tselepi, J.A.C. Bland, S. Holmes, Appl. Phys. Lett. **73**, 399 (1998).
[4] J.F. Ziegler, J.F. Biersack, J.P. Littmark: *The Stopping and Range of Ions in Solids*. Pergamon, New York, (1985).
[5] J.F. Ziegler: *Documentation of the SRIM code, www.srim.org*, (2003).
[6] M. Nastasi, J.W. Mayer, J.K. Hirvonen: *Ion-Solid Interactions: Fundamentals and Applications*. Cambridge University Press (1996).
[7] R.A. Swalin: *Thermodynamics of Solids*. John Wiley, New York (1976).
[8] B. Predel: *Landolt-Börnstein / New Series. Numerical Data and Functional Relationships in Science and Technology, Group IV, Vol.5: Macroscopic Properties of Matter. Phase Equilibria, Crystallographic and Thermodynamic Data of Binary Alloys, Subvolume E*. Springer, Berlin$-$Heidelberg$-$New York, (1995).
[9] S. Blomeier, B. Hillebrands, V.E. Demidov, S.O. Demokritov, B. Reuscher, A. Brodyanski, M. Kopnarski, J. Appl. Phys. **98**, 093503 (2005).
[10] N. Kawamiya, Y. Nishino, M. Matsuo, S. Asano, Phys. Rev. B **44**, 12406 (1991).
[11] W. Köster, T. Gödecke, Z. Metallkde. **68**, 582-589 and 661-666 (1977).
[12] C.T. Rettner, S. Anders, J.E.E. Baglin, T. Thomson, B.D. Terris, Appl. Phys. Lett. **80**, 279 (2002).

6.16 Photo-induced modulation of the interlayer exchange coupling in a magnetic trilayer on the picosecond time scale

S. Blomeier, M.C. Weber, J. Hamrle, and B. Hillebrands

The influence of ultrashort laser pulses on the magnetic properties of thin film systems has attracted considerable interest in recent years. Experimental investigations of thin Ni films employing all−optical pump−probe techniques provided insight into the dynamics of the electron and spin systems of a single magnetic layer on an ultrashort time scale [1, 2]. Moreover, Ju et al. have shown that the interface exchange coupling in exchange bias bilayers consisting of a ferromagnetic (F) and an adjacent antiferromagnetic (AF) layer can be modulated on the picosecond time scale through exposure to ultrashort laser pulses [3]. In the latter case, a reduction in the exchange coupling upon photo−excitation was observed, which was attributed to an optically induced thermal "unpinning" of interfacial spins at the F/AF interface. Moreover, following this ultrafast unpinning, a slower recovery of the magnetic properties of the system, in particular the exchange bias field H_{ex}, was observed [3, 4].

In the work presented here, we provide experimental evidence that it is also possible to modulate the interlayer exchange coupling in a magnetic trilayer on the picosecond time scale by means of an all−optical pump−probe technique. For the purpose of our studies, an epitaxial, antiferromagnetically coupled (10 nm Fe / 0.7 nm Cr / 10 nm Fe) trilayer was grown by electron beam evaporation, using a UHV system with a base pressure of less than $5 \cdot 10^{-10}$ mbar. The sample was grown onto a MgO(100) substrate covered by a 1 nm thick Fe seed layer and a 125 nm thick Ag buffer layer, and it was covered by a 2 nm thick Cr cap layer to prevent it from oxidation. The exact growth procedure is described elsewhere in more detail [5]. This material system was considered to be particularly well−suited for our experiments as it has been the subject of extensive research activities in the past two decades and is therefore well characterized (see, e.g., Ref. [6]).

For the pump−probe experiments, the second harmonic of a high power SESAM mode−locked diode pumped Nd:YVO_4 IR laser oscillator with a repetition rate of 80 MHz and a wavelength of 1064 nm was used. Pulse−picked 8 ps short laser pulses with a central wavelength of 532 nm and a repetition rate of 1 MHz were divided into an intense pump beam and a much weaker probe beam by a beam splitter. Time delay between pump and probe beam was achieved by means of a translation stage, allowing for a variable pump−probe delay interval from −400 ps (i.e. the probe pulse arrives before the pump pulse) up to 6 ns. The excitation density of the intense pump pulses on the sample surface was $2.3\,\mathrm{mJ/cm^2}$. The magnetic properties of the investigated sample as a function of the pump−probe delay time were detected by means of the longitudinal magneto−optical Kerr effect (MOKE), with all measurements being carried out in easy−axis geometry (using a field−sweep rate of approximately 30 Oe/s). More details of this setup can be found in Ref. [7].

Figure 1 shows a typical magnetization curve that was recorded while the pump beam was blocked (this situation was found to be identical to pump−probe processes with negative delay times). A hysteresis loop which is characteristic for an antiferromagnetically coupled trilayer system is displayed. Small arrows indicate the orientations of the magnetizations of the two ferromagnetic Fe layers. At zero external field, both magnetizations are aligned antiparallel in consequence of the antiferromagnetic coupling, resulting in a zero net magnetic moment in remanence. With increasing field, they gradually rotate towards each other, which leads to an increase of the net magnetic moment. It can be seen from Fig. 1 that this rotation is not yet complete at the maximum field value of 2000 Oe that was achievable with our setup.

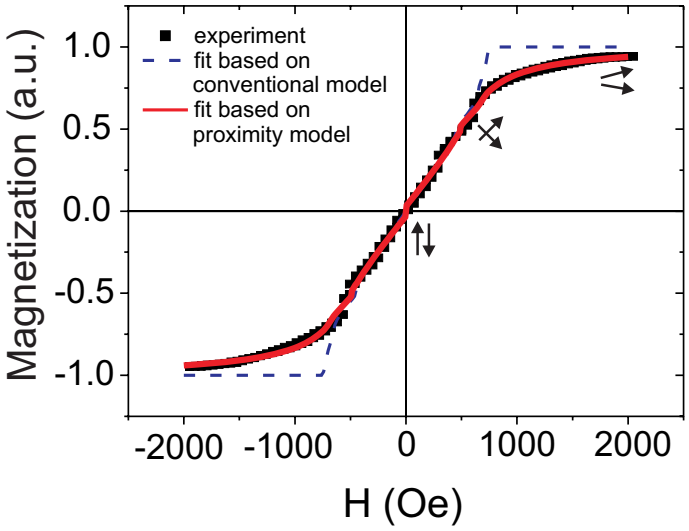

Fig. 1: Magnetization curve recorded from the sample while the pump beam was blocked. A fit based on the conventional model given by Eq. 1 is represented by a dashed line ($J_1 = -0.8\,\mathrm{mJ/m^2}$, $J_2 = -0.16\,\mathrm{mJ/m^2}$), while a fit based on the proximity magnetism model given by Eq. 2 is represented by a solid line line (C_+ = 0.01, C_- = 0.3). Small black arrows indicate the orientations of the magnetizations of the two Fe layers.

Interlayer exchange coupled trilayer systems are usually described by an areal energy density ansatz (see, e.g., Ref. [8]) which is of the form

$$E = -J_1 \cos(\varphi) - J_2 \cos^2(\varphi) \quad . \tag{1}$$

Here, E denotes the interfacial areal energy density of the trilayer system, while φ represents the angle between the magnetizations of the two ferromagnetic layers. J_1 and J_2 are the so−called "bilinear" and "biquadratic" coupling constants which characterize the nature of the interlayer exchange coupling for a given material system. The physical model underlying Eq. 1 is the so−called "quantum well model" [8]. Interlayer exchange coupling in the framework of this model is mediated by conduction electrons within the interlayer and originates from spin−dependent confinement of these electrons. A fit based on Eq. 1 is shown as a dashed line in Fig. 1. It can be seen that for field values up to about 600 Oe, the fit can reproduce the experimental data well, while considerable discrepancies for higher field values occur. In particular, whilst the net magnetization reaches a saturation value in an abrupt manner in the fit model, saturation in the experiment is reached asymptotically.

It has been predicted by Slonczewski that such an asymptotic behavior should occur in the case of magnetic trilayer systems with interlayers consisting of an antiferromagnetic material and exhibiting negligible interfacial roughness [9]. In this case, an alternative model for the interlayer exchange coupling energy density was proposed, which is of the form

$$E = C_+ \varphi^2 + C_- (\pi - \varphi)^2 \tag{2}$$

and which we will refer to as the so−called "proximity magnetism model" in the following. Again, E and φ denote the interfacial areal energy density of the trilayer system and the angle between the magnetizations of the two ferromagnetic layers. Similar to Eq. 1, C_+ and C_- are two adjustable parameters which characterize the nature of the coupling. In particular, for $C_+ \approx 0$ and $C_- > 0$, Eq. 2 describes an antiferromagnetically coupled trilayer.

It is known from detailed experimental studies that the magnetic properties of ultrathin epitaxial Cr layers of a few nanometer thickness, which are in proximity to adjacent Fe layers, can be described by a commensurate spin−density wave (see, e.g. Ref. [10]), i.e., they exhibit an antiferromagnetic order. Hence, the magnetic properties of interlayer exchange coupled Fe/Cr/Fe trilayers with smooth interfaces are better described by Eq. 2 than by the conventional quantum well coupling model given by Eq. 1 at small interlayer thicknesses. Experimental investigations by Kreines et al. indeed confirm these considerations [11]. A fit based on Eq. 2 is shown as a solid line in Fig. 1. The fit reproduces the experimental data in an excellent way for the complete range of the external field. In particular, the saturation regions are also well reproduced. The proximity magnetism model is thus shown to be much better suited to describe the magnetic properties of our sample than the conventional coupling model. However, this does not imply that the proximity magnetism mechanism is the only contribution to the interlayer exchange coupling in our system. In particular, the aforementioned electronic contribution to the coupling due to the quantum well mechanism is an intrinsic property of all interlayer exchange coupled systems and is therefore also present in our system; it is merely superposed by a stronger, dominant coupling mechanism.

According to preliminary estimations based on real−time measurements of the spin temperature dynamics in metallic exchange bias bilayers [7], the exposure of our sample to the pump pulses of our setup should result in a fast increase of the electron and spin temperature in the laser spot region by up to approximately 100 K, after a thermalization process between both systems has taken place on a sub−ps time scale. Conventional static MOKE measurements performed at stationary sample temperatures between room temperature and 373 K indicated that an increase in temperature within this interval leads to a change of the magnetization curves of our sample. Moreover, the most notable thermally induced changes to the magnetization curves were found to occur in the saturation regions of the curves and were rather small, compared to the large field range of −2000 Oe to 2000 Oe. Prior to the pump−probe experiments, it was also checked that the setup used for the magnetometry measurements was stable enough against minor fluctuations of the magneto−optical signal, due to the expected smallness of the effect. It turned out that magnetization curves are reproduced very accurately and that such fluctuations can be ruled out as a source of error.

Figure 2 shows examples of magnetization curves recorded at different pump−probe delay times. In panel (a), three magnetization curves at negative delay (black) and at delay times of 6 ps, i.e., within the autocorrelation width of the pump pulse (dark gray), and 1550 ps (light gray). In panel (b), the magnified positive saturation region marked by a black box in panel (a) is depicted. Although the three magnetization curves appear to be identical at a first glance [see Fig. 2 (a)], it is evident from panel (b) that the magnetization curve of the system slightly but noticeably changes its shape for small delay times, but relaxes back to its original form at negative delay in a very reproducible manner in the case of long delay times. It should be emphasized that the observed changes for small delay times are not due to fluctuations of the magneto−optical signal and can be reproduced very accurately and consistently. Moreover, it can also be expected that so-called “bleaching effects” do not disturb the measurement signal. These effects originate from a massive spin-polarized re-population of electronic states as a result of the optical excitation, leading to an additional non-magnetic contribution to the Kerr signal. In particular, it has been found in epitaxial Ni layers of comparable thickness that such processes take place on a time scale < 2 ps [12], and should therefore not be resolveable within our experiment (which has a minimum delay time of 6 ps). Furthermore, for each delay time, the curves depicted in panel (a) can be fitted as accurately as the curve displayed in Fig. 1, using the fit model based on Eq. 2.

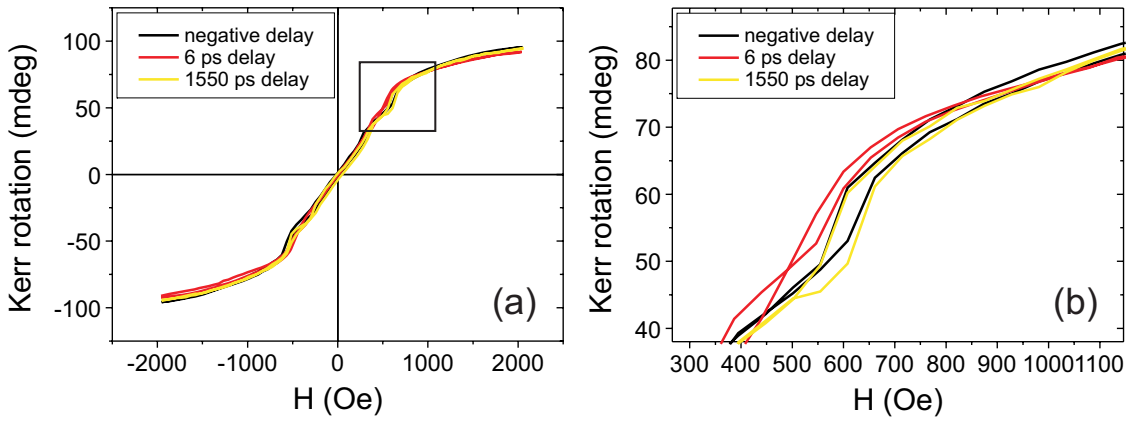

Fig. 2: a) Magnetization curves recorded at different delay times. The curves correspond to negative delay (black), or delay times of 6 ps (dark gray) and 1550 ps (light gray), respectively. Each curve can be fitted according to the model given by Eq. 2, yielding values of 0.3 (negative delay), 0.25 (6 ps delay), and 0.29 (1550 ps delay) for C_-, while C_+ remains at a constant value of 0.01. In panel b), the magnified saturation region marked by a black box in panel a) is shown.

The results of these fits are summarized in Fig. 3. Whilst the coupling constant C_+ remains at its constant small value of 0.01, it turns out that the constant C_- changes as a function of the delay time. To provide a better feeling for the magnitude of the interlayer exchange coupling and its corresponding changes, we also make use of an approximative formula given by Slonczewski [9], which translates the coupling constant C_- (for negligibly small C_+, which is the case here) into the more well−known bilinear coupling constant J_1:

$$J_1 = -\frac{C_- \pi^2}{2} \tag{3}$$

However, as mentioned above, the conventional model described by Eq. 1 is not really appropriate to describe the system investigated here, and thus Eq. 3 should just be considered a rough approximation.

It can be deduced from Fig. 3 that C_- is reduced in magnitude by about 15% within a few picoseconds and thereafter relaxes back to its original value of 0.3 ± 0.01 on a time scale of the order of several hundred picoseconds. In the following we will discuss the origin of this modulation.

It is known from the works of Beaurepaire et al. [1] that a rapid increase in temperature of the electron system of a metallic sample upon laser excitation is followed by thermalization between electron and spin system, which takes place on a time scale of the order of 2 ps (and is therefore not resolveable in our experiment). As it has been mentioned above, it can be estimated that this leads to a temperature increase of both electron and spin system by about 100 K, followed by a much slower recovery to room temperature. We therefore estimate that after the smallest experimentally resolveable delay time of 6 ps in our experiment, we probe a system whose electron and spin temperatures are increased by about 100 K from room temperature. As it has been discussed before, the interlayer exchange coupling within our system consists of two superimposed mechanisms, the quantum well mechanism and the proximity magnetism mechanism, where the latter mechanism is dominant.

It has been predicted theoretically [8] and proven experimentally [15–17] that the electronic contribution to the interlayer exchange coupling due to the quantum well mechanism, described by Eq. 1, has a temperature dependence of the form

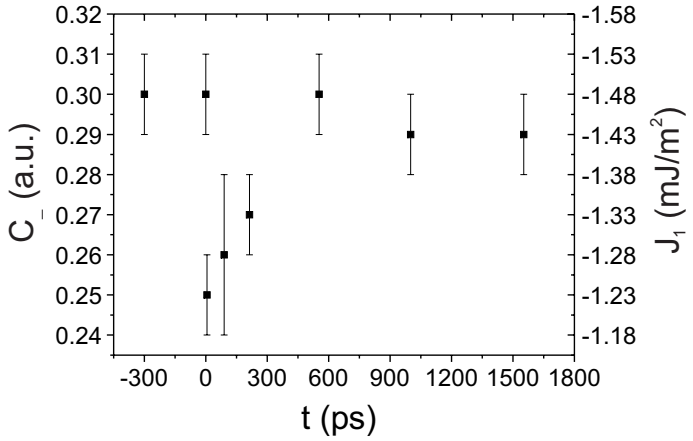

Fig. 3: Dependence of the coupling parameter C_- (and its corresponding value of J_1) on the pump−probe delay time. Two data points plotted at $t = -300\,\mathrm{ps}$ and $t = 0\,\mathrm{ps}$ correspond to the coupling parameter C_- at negative delay times. The scale for J_1 is calculated according to Eq. 3.

$$J_1(T) = J_1(0)\frac{T/T^*}{\sinh(T/T^*)} \quad , \quad \text{with} \quad T^* = \frac{\hbar v^\alpha}{2\pi k_B d} \quad , \tag{4}$$

where $d = 0.7\,\mathrm{nm}$ is the interlayer thickness and v^α is a measure of the Fermi velocity within the interlayer, which is typically of the order of $10^6\,\mathrm{m/s}$. According to Eq. 4, the electronic contribution to the interlayer coupling does not change by more than 1−2% in consequence of a temperature increase of less than 100 K, which is in strong contrast to the observed modulation of the coupling constants by about 15% in our experiment. We therefore exclude an increase of the electron temperature of our system as the main source of the observed modulation of the coupling.

On the other hand, the dominant proximity magnetism contribution to the coupling is mediated by exchange interaction of neighboring spins and is therefore dependent on the order of the *spin* system in the interlayer region [9]. A photo−excited thermal disorder of the spin system in this region will therefore also lead to an attenuation of the interlayer exchange coupling strength. Up to our knowledge, a temperature dependence of the proximity magnetism coupling mechanism has not been theoretically derived so far. However, it is known from the works of Ju et al. [3] and Weber et al. [4] that the exchange coupling mediated by the interfacial spin system in F/AF bilayers (which are not unlike the F/AF/F trilayer studied here) can be modulated on the ps time scale. In particular, it has been shown for the system NiFe/FeMn that a rapid increase of the interfacial spin temperature of the order of 100 K leads to a noticeable reduction of the coupling strength within this system, which also in this case happens within a few ps [4].

According to these considerations, we attribute the observed rapid drop of the interlayer exchange coupling strength within a few ps upon laser excitation to an optically induced thermal disorder of the spin system in the interlayer region, i.e., in the interfacial region of the trilayer. Moreover, the subsequent slower recovery of the coupling strength is governed by spin−lattice relaxation processes and by heat−flow out of the multilayer stack into the substrate. While the heat−flow properties of our sample are not directly accessible in the frame of our experiment, it has been shown by Vaterlaus et al. that the spin−lattice relaxation time in ferromagnetic Gd is of the order of $100 \pm 80\,\mathrm{ps}$ [13, 14]. Assuming that the corresponding value for Fe is of the same order, this result is in accordance with our observation that the relaxation of the interlayer exchange coupling strength takes place on a sub−ns time scale.

In summary, we have provided experimental evidence that it is possible to modulate the interlayer exchange coupling in Fe/Cr/Fe trilayers with smooth interfaces on the picosecond time scale, using an all−optical pump−probe technique. This modulation is attributed to an optically induced thermal disorder of the spin system in the interlayer region of the trilayer.

Support from the Deutsche Forschungsgemeinschaft is gratefully acknowledged.

References

[1] E. Beaurepaire, J.-C. Merle, A. Daunois, J.-Y. Bigot, Phys. Rev. Lett. **76**, 4250 (1996).
[2] J. Hohlfeld, E. Matthias, R. Knorren, K.H. Bennemann, Phys. Rev. Lett. **78**, 4861 (1997).
[3] G. Ju, A.V. Nurmikko, R.F.C. Farrow, R.F. Marks, M.J. Carey, B.A. Gurney, Phys. Rev. Lett. **82**, 3705 (1999).
[4] M.C. Weber, H.T. Nembach, S. Blomeier, B. Hillebrands, R. Kaltofen, J. Schumann, M.J. Carey, Euro. Phys. J. B **45**, 243 (2005).
[5] S. Blomeier, B. Hillebrands, V.E. Demidov, S.O. Demokritov, B. Reuscher, A. Brodyanski, M. Kopnarski, J. Appl. Phys. **98**, 093503 (2005).
[6] D.T. Pierce, J. Unguris, R.J. Celotta, M.D. Stiles, J. Magn. Magn. Mater. **200**, 290 (1999).
[7] M.C. Weber, H.T. Nembach, B. Hillebrands, J. Fassbender, IEEE Trans. Magn. **41**, 1089 (2005).
[8] D.E. Bürgler, P. Grünberg, S.O. Demokritov, M.T. Johnson, Handbook of Magnetic Materials, Vol. 13, edited by K.J.H. Buschow, Elsevier, Amsterdam (2001).
[9] J.C. Slonczewski, J. Magn. Magn. Mater. **150**, 13 (1995).
[10] A. Schreyer, C.F. Majkrzak, T. Zeidler, T. Schmitte, P. Bödeker, K. Theis-Bröhl, A. Abromeit, J.A. Dura, T. Watanabe, Phys. Rev. Lett. **79**, 4914 (1997).
[11] N.M. Kreines, D.I. Kholin, S.O. Demokritov, M. Rickart, J. Exp. Theor. Phys. **78**, 1121 (2003).
[12] B. Koopmans, M. van Kampen, J.T. Kohlhepp, W.J.M. de Jonge, Phys. Rev. Lett. **85**, 844 (2000).
[13] A. Vaterlaus, T. Beutler, F. Meier, Phys. Rev. Lett. **67**, 3314 (1991).
[14] A. Vaterlaus, T. Beutler, D. Guarisco, M. Lutz, F. Meier, Phys. Rev. B **46**, 5280 (1992).
[15] S.O. Demokritov, A.B. Drovosekov, N.M. Kreines, H.T. Nembach, M. Rickart, D.I. Kholin, J. Exp. Theor. Phys. **95**, 1062 (2002).
[16] M. From, L.X. Liao, J.F. Cochran, B. Heinrich, J. Appl. Phys. **75**, 6181 (1994).
[17] B.G. Almeida, V.S. Amaral, J.B. Sousa, J. Colino, I.K. Schuller, J. Magn. Magn. Mater. **177-181**, 1170 (1998).

C. Exchange Bias Effect

6.17 Orthogonal exchange bias field directions in FeMn/NiFe microstructures

P. Candeloro, H. Schultheiß, H.T. Nembach, B. Hillebrands[1]

The exchange bias effect arises in ferromagnetic(F)/antiferromagnetic(AF) bilayers when the uncompensated AF spins near the F/AF interface are mostly aligned along one direction [1]. In these circumstances, the exchange coupling at the F/AF interface acts as an internal field which shifts the hysteresis loop by the so-called exchange bias field, H_{eb}. The most common techniques to achieve the alignment of the uncompensated AF spins are either the deposition of the F/AF bilayer in an external applied field or cooling the sample through the Néel temperature (T_N) in a field. Under these conditions the external field is saturating the F layer, which in turn affects the final arrangement of the AF spins. The resulting H_{eb} direction will be the same as the external field, unless this latter one is large enough to affect directly the AF spins; in this case also the opposite direction, "positive" exchange bias, is possible for some F/AF systems [2]. Excepting extreme situations, the exchange bias direction is determined by the interaction with the F layer and not directly by the external field. Recently several reports have shown the occurrence of double-shifted hysteresis loops in exchange bias continuous films, i.e. hysteresis loops divided in two sub-loops, one shifted to negative fields and the other to positive ones [3–5]. This effect is usually observed combining the demagnetization of the sample above T_N with a following zero-field cooling (ZFC) procedure. If the F layer presents an uniaxial anisotropy, the demagnetization will produce domains with opposite magnetizations along the easy axis. Then, during the ZFC step, the uncompensated AF spins are coupled to the F ones along opposite orientations for the different domains, providing an exchange bias shift toward negative fields in some regions of the film and toward positive fields in the other regions.

In the present work [6] a ZFC procedure is exploited to achieve two *orthogonal* directions of H_{eb} coexisting together in the same microstructure (for a recent review on exchange bias in nanostructures see J. Nogués et al. [7]). Compared to previous works dealing with a continuous F layer, confined magnetic elements with suitable geometry allow for multiple directions of the exchange bias field and for the control of the spatial distribution of these directions. In a continuous film with uniaxial anisotropy only one axis (that of the easy-direction) with two opposite orientations is allowed for the magnetization in zero field; furthermore the demagnetizing process does not offer any control on the spatial location of the opposite-oriented domains. Instead, in confined elements with L-like and cross-like shapes, the magnetization can be easily aligned along the microstructures arms because of the shape anisotropy, thus providing two different and clearly located axes for the exchange bias field.

The magnetic microstructures (Fig. 1) are fabricated from a polycrystalline $Fe_{50}Mn_{50}$(12 nm)/$Ni_{81}Fe_{19}$(5 nm) continuous bilayer by means of lithographic techniques [8]. Both the L-like and cross-like shapes have the dimensions of $0.7\,\mu m \times 4.0\,\mu m$ per arm; for the subsequent comparison of the magnetic measurements also vertical bars of dimensions $0.7\,\mu m \times 4.0\,\mu m$ (not shown in Fig. 1) are fabricated on the same sample. In order to initialize the exchange bias field, the sample

[1] In collaboration with S. Trellenkamp, C. Dautermann, and S. Wolff, Nano+Bio Center, Technische Universität Kaiserslautern, Germany

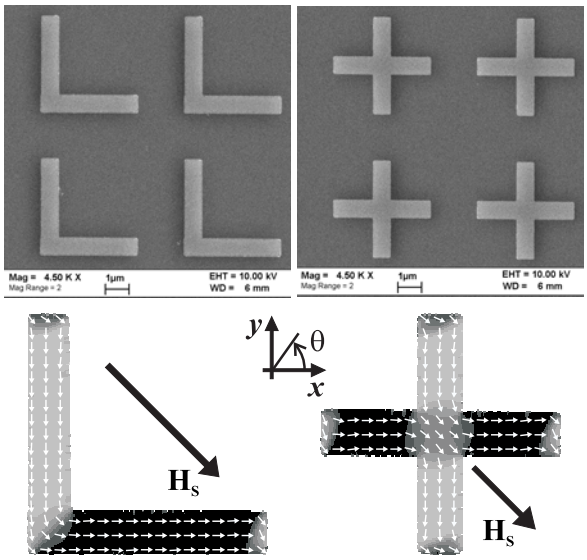

Fig. 1: First row: SEM pictures of the fabricated L-like and cross-like microstructures; the structures arms are $0.7\,\mu\text{m}\times 4.0\,\mu\text{m}$ and the structure period is $6\,\mu\text{m}$ in both the horizontal and vertical directions. Second row: micromagnetic simulation of the domains configuration using the OOMMF code after removing the saturation field H_S. The magnetization is mainly oriented parallel to the arms, but some domains along the -45° direction are observable at the arms ends and at the intersection of the arms.

is heated above T_N of $Fe_{50}Mn_{50}$, and a saturating field $H_S = 1\,\text{kOe}$ is applied along the diagonal to the L-like and cross-like structures. Then the external saturating field is removed, while keeping the temperature $T > T_N$. Due to the shape anisotropy, the magnetization in zero field is aligned along the microstructures arms, orthogonal to each other. The results of a micromagnetic simulation of this step using the OOMMF code [9] are shown in the bottom row of Fig. 1. Subsequently, zero-field cooling through the Néel temperature induces different exchange bias directions inside the same structure, according to the magnetization orientation.

Hysteresis loops for all the patterns (bars, L-shapes and crosses) are measured by means of a magneto-optical Kerr effect (MOKE) magnetometer setup, varying the angle of the external field. We define the x and y axes as indicated in Fig. 1, and the angles are counted counterclockwise starting from the positive x semi-axis; the bars are oriented with the long side parallel to the y axis. The results of the MOKE measurements are presented in Fig. 2. While the bars exhibit clearly a single hysteresis loop with exchange bias field along the -90° direction, the hysteresis curves of the L-shapes and the crosses are composed of two sub-loops. When the external field H_{ext} is applied along the positive x axis (0° direction), the horizontal arms of the L-shapes and the crosses will provide an easy-axis contribution to the hysteresis curve, while the vertical ones will contribute with a hard-axis behavior; a reversed situation is expected to occur for H_{ext} directed along the y axis. From Fig. 2 it is evident that the hysteresis curves measured for H_{ext} along 0° and 90° are exactly the superpositions of a easy-axis loop and a hard-axis one. Furthermore, the easy-axis contribution is shifted toward negative fields for H_{ext} along 0° and toward positive fields for H_{ext} along 90°, indicating that the exchange bias field is oriented along 0° for the horizontal arms and along -90° for the vertical ones. These results are in agreement with the orientations expected after applying H_S along -45° (Fig. 1).

If homogeneous magnetizations are assumed to exist in the horizontal and vertical arms separately, and if their potential interaction is neglected, the free energy E of L-shapes and crosses can be written as the sum of two terms, one for each arm:

$$\sum_{i=1,2} -H_{ext}M_{S,i}\cos(\theta_i-\theta_H) - K_{eb,i}\cos(\theta_i-\theta_{eb,i}) + K_{u,i}\cos^2\theta_i \quad , \tag{1}$$

where the subscripts 1 and 2 refer, respectively, to the horizontal and vertical arms. $M_{S,i}$ is the saturation magnetization of the i-th arm, $K_{eb,i}$ and $K_{u,i}$ are, respectively, the unidirectional (exchange

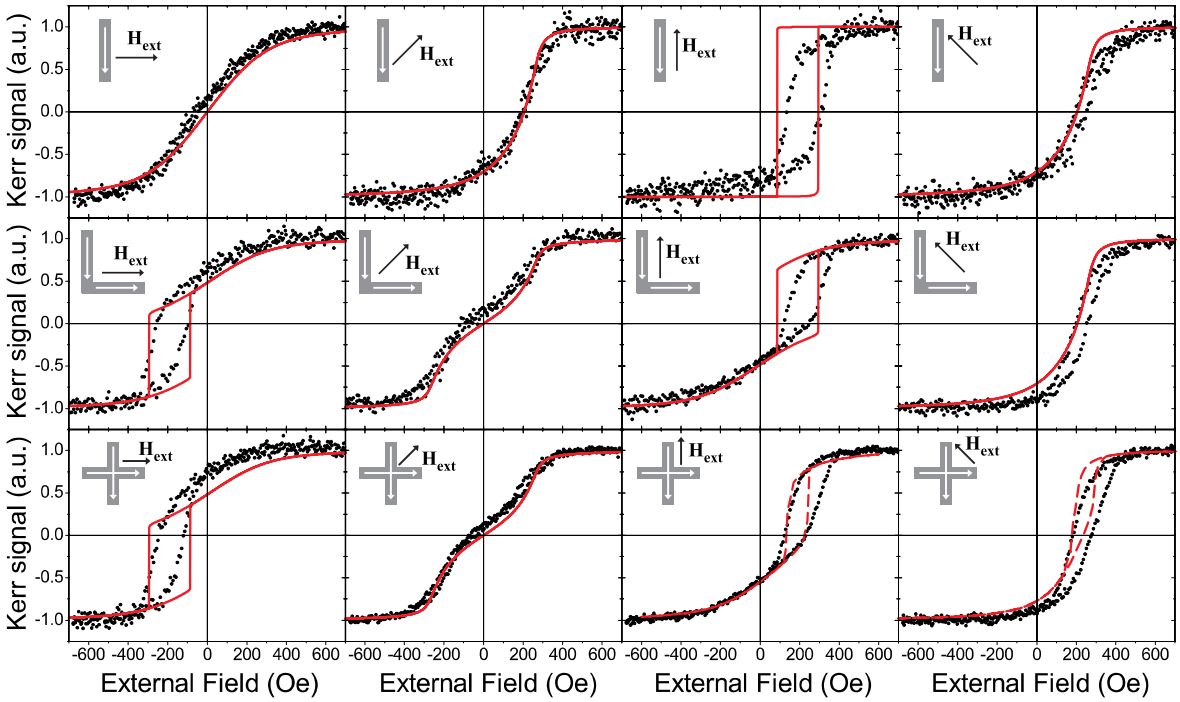

Fig. 2: Hysteresis loops measured by MOKE magnetometry for the bar-like (top row), L-like (middle row) and cross-like (bottom row) structures. The external field was applied along 0° (first column), 45° (second column), 90° (third column) and 135° (last column) as indicated by the black arrows in the drawings. The white arrows indicate the exchange bias directions inside the structures. While the bars exhibit only one shifted easy-axis loop for external field along the 90° direction, the L-like and cross-like structures show shifted easy-axis sub-loops for both the 0° and 90° directions. Experimental hysteresis loops (symbols) are simulated through a coherent rotation model (solid lines). The features of the experimental curves not well reproduced by the coherent rotation model are properly simulated through micromagnetic calculations (dashed lines in the last two graphs of the bottom row, i.e. crosses loops with external field along 90° and 135°).

bias) and the uniaxial (shape anisotropy) constants for the i-th arm. All the angles are counted with respect to the positive x semi-axis, and they are θ_H for the external field, $\theta_{eb,i}$ for the exchange bias direction in the i-th arm and θ_i for the magnetization $M_{S,i}$. Similarly to earlier works investigating the interplay between the unidirectional and the shape anisotropies [10, 11], Eq. 1 is here used within a coherent rotation model [12] in order to calculate the hysteresis loops via energy minimization. We use $4\pi M_{S,i} = 10.8\,\mathrm{kG}$ for permalloy; the unidirectional exchange bias constant $K_{eb,i}$ can be determined directly from the hysteresis loops measured along 0° and 90° and it is $K_{eb,i}/M_{S,i} = H_{eb,i} \approx 200\,\mathrm{Oe}$ for both the directions; $\theta_{eb,1}$ and $\theta_{eb,2}$ are fixed to 0° and $-90°$ respectively. Finally, for the shape anisotropy energy we use the following formula:

$$K_{u,i}\cos^2\theta_i = 2\pi M_{S,i}^2(D_{ix} - D_{iy})cos^2\theta_i \quad , \tag{2}$$

where D_{ix} and D_{iy} are the demagnetizing factors of the i-th arm, respectively along the x and y axes, and they are evaluated through the approximated formula for rectangular prisms reported by Aharoni [13]. The numerically determined hysteresis loops are shown in Fig. 2; in the case of the bars only one of the two terms in Eq. 1 is used for the energy minimization. Despite the simplicity of the model, the qualitative agreement with the measured loops is remarkable, considering also that none of the parameters in Eq. 1 was determined by fitting procedures. For all the directions of H_{ext} the main features of the curves are well reproduced, and in several cases (e.g. H_{ext} along 45°) also the quantitative agreement is considerable. The most significant disagreements occur when the

experimental data show a hysteretic behavior: for H_{ext} along 0° and 90° the easy-axis sub-loops are not well reproduced, while for 135° the calculated loops have no hysteresis. These discrepancies have origins of different nature. For the 0° and 90° hysteresis curves, the coherent rotation model does not take into account the nucleation of closure domains at the edges of the arm parallel to the external field (i.e. the arm in easy-axis configuration with respect to H_{ext}), and exactly these domains are responsible for the less abrupt magnetization reversal observed in the experimental data. Instead, concerning the non-zero hysteresis of the 135° experimental loops, we suppose that small regions biased along the −45° direction are present in the microstructures. With reference to Fig. 1 we can see that, after removing H_S, small domains nearly oriented along −45° are observable at the edges of the arms (closure domains) and at the intersection of the two arms. This is more evident for the crosses, where the central area constitutes a −45° domain. This fingerprint of the F layer is then transmitted to the uncompensated AF spin arrangement through the cooling step. Obviously the magnetization reversal will be affected by these regions and the hysteresis loops will present some features related to a −45° bias initialization, like a non-zero hysteresis when H_{ext} is along −45° (or equivalently 135°). To support this hypothesis we can observe that no hysteresis is exhibited by the curves measured along 45°, since this is a hard-axis also for the small −45° biased regions; moreover, the hysteretic behavior along 135° is more pronounced for crosses than for L-shapes and bars, in agreement with the percentage area occupied by the −45° domains after the removal of H_S (Fig. 1). Finally, we performed micromagnetic simulations [9] of the hysteresis loops to take into account the effects of both the closure domains and the −45° biased areas. In the calculations only the F layer is modeled on a microscopic scale, while the coupling with the antiferromagnet is simulated through a 200 Oe fixed field. The different biasing directions are provided by a non-uniform orientation of this field. More in details, the fixed field in the L-like and cross-like structures is oriented as the magnetic configurations shown in Fig. 1. This mainly produces three different areas with different biasing directions (along 0°, −90° and −45°). For the calculations we use $4\pi M_S = 10.8\,\mathrm{kG}$ and a mesh-size of (20 nm×20 nm×5 nm). Results of these simulations are presented for crosses with the external field applied along 90° and 135° (Fig. 2). A substantial improvement of the overall agreement can be observed. In fact, the micromagnetic calculation allows for the nucleation of domains during the hysteresis loop, thus producing a less abrupt reversal for the 90° curve compared to the coherent rotation result. Moreover, for the 135° curve, the −45° biased areas included in the micromagnetic model give rise to a hysteretic behavior similar to the experimental one. The discrepancies still present between the calculated and experimental loops are likely due to slight differences between the fixed field of the simulations and the real exchange bias field.

For the L-structures we have investigated in more detail the dependence of the exchange bias H_{eb} and the coercivity H_C upon the external field direction, θ_H. For this purpose we use the conventional definition of exchange bias field, which is the mean value of the left branch and right branch coercive fields of a hysteresis loop. On the other hand we want to notice that this definition is not always providing the effective biasing field for hysteresis curves composed by two sub-loops (e.g. the curves along 0° and 90°). Figure 3 summarizes the collected experimental data (symbols) and the expected behavior calculated with the coherent rotation model (lines). Qualitatively the coherent rotation model predicts the general trend of the experimental data. Due to the reasons discussed above, we have a significant underestimate of the coercivity when θ_H is close to −45° or to 135°, while it is overestimated for θ_H oriented along the structures arms (i.e. the x and y axes). Concerning H_{eb}, both the experimental data and the simulated curve indicate that the maximum bias field is not achieved along the structures arms, as it could be naively expected. The misalignment between the biasing axis and the maximum H_{eb} direction arises because of the

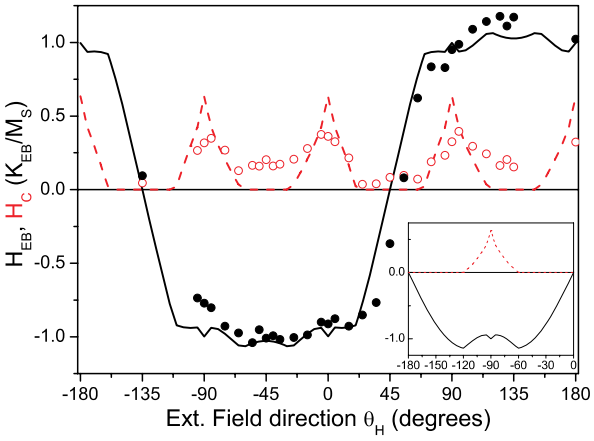

Fig. 3: Dependence of the bias field and the coercivity on the external field direction for the L-like structures. The experimental data (closed symbols for the bias field, open symbols for the coercivity) are compared to the curves calculated through the coherent rotation model (full line for the bias field, dashed line for the coercivity). The maximum bias field is achieved for directions 30° out of arms axes; this effect is due to the competition between unidirectional and uniaxial anisotropy and it is present also for the bar-like structures (calculated line shown in the inset).

interplay between unidirectional and uniaxial anisotropies. This effect was already observed in simple line microstructures [11] (where the uniaxial anisotropy is due to the shape) as well as in continuous films with large uniaxial anisotropy [14]. The inset of Fig. 3 shows the dependence of H_{eb} upon θ_H calculated for the bars structures. The maximum H_{eb} is found to be at $\theta_H = -60°$ and $-120°$, that is 30° out of the exchange bias axis. This result agrees with the value calculated through the analytical equations reported by Chung et al. [11].

In conclusion, exchange bias fields with orthogonal directions are simultaneously initialized within the same microstructure exploiting shape anisotropy and zero field cooling procedures. Furthermore, the confined magnetic elements allow for a full control on the spatial distribution of the biasing axes. To our knowledge this is the first reported case of a double-axis configuration for the exchange bias field and a full report is given in [6]. Further engineering of the microstructures shapes can make available manifold H_{eb} directions (more than two axes). Nevertheless, one has to consider that the ratio between the F and AF domain sizes is of crucial importance for tailoring the exchange bias through ferromagnetic domains and ZFC procedures [4]. Specifically, F domains have to be larger than the AF ones. Once this condition is fulfilled, any stable and reproducible domain configuration of the ferromagnetic layer can be used to initialize multi-axis exchange bias fields.

This work is supported in part by the European Communities Human Potential program under contract number HPRN-CT-2002-00296 NEXBIAS.

References

[1] For a review of exchange bias, see J. Nogués, I. K. Schuller, J. Magn. Magn. Mater. **192**, 203 (1999).
[2] J. Nogués, D. Lederman, T. J. Moran, I. K. Schuller, Phys. Rev. Lett. **76**, 4624 (1996).
[3] I. V. Roshchin, O. Petracic, R. Morales, Z.-P. Li, X. Batlle, I. K. Schuller, Europhys. Lett. **71**, 297 (2005).
[4] S. Brück, J. Sort, V. Baltz, S. Suriñach, J. S. Muñoz, B. Dieny, M. D. Baró, J. Nogués, Adv. Mater. **17**, 2978 (2005).
[5] P. Miltényi, M. Gierlings, M. Bamming, U. May, G. Güntherodt, J. Nogués, M. Gruyters, C. Leighton, I. K. Schuller, Appl. Phys. Lett. **75**, 2304 (1999).
[6] P. Candeloro, H. Schultheiß, H. T. Nembach, B. Hillebrands, S. Trellenkamp, C. Dautermann, S. Wolff, Appl. Phys. Lett. **88**, 192510 (2006).
[7] J. Nogués, J. Sort, V. Langlais, V. Skumryev, S. Suriñach, J. S. Muñoz, M. D. Baró, Phys. Rep. **422**, 65 (2005).
[8] F. Rousseaux, D. Decanini, F. Carcenac, E. Cambril, M. F. Ravet, C. Chappert, N. Bardou, B. Bartenlian, P. Veillet, J. Vac. Sci. Technol. B **13**, 2787 (1995).
[9] The free code OOMMF is used for the micromagnetic simulations: http://math.nist.gov/oommf/
[10] A. Hoffmann, M. Grimsditch, J. E. Pearson, J. Nogués, W. A. A. Macedo, I. K. Schuller, Phys. Rev. B **67**, 220406 (2003).

[11] S. H. Chung, A. Hoffmann, M. Grimsditch, Phys. Rev. B **71**, 214430 (2005).
[12] E. C. Stoner, E. P. Wohlfarth, Philos. Trans. R. Soc. London, Ser. A **240**, 74 (1948).
[13] A. Aharoni, J. Appl. Phys. 83, 3432 (1998).
[14] J. Camarero, J. Sort, A. Hoffmann, J. M. García-Martín, B. Dieny, R. Miranda, J. Nogués, Phys. Rev. Lett. **95**, 057204 (2005).

D. Transfer of Technology

6.18 Tunneling magneto resistance microstructures on top of coplanar waveguides

G. Wolf, S. Becker, P. Martín Pimentel, B. Leven, and B. Hillebrands[1]

Recently there has been important progress in the field of magnetic logic. Magnetic logic gate arrays, containing tunneling magneto resistance (TMR) microstructures, have been successfully demonstrated by the group of Prof. G. Reiss at the University of Bielefeld [1]. Such TMR elements generally consist of a sandwich structure with two ferromagnetic (FM) layers, separated by an insulating layer. One of the FM layers is pinned by an adjacent antiferromagnetic (AFM) layer via the exchange bias effect, while the magnetization of the other FM layer is free to switch in an applied magnetic field. The electrical resistance of the multilayer system strongly depends on the relative orientation of the magnetizations of these two layers. In particular, the logic states “0” and “1” correspond to a large resistance at antiparallel orientation and a small resistance at parallel orientation, respectively.

For technological applications the magnetization dynamics of TMR elements is of fundamental importance. For this purpose, it is necessary to fabricate the TMR microstructures on top of the crossing point of two crossed 3D coplanar waveguides. The preparation of such a device is subject of this report. A suitable 3D waveguide design for such investigations has been developed by P. Martín Pimentel et al. [2]. While the coplanar waveguides were processed in the Nano+Bio Center of the TU Kaiserslautern, the TMR elements were fabricated in cooperation with the group of Prof. G. Reiss at the University of Bielefeld.

Ellipsoidal microelements of different lateral dimensions were prepared on top of the waveguides by means of electron beam lithography (EBL) and magnetron sputtering. A magnetron sputtering chamber CLAB 600 Clustertool from Leybold Vakuum GmbH was employed for deposition, while an EBL system LEO 1530 from LEO Electron Microscopy Ltd. was used for the patterning processes. Both positive and negative lithography processes can be utilized for the fabrication of the TMR elements. In both cases, in order to prevent the insulating substrate of the waveguide to be charged during the EBL process, a 7 nm Ru layer was deposited onto the sample first.

During the positive process a photo resist provided by Allresist GmbH containing a copolymer based on Methylmethacrylat and Methacrylacid (PMMA/MA) was spin coated. The long axis of the ellipse was oriented perpendicular to the reset line of the coplanar waveguide system. After developing the exposed resist in a suitable developer, a Ta/Cu multilayer was sputtered to improve the adhesion on the coplanar waveguide system.

For the pinned ferromagnetic layer system a 3 nm CoFeB FM layer is used in combination with a 12 nm antiferromagnetic MnIr layer, while the insulating layer consists of Al_2O_3 with a thickness of 1.8 nm, fabricated by deposition of Aluminum and subsequent plasma oxidation. CoFeB is also used for the free FM layer, which has a thickness of 4 nm. Finally, a 10 nm Ta and a 7 nm Ru layer were deposited on top of the free FM layer as capping layers (see inset Fig. 1). For the following lift-off process N-Methyl-Pyrrolidon (NMP) was used with the additional support of ultrasonic and heat treatment.

[1] In cooperation with K. Rott and G. Reiss, Fakultät der Physik, Universität Bielefeld, Germany.

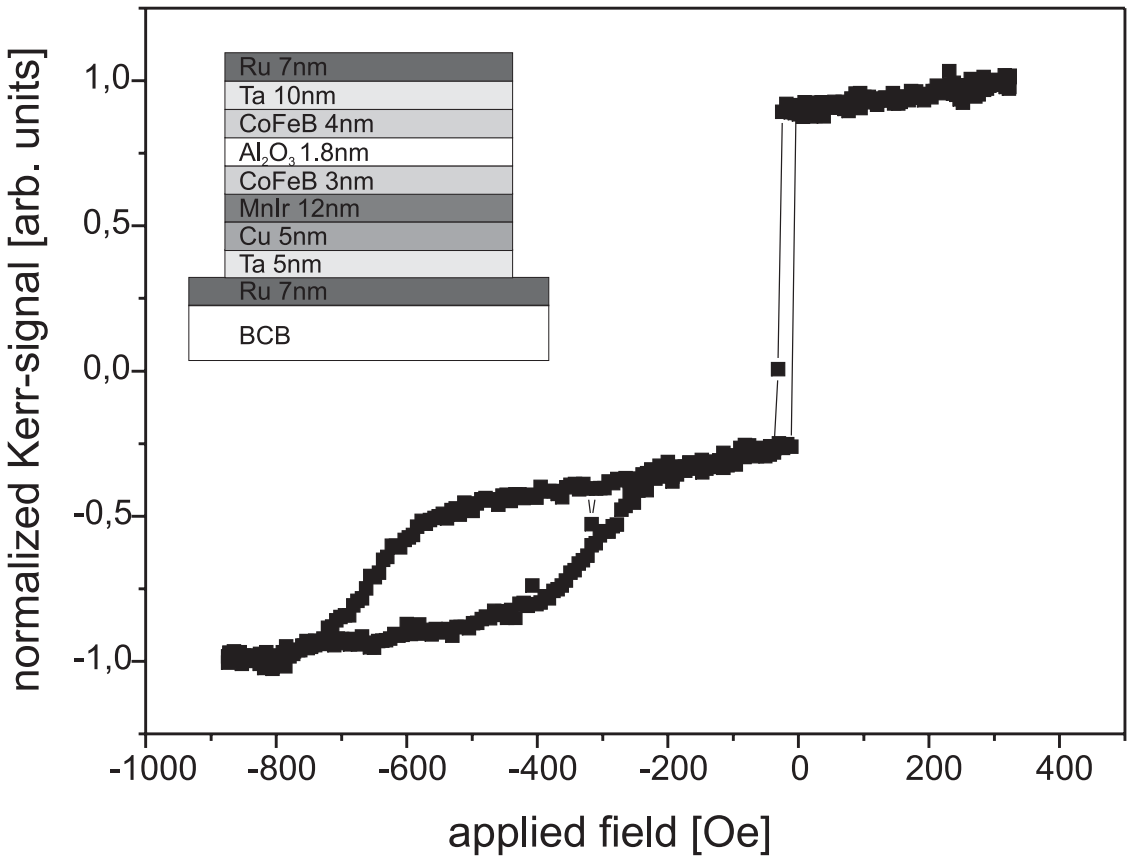

Fig. 1: MOKE-measurement on a continuous Ru/Ta/Cu/MnIr/CoFeB/Al_2O_3/CoFeB/Ta/Ru film. The free ferromagnetic layer shows a rather small coercive field, while the pinned ferromagnetic layer can only be reversed at higher fields. The exchange bias field is approximately 500 Oe. Inset: Schematic cross-section of the full multilayer stack.

Exchange bias was initialized at the CoFeB/MnIr interface by means of a standard field cooling procedure above the Néel temperature of the AFM in the presence of an external magnetic field, while remaining below the Curie temperature of the FM layer [1]. In this temperature range the magnetic moments in the antiferromagnet are thermally disordered while the magnetic moments in the ferromagnet are oriented in the direction of the external field. During the following cooling process the AFM moments close to the interface arrange themselves parallel to the FM moments. For this purpose the system is heated up to 275 °C for 30 minutes under vacuum conditions, to prevent oxidation. The external field is applied in easy axis direction along the long axis of the ellipse by means of a permanent magnet. As a final step Argon ion etching controlled by a quadrupol mass spectrometer was used to remove the conducting layer of Ru used for the EBL-process.

In contrast to the positive process described above, during the negative process the whole multilayer system is deposited first. After an identical field cooling procedure, the ellipse was written by EBL using a negative resist provided by Allresist GmbH. The exposed ellipse is not soluble in the developer and therefore protects the multilayer system in the following Argon ion etching process. Finally the resist was removed in NMP together with ultrasonic and heat treatment.

A magneto-optic Kerr effect (MOKE) measurement on a TMR reference film is shown in Fig. 1. Because of its rather small coercive field, the free ferromagnetic layer can be reversed easily, while the pinned layer is reversed at higher fields because of the 500 Oe exchange bias field.

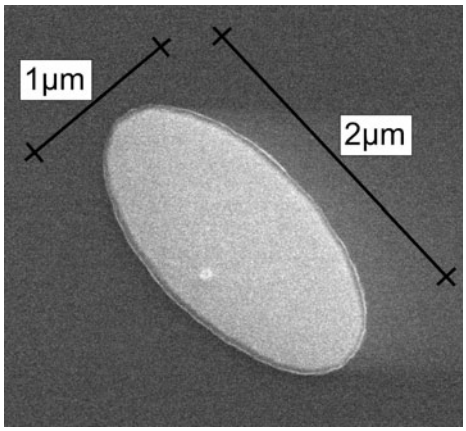

Fig. 2: SEM-picture (top view) of a positive processed $1\,\mu m \times 2\,\mu m$ ellipse after the lift-off procedure. At this size, the ellipsoidal shape can be reproduced easily. On the edge of the ellipse some material is still remaining, which could not be lifted. The magnetic easy axis direction is oriented along the long axis of the ellipse.

A positive processed $1\,\mu m \times 2\,\mu m$ ellipse is shown in Fig. 2. The picture was taken after the lift-off procedure. It can be seen that some material, which could not be lifted, is still remaining on the edge of the ellipse. This is characteristic for the positive process. Except for this, the favored geometry could be well prepared, which is crucial for further investigations.

In summary, ellipsoidal microelements were successfully fabricated on top of coplanar waveguides exploiting both positive and negative resist processes. Further investigations will concentrate on the dynamics of the magnetic switching process of this multilayer system, which will experimentally be investigated by means of time-resolved Kerr microscopy.

The authors would like to thank the group of Prof. G. Reiss, especially Dr. K. Rott. The work is supported by the European Commission within the EU-STREP project MAGLOG FP6-50021.

References

[1] D. Meyners, Herstellung und Charakterisierung von Logikarrays mit ultrakleinen magnetischen Tunnelelementen, Dissertation, Fakultät der Physik, Universität Bielefeld (2006).
[2] P. Martín Pimentel, S.J. Hermsdoerfer, H.T. Nembach, B. Leven, B. Hillebrands, Appl. Phys. Lett. **88**, 122510 (2006).

6.19 Immobilization of therapeutic agents on amorphous carbon coated surfaces

L. Kleinen, U. Böde, and B. Hillebrands[1]

Among the currently known biomaterials, diamond-like amorphous carbon coatings (DLC, a-C:H) stand out due to the variability in their composition and their remarkable physical and chemical properties in the field of microbiology and medicine. Several investigations proved their excellent compatibility in respect to blood and bone cells, and to human keratinocytes [1–4].

Amorphous carbon thin films can be prepared by miscellaneous deposition methods (e.g. ion deposition, sputtering, pulsed laser deposition, plasma enhanced chemical vapor deposition) all using accelerated hydrocarbon ions as film forming particles.

Diamond-like amorphous carbon is a thermodynamically metastable state of amorphous carbon, in which diamond-like (sp^3-hybridized) and graphite-like (sp^2-hybridized) bonding coexist, with large fraction of sp^3 bonds [5]. The coatings in general are characterized by high mechanical hardness, wear resistance, low friction and chemical inertness. Depending on the deposition conditions, the properties of the films can be adjusted for several applications, e.g., to enhance wear- and corrosion resistance of precision cutting and machining tools or to act as gas diffusion barriers on food wrappers or on containers for volatile solvents. To add further functionality to the coatings they can be modified by the addition of appropriate elements, e.g., nitrogen, oxygen or fluorine to change the wettability or the free energy of the surface, respectively, - both parameters influence cell proliferation and cell spread [6, 7].

By incorporation of reactive groups capable to form strong bonds with therapeutic agents, such as bactericides, anticoagulants or growth factors, it is possible to further functionalize the amorphous carbon coatings and use them for controlled local drug delivery in association with implantable devices. These plasma surface grafting techniques have already been well established with respect to polymers. However, in many applications, polymeric materials cannot be used. Most polymers, for example, are porous and lack the mechanical stability required for orthopedic implants or vascular stents. Thus, the development of a substrate-independent coating, combining the above mentioned diamond-like carbon surface properties with binding sites for active agents, is a promising approach that opens new fields of biomedical applications.

In general, carboxylic or amino groups can be considered as binding sites for active agents. The introduction of amino groups by using ammonia gas as an additional precursor has two main advantages. First, amino groups are known to facilitate cellular spreading on biomaterial surfaces allowing good implant integration. Second, amino groups react readily with several other functional groups, allowing attachment of specific molecules through interactions which are strong enough to prevent leaching of agents. For example, amino groups can be used to ionically immobilize heparin, a well known polysaccharide anticoagulant, or ethacridine lactate, a typical bactericide.

The immobilization of active agents can be achieved by direct bonding to the amino groups located at the coated surface or by applying a spacer molecule with at least two functional groups, one bonded to the amino binding site on the surface and the other to a functional group of the drug molecule. Some applications require a controlled release of the active agent from the implant into

[1] In collaboration with N. Laube, Universitätsklinikum Bonn.

the surrounding tissue. In this case, the spacer molecule can be designed to ensure reproducible release kinetics by providing the adequate bonding type.

We deposit amorphous carbon films with incorporated amino groups from an acetylene/ammonia precursor gas mixture. The rf-driven plasma source working at 13.56 MHz allows adjustment of the dissociation and ionization of the gas molecules by variation of rf-power and precursor gas flows. With this procedure, type (e.g. NH, NH_2) and amount of functional groups on the surface can be changed.

In order to determine the density of the amino groups on the surface, a so-called *succinic acid assay (SAA)* was established. The *SAA* uses a small spacer molecule which is first covalently attached to potential binding sites at the surface, preferably to NH_2 groups. In a second step, the molecule is removed from the surface and quantified using gas chromatography - mass spectrometry (GC/MS).

With the *SAA*, all functional groups acting as binding sites for the spacer molecule are detected. The method is not exclusively sensitive to the NH_2 groups. However, with respect to the problem of drug loading, the amount of spacer- or drug-molecules bonded to the surface is the relevant parameter which can be quantified reliably with the *SAA*.

The selection of succinic acid as detecting molecule from the homologous series of dicarboxylic acids was motivated by the linear conformation of the molecule. This ensures negligible sterical hindrance at the surface and allows for a dense package of spacer molecules if the coating provides a sufficient amount of binding sites. With its two carboxylic groups, succinic acid can act as linking molecule between surface functional groups and active agents. With a chain of only four carbon atoms, the probability of molecule bending and bridging with both carboxylic groups to the surface can be excluded. Furthermore, succinic acid is known as a nontoxic product of the human metabolism.

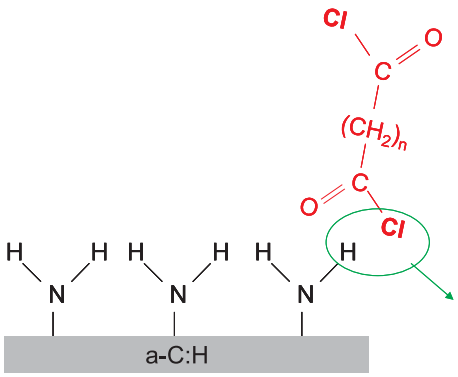

Fig. 1: Covalent attachment of carboxylic acid dichloride (for succinyl chloride: n = 2) to primary amino group via amid bond.

The covalent bonding of succinic acid to the amino groups on the surface is achieved by using a 10% solution of succinyl chloride in chloroform. As the succinyl chloride shows strong reactions with metals, the a-C:H/NH_3 films are deposited on teflon samples, sized $2 \times 2\,cm^2$; the center of this chip was coated with a circular $2\,cm^2$ area. Ten teflon samples of each coating type as well as ten uncoated teflon reference samples are immersed for 90 min in 50 ml of the succinyl chloride/chloroform solution allowing the saturation of the amino groups with succinyl chloride by forming an amid bond under formation of hydrochloric acid (Fig. 1). Next, the samples are washed in chloroform and distilled water as shown in Fig. 2 in order to remove excessive succinyl chloride. In contact with H_2O, the remaining chloride atom of the bonded succinyl chloride molecules is replaced by a hydroxy group. After this washing procedure, the amino groups on the surface are saturated with succinic acid molecules. By immersing the samples in 3 ml NaOH at pH 12, the

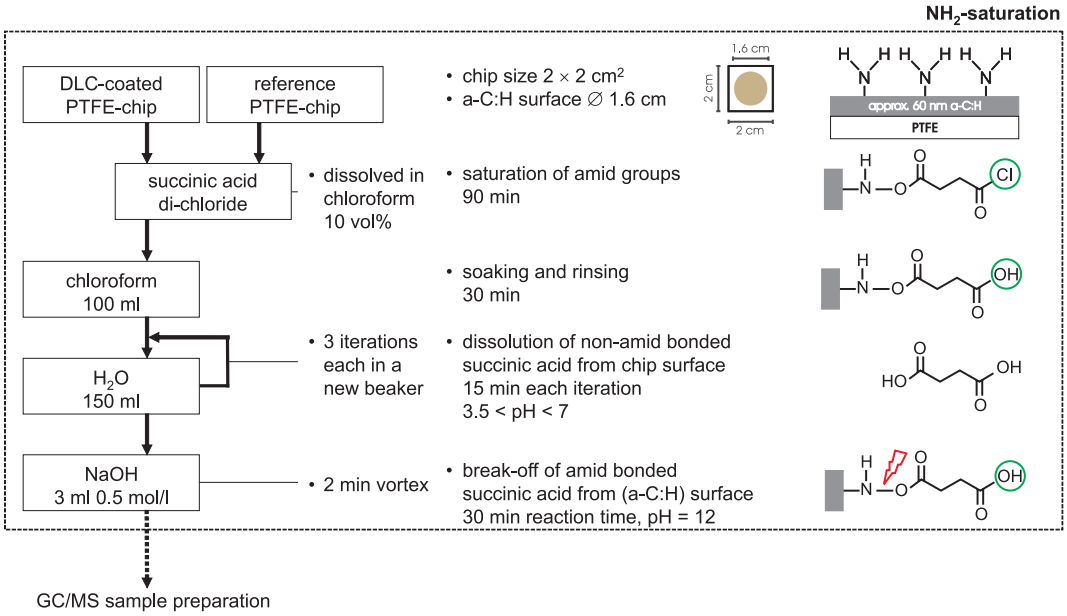

Fig. 2: Experimental protocol for spacer molecule saturation of the surface NH_2 groups and subsequent dissolution of the formed covalent bonds.

amid bonds are dissolved and the succinic acid molecules are transferred into the NaOH solution (Fig. 2 bottom).

To 200 µl of the obtained succinic acid/NaOH solution, 30 µl of 20 µmolar glutaric acid is added as internal standard for GC/MS measurements. Glutaric acid was chosen because of the chemical similarities to succinc acid, both are linear dicarboxylic acids with only one CH_2 group difference.

The sample solution is then acidulated by addition of 10 µl of 25% hydrochloric acid. Both dicarboxylic acids are extracted from the aqueous phase with 500 µl ethyl acetate.

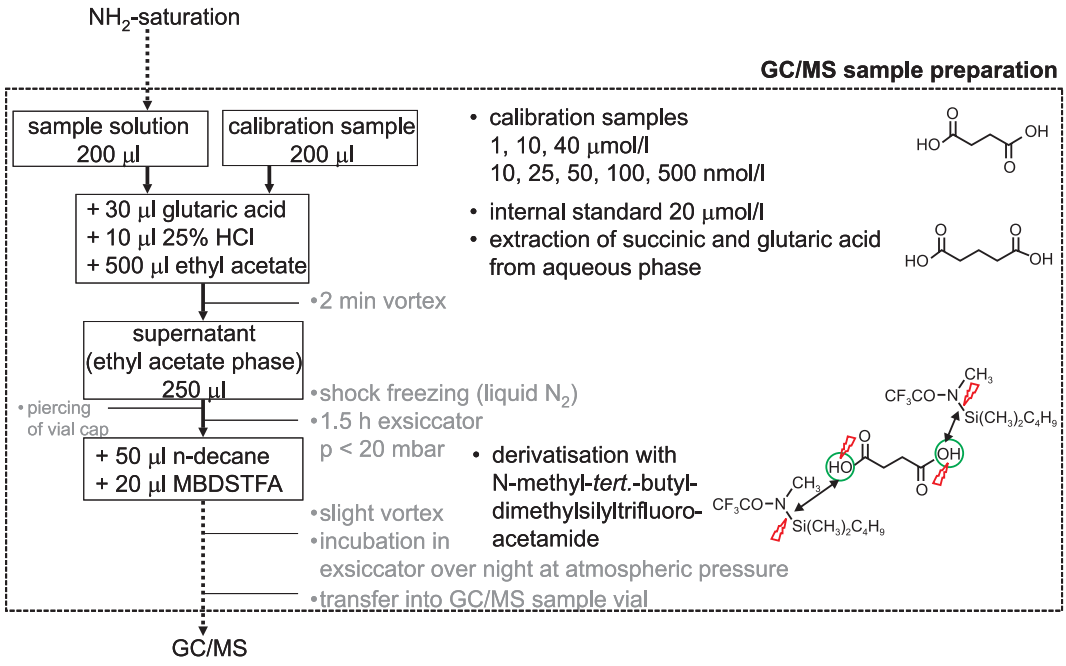

Fig. 3: Preparation steps for sample processing in advance of gas chromatography/mass spectroscopy (GC/MS) analysis.

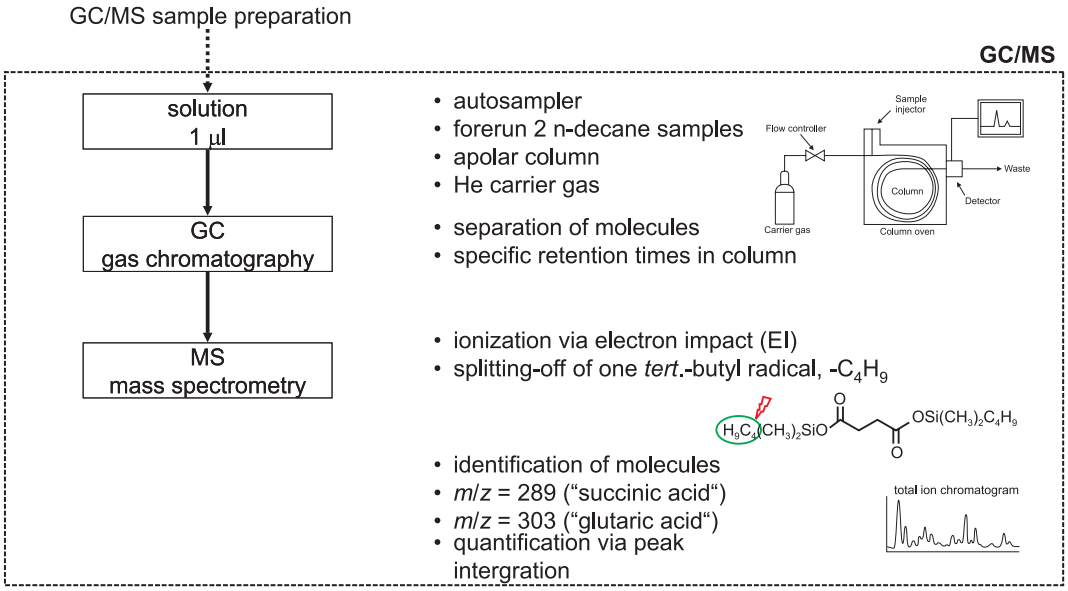

Fig. 4: Analysis of concentrations of succinic acid molecules dissolved from different surfaces types to quantify the binding sites density.

After 2 min vortexing, 250 µl of the supernatant ethyl acetate phase is transferred into a new reaction vial which is then shock-frozen in liquid nitrogen. Next, the sample is stored in an exsiccator for 1.5 hours at pressures below 20 mbar to evaporate the volatile ethyl acetate. The dried sample is re-suspended with 50 µl n-decane and derivatized with 20 µl of N-methyl-tert.-butyldimethylsilyltrifluoroacetamide (MBDSTFA). After a slight vortex, the sample is allowed to react overnight at atmospheric pressure in an exsiccator containing silica gel with moisture indicator. This ensures the sufficient silanization of both carboxylic groups of succinic and glutaric acid.

Calibration samples containing 2 nmolar to 2 µmolar of succinic acid are worked up in the same way as the samples obtained from the different coating types under investigation. 70 µl of each prepared sample are transferred into autosampler vials and capped tightly. The Shimadzu auto injector AOC-20i is used to inject 1 µl of each sample into the Shimadzu gas chromatograph GC-17A. The helium carrier gasflow and the temperature ramp in the oven are adjusted to ensure a clear separation of all sample compounds in the predominantly apolar column (OPTIMA-5-MS-0.25 µm by Macherey-Nagel). The silanisized succinic and glutaric acids enter the Shimadzu MS-QP5000 mass spectrometer with different retention times allowing for a sensitive quantitative analysis of the compounds after fragmentation and ionization by impact of 70 eV electrons. Due to this electron impact, each silanized carboxylic acid molecule loses one tertiary butyl group and can be detected at the mass/charge-ratios (m/z) 289 (succinic acid) and 303 (glutaric acid).

The dilution series with known concentrations of succinic acid is used for calibration of the GC/MS. The ratio of the signal heights of succinic and glutaric acid is used to determine the concentration of succinic acid in the samples. The density of succinic acid molecules on the differently prepared surfaces is then computed taking into account the background, determined with the uncoated teflon reference samples.

The results of the currently achieved spacer density on three selected surface types is shown in Fig. 5. The a-C:H coating deposited from acetylene gas (30 sccm) allows attachment of 0.5 succinic acid molecules per nm^2. The amount of molecules bonded to the coatings deposited with the

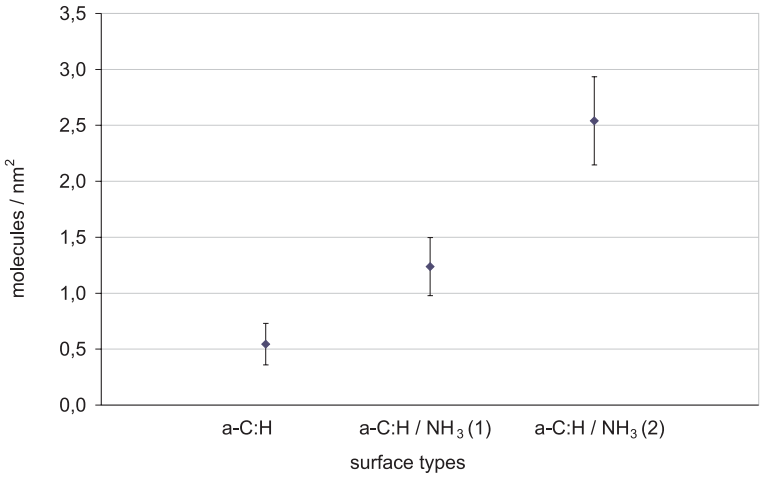

Fig. 5: Covalent bonding of dicarboxylic acid on a-C:H surfaces prepared with different precursors.

additional ammonia precursor is 2.5 times higher with an ammonia/acetylene precursor ratio of 1.0 (a-C:H/$NH_3(1)$) and 5 times higher for a precursor flow ratio of 1.5 (a-C:H/$NH_3(2)$), respectively.

These binding site densities are within the same order of magnitude as observed for ammonia plasma treated polymers. The density can be further increased by systematic adjustment of the plasma parameters. The relationship between deposition conditions and binding site densities is currently established in ongoing investigations with optical emission spectroscopy. Additional surface spectroscopy (FTIR) will reveal which functional groups are grafted to the a-C:H surface.

During the last years we could establish the significant effects of amorphous carbon coatings on the reduction of crystalline bacterial biofilm formation on urological implants [8,9]. The improvement of these properties by additional loading of the coatings with active agents, e.g., with bactericides (e.g. ethacridine lactate), can be reasonably expected and will be investigated in further studies.

Support by the *Stiftung Rheinland-Pfalz für Innovation* is gratefully acknowledged.

References

[1] A. Grill, Diamond and Related Materials **12**, 166-170 (2003).
[2] R. Hauert, Diamond and Related Materials **12**, 583-589 (2003).
[3] S.E. Rodil C. Ramírez, R. Olivares, H. Arzate, J. Réyes-Gasga, C. Magañac, Diamond and Related Materials **15**, 1300-1309 (2006).
[4] L. Kleinen, B. Hillebrands, H. Busch, U. Grabowy, V. Herzog, G. Kirfel, H. Wegner, F. Peukert, N. Laube, 4. Tagung des DVM-Arbeitskreises "Biowerkstoffe", DVM-Berichtband **315**, 157-164 (2004).
[5] J. Robertson, Mat Sci Eng R **37**, 129-281 (2002).
[6] A. Schroeder, G. Francz, A. Brunenk, R. Hauert, J. Mayer, E. Wintermantel, Biomaterials **21**, 449456 (2000).
[7] S.C.H. Kwok, J. Wang. P.K. Chu, Diamond and Related Materials **14**, 7885 (2005).
[8] N. Laube, J. Bradenahl, A. Meißner, L. Kleinen, Journal of Urology, accepted.
[9] L. Kleinen, U. Böde, K. Schenk, H. Busch, J. Bradenahl, S.C. Müller, B. Hillebrands, N. Laube, Plasma Processes and Polymers, submitted.

Chapter 7: Publications

Most publications can be downloaded from http://www.physik.uni-kl.de/hillebrands.

7.1 published

1. *Structural and chemical phase transitions in tungsten carbide films evidenced by the analysis of their stiffness tensors*
   T. Wittkowski, K. Jung, B. Hillebrands, D. Comins
   J. Appl. Phys. **100**, 073513 (2006).

2. *Bose-Einstein condensation of quasi-equilibrium magnons at room temperature under pumping*
   S.O. Demokritov, V.E. Demidov, O. Dzyapko, G.A. Melkov, A.A. Serga, B. Hillebrands, A.N. Slavin
   Nature **443**, 430 (2006).

3. *Domain structure during magnetization reversal of PtMn/CoFe exchange bias micropatterned lines*
   M.O. Liedke, K. Potzger, A.H. Bothmer, J. Fassbender, B. Hillebrands, M. Rickart, P.P. Freitas
   J. Appl. Phys. **100**, 043918 (2006).

4. *Phase-sensitive Brillouin light scattering spectroscopy from spin-wave packets*
   A.A. Serga, T. Schneider, B. Hillebrands, S.O. Demokritov, M.P. Kostylev
   Appl. Phys. Lett. **89**, 063506 (2006).

5. *Orthogonal exchange bias field directions in exchange bias microstructures*
   P. Candeloro, H. Schultheiss, H.T. Nembach, B. Hillebrands, S. Trellenkamp, C. Dautermann, S. Wolff
   Appl. Phys. Lett. **88**, 192510 (2006).

6. *Real time evidence of two-magnon scattering in exchange coupled bilayers*
   M.C. Weber, H. Nembach, B. Hillebrands, M.J. Carey, J. Fassbender
   J. Appl. Phys. **99**, 08J308 (2006).

7. *A new crossed coplanar waveguide design for ultrafast magnetization switching utilizing polymer insulation layers*
   P. Martín Pimentel, S. Trellenkamp, S. Wolff, S.J. Hermsdoerfer, H.T. Nembach, B. Leven, B. Hillebrands
   Appl. Phys. Lett. **88**, 122510 (2006).

8. *Spin-wave eigenmodes of an infinite thin film with periodically modulated exchange bias field*
   C. Bayer, M.P. Kostylev, B. Hillebrands
   Appl. Phys. Lett. **88**, 112504 (2006).

9. *High-spin polarization of Heusler alloys*
   B. Hillebrands, C. Felser
   J. Phys. D: Appl. Phys. **39**, (2006).

10. *Parametric generation of soliton-like spin wave pulses in ferromagnetic thin-film ring resonators*
    A.A. Serga, M.P. Kostylev, B.A. Kalinikos, S.O. Demokritov, B. Hillebrands, H. Benner
    J. Exp. Theo. Phys. **102**, 497 (2006).

11. *Spin-Wave Eigenmodes of Landau-Domain Patterns*
    M. Bolte, G. Meier, C. Bayer
    Phys. Rev. B**73**, 052406 (2006).

12. *Über die Unsicherheit von Messwerten am Beispiel des BONN-Risk-Index*
    N. Laube, L. Kleinen
    Der Urologe **45**, 189 (2006).

13. *Plasmadeponierte Kohlenstoffbeschichtung auf urologischen Verweilkathetern*
    N. Laube, J. Bradenahl, A. Meißner, J. v. Rappard, L. Kleinen, S.C. Müller
    Der Urologe **45**, 1163 (2006).

14. *Spin-lattice relaxation phenomena in manganite LSMO thin films*
    M.C. Weber, B. Hillebrands, V. Moshnyaga, K. Samwer
    Europhys. Lett. **73**, 285 (2006).

15. *Magnetic patterning of Fe/Cr/Fe(001) trilayers by Ga+ ion irradiation*
    S. Blomeier, B. Hillebrands, V.E. Demidov, S.O. Demokritov, B. Reuscher,
    A. Brodyanski, M. Kopnarski
    J. Appl. Phys. **98**, 093503 (2005).

16. *Domain Structure of Magnetically Micro-Patterned PtMn/NiFe Exchange Bias Bilayers*
    K. Potzger, L. Bischoff, M.O. Liedke, B. Hillebrands, M. Rickart, P.P. Freitas, J. McCord, J. Fassbender
    IEEE Trans. Magn., **41**, 3094 (2005).

7.2 in press

1. *Micromagnetism and magnetization reversal of embedded ferromagnetic elements*
    S. Blomeier, P. Candeloro, B. Hillebrands, B. Reuscher, A. Brodyanski, M. Kopnarski
    Phys. Rev. B, in press.

2. *Magnetic anisotropies and magnetization reversal of the $Co_2Cr_{0.6}Fe_{0.4}Al$ Heusler compound*
    J. Hamrle, S. Blomeier, O. Gaier, B. Hillebrands, R. Schäfer, M. Jourdan
    J. Appl. Phys., in press.

3. *Ion beam-induced magnetic nanopatterning of interlayer exchange coupled Fe/Cr/Fe trilayers*
    S. Blomeier, P. Candeloro, B. Hillebrands, B. Reuscher, A. Brodyanski, M. Kopnarski
    J. Magn. Magn. Mater., in press.

4. *Diamond-like carbon coatings on ureteral stents - A new strategy in reducing formation of crystalline bacterial biofilms?* N. Laube, J. Bradenahl, A. Meißner, L. Kleinen, Journal of Urology, in press.

7.3 submitted

1. *Linear and nonlinear phase accumulation of backward volume magnetostatic spin waves in yttrium-iron-garnet spinwave waveguides*
   T. Schneider, A.A. Serga, B. Hillebrands, M.P. Kostylev
   submitted to Europhys. Lett..

2. *Shaping of microwave pulses using phase-sensitive spin-wave amplifier*
   A.A. Serga, T. Schneider, B. Hillebrands, M.P. Kostylev, A.N. Slavin
   submitted to Appl. Phys. Lett..

3. *Huge quadratic magneto-optical Kerr effect in the Co_2FeSi Heusler compound* J. Hamrle, S. Blomeier, O. Gaier, B. Hillebrands, H. Schneider, G. Jakob, K. Postava, C. Felser
   submitted to J. Phys. D: Appl. Phys..

4. *Ion beam induced modification of exchange interaction and spin-orbit coupling in the Co_2FeSi Heusler compound*
   J. Hamrle, S. Blomeier, O. Gaier, B. Hillebrands, H. Schneider, G. Jakob, B. Reuscher, A. Brodyanski, M. Kopnarski, K. Postava, C. Felser
   submitted to J. Phys. D: Appl. Phys..

5. *Microwave assisted switching in a $Ni_{81}Fe_{19}$ ellipsoid*
   H.T. Nembach, P. Martín Pimentel, S.J. Hermsdoerfer, B. Leven, S.O. Demokritov, B. Hillebrands
   submitted to Appl. Phys. Lett..

6. *Direct observation of magnetic exchange coupling effects in arrays of embedded ferromagnetic elements*
   S. Blomeier, B. Hillebrands, B. Reuscher, A. Brodyanski, M. Kopnarski
   submitted to Phys. Rev. Lett..

7. *Resonant and non-resonant scattering of dipole-dominated spin waves from a region of inhomogeneous magnetic field in a ferromagnetic film*
   M.P. Kostylev, A.A. Serga, T. Schneider, B. Leven, B. Hillebrands, R.L. Stamps
   submitted to Phys. Rev. B.

8. *Evidence of lateral coupling in exchange bias double layers with lateral modulation of the exchange bias field*
   P. Candeloro, S. Blomeier, P.A. Beck, H. Schultheiß, H.T. Nembach, B. Hillebrands, M.O. Liedke, J. Fassbender, B. Reuscher
   submitted to J. Appl. Phys..

9. *Amorphous carbon coatings inhibit crystalline biofilm formation on urological implants*
   L. Kleinen, U. Böde, K. Schenk, H. Busch, J. Bradenahl, S.C. Müller, B. Hillebrands, N. Laube
   submitted to Plasma Processes and Polymers.

7.4 Ph.D. theses

1. *Schaltverhalten magnetischer Strukturen auf der Subnanosekunden-Zeitskala*
   Hans Nembach, Ph.D. thesis, Technische Universität Kaiserslautern, April 2006.

2. *Das Spinwellen-Eigenspektrum in homogen und inhomogen magnetisierten Strukturen und periodischen Übergittern*
   Christian Bayer, Ph.D. thesis, Technische Universität Kaiserslautern, March 2006.

3. *Optische Kontrolle der Magnetisierung in austauschgekoppelten magnetischen Bilagen*
   Markus Weber, Ph.D. thesis, Technische Universität Kaiserslautern, December 2005.

Chapter 8: Conferences, Workshops, Schools, Seminars

(shown in chronological order with the speaker named)

8.1 Conferences

8.1.1 Invited talks

B. Hillebrands:
Spinwaves: propagation, manipulation, detection
JEMS, San Sebastian, Spain, June 2006

B. Hillebrands:
Brillouin light scattering from small magnetic elements
ICMFS'06, Sendai, Japan, August 2006

8.1.2 Contributed talks and posters

S. Blomeier:
Magnetic patterning of interlayer exchange coupled Fe/Cr/Fe trilayers induced by ion irradiation
MMM Conference 2005, San Jose, USA, November 2005

M. Weber:
Real time evidence of two-magnon scattering in exchange coupled bilayers
MMM Conference 2005, San Jose, USA, November 2005

A. Serga:
Stimulated phase-coherent recovery of microwave signal stored in spin wave excitations
MMM Conference 2005, San Jose, USA, November 2005

B. Leven:
Magnetic logic with spin waves
MMM Conference 2005, San Jose, USA, November 2005

M.O. Liedke:
Domain structure during magnetization reversal of PtMn/CoFe exchange bias micro-patterned lines
MMM Conference 2005, San Jose, USA, November 2005

J. Hamrle:
Magnetic properties of $Co_2Cr_{0.6}Fe_{0.4}Al$ and Co_2FeSi Heusler alloys
4th International Symposium on New Materials with high spin polarization, Dresden, April 2006

M.O. Liedke:
Exchange bias on rippled substrates - step induced uniaxial versus unidirectional anisotropy
INTERMAG Conference, San Diego, USA, May 2006

B. Hillebrands:
Phase-sensitive Brillouin light scattering spectroscopy
INTERMAG Conference, San Diego, USA, May 2006

P. Martín Pimentel:
Microwave assisted switching in $Ni_{81}Fe_{19}$ elements
INTERMAG Conference, San Diego, USA, May 2006

T. Schneider:
Space and time resolved phase measurements of dipolar dominated spin waves in Yttrium iron garnet waveguides
JEMS, San Sebastian, Spain, June 2006

P. Martín Pimentel:
Microwave assisted switching in $Ni_{81}Fe_{19}$ elements
JEMS, San Sebastian, Spain, June 2006

H. Schultheiß:
Brillouin light scattering microscopy investigations of quantized spin waves in small magnetic ring structures
JEMS, San Sebastian, Spain, June 2006

P. Martín Pimentel:
A new crossed coplanar waveguide design for ultrafast magnetization switching utilizing polymer insulation layers
JEMS, San Sebastian, Spain, June 2006

P. Candeloro:
Orthogonal exchange bias directions in FeMn/NiFe microstructures
JEMS, San Sebastian, Spain, June 2006

S. Blomeier:
Ion beam induced magnetic patterning on interlayer exchange coupled Fe/Cr/Fe-trilayers
International Conference on Magnetism (ICM), Kyoto, Japan, August 2006

A. Serga:
Observation of spin wave envelope soliton interaction by means of phase-sensitive Brillouin light scattering spectroscopy
International Conference on Magnetism (ICM), Kyoto, Japan, August 2006

P. Martín Pimentel,:
Microwave assisted switching in $Ni_{81}Fe_{19}$ elements
AOFA, Kaiserslautern, September 2006

L. Kleinen:
Beeinflussung von Kristallisationsvorgängen an Oberflächen durch plasmadeponierte amorphe Kohlenstoffschichten
AOFA, Kaiserslautern, September 2006

H. Schultheiß:
Brillouin light scattering microscopy investigations of quantized spin waves in small magnetic ring structures
AOFA, Kaiserslautern, September 2006

S. Blomeier:
Ion beam induced fabrication of ferromagnetic microelements
AOFA, Kaiserslautern, September 2006

S. Blomeier:
Ion beam induced fabrication of ferromagnetic microelements
15th International Conference on Ion Beam Modification of Materials, Taormina, Italy, September 2006

8.1.3 Contributions to the DPG Frühjahrstagung

13 contributions: DPG Frühjahrstagung, Dresden, March 2006

8.2 Workshops

8.2.1 Invited talks

B. Hillebrands:
Spin based transport in novel materials
Workshop on Magnetic Soft Matter, Max Planck Institute for Polymer Research, Mainz, September 2006

B. Hillebrands:
Stand und Zukunft magnetischer Technologien
Workshop “Magnetische Mikrosysteme”, Ministerium für Wirtschaft, Verkehr, Landwirtschaft und Weinbau RLP, Mainz, September 2006

B. Hillebrands:
Spin waves in magnetic structures
378th WE-Heraeus Seminar, Spin Torque in Magnetic Nanostructures Physikzentrum, Bad Honnef, October 2006

B. Hillebrands:
Dynamics in small magnetic elements for magnetoelectronic applications
Japan-Germany joint Workshop on Nanoelectronics, Tokyo, October-November 2006

8.2.2 Contributed talks and posters

J. Harmle:
Brillouin light scattering microscopy investigations of quantized spin waves in mesoscopic magnetic rings
364th WE-Heraeus seminar “Nanoscale Magnets - Top-down meets Bottom-up”, Bad Honnef, January 2006

J. Hamrle:
Magnetic properties of $Co_2Cr_{0.6}Fe_{0.4}Al$ and Co_2FeSi Heusler alloys
International Workshop on Spin Transfer (IWST)’06, Nancy, France, October 2006

J. Hamrle:
Magnetic and magneto-optical properties of Co_2FeSi *and* $Co_2Cr_{0.6}Fe_{0.4}Al$ *Heusler compounds*
378th WE-Heraeus Seminar, Spin Torque in Magnetic Nanostructures, Bad Honnef, October 2006

H. Schultheiß:
Observation of partial decoherence of quantized spin waves in nanoscaled magnetic ring structures
378th WE-Heraeus Seminar, Spin Torque in Magnetic Nanostructures, Bad Honnef, October 2006

8.3 Meetings

P. Martín Pimentel:
Magneto-optical studies of the magnetization under microwave excitation
Final Meeting ULTRASWITCH, TU Kaiserslautern, May 2006

J. Hamrle:
Magnetic anisotropy in Co_2FeSi Heusler compound
Final Meeting ULTRASWITCH, TU Kaiserslautern, May 2006

B. Hillebrands:
Magnetodynamic investigations of Heusler compounds
NEDO meeting, Matsushima, Japan, August 2006

P. Candeloro:
Control of multiple exchange Bias directions
Nexbias meeting, University of York, United Kingdom, June 2006

8.4 Summer Schools

B. Hillebrands:
Magneto-Optics
ULTRASMOOTH Summerschool, Durham, UK, July 2006

B. Hillebrands:
Spindynamics I: Dynamics in small magnetic strukures
Spindynamics II: Linear and nonlinear optics with spin waves
WE-Heraeus Summerschool “Nanomagnetism”, Schloss Rauischholzhausen, Gießen, September 2006

B. Hillebrands:
Spindynamics I: Dynamics in small magnetic strukures
Spindynamics II: Linear and nonlinear optics with spin waves
International school & workshop “Modern Problems of Spin Dynamics”, Strasbourg, France, October 2006

8.5 Invited colloquia and seminars

P. Martín Pimentel:
Microwave assisted switching and direct writing for magnetic random access memory devices (MRAM)
Sensitec-Naomi, Mainz, March 2006

P. Candeloro:
Magnetization reversal process in patterned NiFe/NiMn exchange-bias bilayers
Scuola Normale Superiore (SNS), Pisa, Italy, May 2006

P. Candeloro:
Magnetic investigation of exchange-bias bilayers patterned by electron beam lithography and ion irradiation techniques
Laboratory for Micro- and Nanotechnology (LMN), Paul Scherrer Institut (PSI), Villigen, Switzerland, May 2006

P. Martín Pimentel:
Magneto-optical studies of the magnetization in $Ni_{81}Fe_{19}$ elements
Instituto de ciencia de la materia, Madrid, Spain, September 2006

8.6 IEEE-Magnetics Society Distinguished Lectures

In 2005 B. Hillebrands served for the IEEE-Magnetics Society as a Distinguished Lecturer to promote the science of magnetism as well as the goals of the Society. Annually the Society selects three Distinguished Lecturers.

The lecture was entitled: *Dynamics in magnetic micro- and nanostructures*.

The Lecture was given on invitation from local Chapters of the Magnetics Society and on invitation from universities and research laboratories.

In the report period the following lectures were presented:

05.12.2005	UTH Stockholm, Stockholm, Sweden
06.12.2005	Iniversity of Upsalla, Upsalla, Sweden

16.01.2006	TU Wien, Vienna, Austria
05.05.2006	Oakland University, Michigan, USA
12.05.2006	University of California San Diego, Center for Magnetic Recording Research, USA

8.7 Contributions to other meetings

J. Hamrle:
Coherence and dissipation of spin-wave eigen modes in magnetic micro- and nano-structures
Assessment-Colloquium of Schwerpunkt SPP 1133, Bad Honnef, March 2006

B. Leven:
Interaction of spin waves with domain walls
Assessment-Colloquium of Schwerpunkt SPP 1133, Bad Honnef, March 2006

L. Kleinen:
Versatile amorphous carbon coatings on polymers and on tools for polymer processing
Trade fair: ACHEMA Industrial Biotechnology Partnering Conference, Frankfurt, May 2006

A. Serga:
Parametrical interaction of spin waves and oscillations with non-stationary local pumping
Taras Shevchenko National University of Kiev, Faculty of Radiophysics, Kiev, Ukraine, July 2006

A. Serga:
Parametrical interaction of spin waves and oscillations with non-stationary local pumping
National Technical University of Ukraine “Kyiv Polytechnic Institute”, Faculty of Radioengineering, Kiev, Ukraine, September 2006

A. Serga:
Parametrical interaction of spin waves and oscillations with non-stationary local pumping
Institute of Physics (National Academy of Science of Ukraine), Kiev, Ukraine, September 2006

Appendix: Impressions from 2006

Football World Championship Celebration:

Honorary Doctor Award on Oct 30, 2006: Prof. Albert Fert